An Experimental Investigation of Flow Over an Oscillating Airfoil

Panayiote Gerontakos

Department of Mechanical Engineering
McGill University, Montreal, Quebec, Canada
February 2004

A thesis submitted to McGill University in partial fulfillment of the requirements of the degree of Master of Engineering

© Panayiote Gerontakos 2004

Library and Archives Canada

Published Heritage Branch

395 Wellington Street
Ottawa ON K1A 0N4
Canada

Bibliothèque et Archives Canada

Direction du Patrimoine de l'édition

395, rue Wellington
Ottawa ON K1A 0N4
Canada

Your file Votre référence
ISBN: 0-612-98528-8
Our file Notre référence
ISBN: 0-612-98528-8

NOTICE:
The author has granted a non-exclusive license allowing Library and Archives Canada to reproduce, publish, archive, preserve, conserve, communicate to the public by telecommunication or on the Internet, loan, distribute and sell theses worldwide, for commercial or non-commercial purposes, in microform, paper, electronic and/or any other formats.

The author retains copyright ownership and moral rights in this thesis. Neither the thesis nor substantial extracts from it may be printed or otherwise reproduced without the author's permission.

AVIS:
L'auteur a accordé une licence non exclusive permettant à la Bibliothèque et Archives Canada de reproduire, publier, archiver, sauvegarder, conserver, transmettre au public par télécommunication ou par l'Internet, prêter, distribuer et vendre des thèses partout dans le monde, à des fins commerciales ou autres, sur support microforme, papier, électronique et/ou autres formats.

L'auteur conserve la propriété du droit d'auteur et des droits moraux qui protège cette thèse. Ni la thèse ni des extraits substantiels de celle-ci ne doivent être imprimés ou autrement reproduits sans son autorisation.

In compliance with the Canadian Privacy Act some supporting forms may have been removed from this thesis.

While these forms may be included in the document page count, their removal does not represent any loss of content from the thesis.

Conformément à la loi canadienne sur la protection de la vie privée, quelques formulaires secondaires ont été enlevés de cette thèse.

Bien que ces formulaires aient inclus dans la pagination, il n'y aura aucun contenu manquant.

Canada

ACKNOWLEDGEMENTS

The author would like to express his appreciation to Professor Tim Lee for his support and guidance throughout this project. His help and advice was invaluable. Credit must also be given to the research group of the Experimental Aerodynamics Laboratory of the Department of Mechanical Engineering of McGill University and the support staff. These include David Birch, Anthony Panagakos, George Petrakis, Georges Tewfik, Mario Iacobaccio and Mario Sglavo. More personally, the author would like to thank Carmelina Giurleo, his parents, Vassilios and Despina Gerontakos, and the rest of his family for their encouragement.

ABSTRACT

The detailed behaviour of the unsteady boundary layer and stall events occurred on a sinusoidally oscillating NACA 0012 airfoil at Re = 1.35×10^5 was investigated experimentally by using closely-spaced multiple hot-film sensor arrays. The hot-film measurements were supplemented by surface pressure measurements, hot-wire wake velocity surveys and smoke-flow visualizations. Three typical oscillation parameters: attached flow, light stall, and deep stall were tested. Special attention was focused on the non-intrusive identification of the spatial-temporal progression of the locations of the boundary-layer transition and separation and reattachment points for a range of oscillation frequencies and amplitudes both prior to, during, and post the stall. The results show that for an unsteady airfoil, the reduced frequency of the oscillation was found to be highly significant and only small values of reduced frequency were required to delay the onset of the various boundary-layer events, and to produce significant variations and hysteresis in the peak values of lift and drag forces and the pitching moments, which are fundamentally different from their static counterparts. Lift stall was observed to occur when the leading-edge vortex reached 90% of the chord, while moment stall occurred at the end of the upward spread of the trailing-edge flow reversal. The convection speed of the leading-edge and the secondary vortices were also reported. Dynamic stall was found to be caused by an abrupt turbulent separation near the leading-edge region and not with the bursting of the laminar separation bubble, as is commonly observed for a static NACA 0012 airfoil; the result being the initiation, growth and convection of an energetic leading-edge vortex. Moreover, the detection of the sudden turbulent breakdown could serve as an indicator for dynamic stall detection and control. The results reported on here provide a deepened insight into the detailed nature of the unsteady boundary-layer events as well as the stalling mechanisms at work at different stages in the dynamic-stall process.

RÉSUMÉ

Le comportement détaillé des évènements de la couche limite irrégulier et du décrochage qui est arrivé sur une surface portant NACA 0012 oscillante à Re = 1.35×10^5 à été investigué expérimentalement par plusieurs détecteurs <<hot-film>>. Ces mesures ont été supplémentées par des mesures de la pression sur la surface, des inspections de la vélocité dans le sillage et des visualisations de la circulation. Trois paramètres typiques de l'oscillation : circulation attachée, décrochage léger, et décrochage profond ont été testé. Une attention spéciale a été mise sur l'identification non-intrusif de la progression spatial-temporal des locations des pointes de transition, séparation et attachement de la couche limite pour une gamme de fréquences et amplitudes oscillatoires dans les circonstances; avant, durant et après le décrochage. Les résultats montrent que, pour une surface portant oscillée, la fréquence non-dimensionné de l'oscillation a été très important et seulement des petites valeurs de la fréquence non-dimensionné a été requise pour retarder le commencement des plusieurs évènements de la couche limite, et à produire des variations signifiantes et de l'hystérésis dans les valeurs maximales des forces aérodynamiques, qui sont fondamentalement différent de ses homologues stables. Le décrochage du force soulevant a pris place quand le tourbillon du bord d'attaque s'est rendu à 90% de la corde, alors que le décrochage du moment a pris place à la fin du mouvement vers le haut de la circulation renversé du bord de fuite. La vitesse conventionnaire du tourbillon du bord d'attaque, ainsi que les tourbillons secondaires, ont été reporté. C'était trouvé que le décrochage dynamique a été causé par une séparation turbulente soudain dans une région près du bord d'attaque et non avec l'éclatement de la bulle de séparation, comme est généralement observé pour une surface portant stable NACA 0012; le résultat étant l'initiation, croissance et convection d'une tourbillon du bord d'attaque énergique. De plus, la détection de la dégradation turbulente soudain peut servir comme une indicatrice pour la détection et contrôle du décrochage dynamique. Les résultats reportés ici fournissent une compréhension plus profond de la nature détaille des évènements de la couche limite irrégulier, ainsi que le mécanisme de décrochage qui se trouve dans les différentes phases du procès de décrochage dynamique.

TABLE OF CONTENTS

NOMENCLATURE

c	chord length
C_d	section pressure drag coefficient, $= \dfrac{d}{0.5\rho U_\infty^2 c}$
C_l	section lift coefficient, $= \dfrac{l}{0.5\rho U_\infty^2 c}$
$\Delta C_{l\max}$	maximum lift coefficient increment, $= \Delta C_{l\text{at}} + \Delta C_{l\text{fr}} + \Delta C_{l\text{LEV}}$
$C_{l\alpha}$	lift-curve slope, $= dC_l/d\alpha$
$\Delta C_{l\text{at}}$	lift increment due to attached-flow effect
$\Delta C_{l\text{fr}}$	lift increment due to flow reversal
$\Delta C_{l\text{LEV}}$	lift increment due to transient LEV effect
C_m	sectional pitching moment coefficient, $= \dfrac{m_P}{0.5\rho U_\infty^2 c^2}$
$\Delta C_{m,min}$	pitching moment coefficient increment
C_p	pressure coefficient, $= \dfrac{p - p_\infty}{0.5\rho U_\infty^2}$
d	section drag
f_o	oscillation frequency
l	section lift
l_b	laminar separation bubble length
L	lift stall
LESP	leading-edge stagnation point
LEV	leading-edge vortex
M	moment stall
MHFS	multi-element hot-film sensor
m_p	sectional pitching moment
p	static pressure
Re	Reynolds number, $= cU_\infty/\nu$
rms	root-mean-square
s	sensor spacing

t	time
U_{LEV}	leading-edge vortex convection speed
U_{2ND}	secondary vortex convection speed
U_∞	free-stream velocity
x	streamwise distance along the airfoil
y	transverse distance above the airfoil chordline
α	angle of attack
α_m	mean angle of attack
α_{min}	minimum angle of attack
α_{max}	maximum angle of attack
$\alpha(t)$	instantaneous angle of attack, $= \alpha_m + \Delta\alpha \sin\omega t$
$\Delta\alpha$	oscillation amplitude
α_{ds}	dynamic-stall angle
α_{ss}	static-stall angle
$\Delta\alpha_{tl}$	stall-angle increment due to attached-flow effect
$\Delta\alpha_{fr}$	stall-angle increment due to flow reversal
$\Delta\alpha_{LEV}$	stall-angle increment due to transient LEV effect
ω	angular frequency, $= 2\pi f_o$
κ	reduced frequency, $= \omega c/2u_\infty = \pi f_o c/U_\infty$
τ	phase angle, $= \omega t$
ν	fluid viscosity
ρ	fluid density

Subscripts

d	downstroke
u	upstroke

LIST OF FIGURES

Figure 9 Boundary-layer events of a static NACA 0012 airfoil at $Re = 1.35 \times 10^5$. (a) critical flow points, (b) C_l–α curve, (c) bubble length l_b, and (d) C_p distributions.

Figure 10 Identification of (a) laminar separation and (b) boundary-layer transition over a static NACA 0012 from MHFS signals.

Figure 11 Smoke flow visualization pictures for a static NACA 0012 airfoil at angles of attack (a) 2 deg, (b) 4 deg, (c) 5 deg, (d) 6 deg, (e) 7 deg, (f) 8 deg, (g) 9 deg, (h) 10 deg, (i) 12 deg, (j) 15 deg and (k) 20 deg. The flow is from left to right.

Figure 12 Typical 3-D representation of the wake mean and fluctuating velocity profiles. (a) static airfoil, (b) $\alpha(t) = 0^o + 7.5^o \sin\omega t$ and $\kappa = 0.05$, (c) $\alpha(t) = 0^o + 15^o \sin\omega t$ and $\kappa = 0.05$, and (d) $\alpha(t) = 10^o + 15^o \sin\omega t$ and $\kappa = 0.10$. (e) 2-D presentation of (d) at selected $\alpha(t)$ corresponding to Regions A–F with o, $\kappa = 0.05$; □, $\kappa = 0.10$; Δ, $\kappa = 0.20$ and; ___, static airfoil.

Figure 13 Representative MHFS signals for $\alpha(t) = 0^o + 7.5^o \sin\omega t$ at $\kappa = 0.05$. (a) S_1-S_{116} and (b) S_{114}-S_{126}. T_1 through T_{17} denote the locus of the leading-edge stagnation point (LESP). For sensor S_{76}, point 1 identifies transition, the region between points 2 and 3 indicates an attached turbulent boundary layer and point 4 denotes the return to a laminar boundary layer.

Figure 14 Loci of boundary layer (a) transition and (b) relaminarization for $\alpha(t) = 0^o + 7.5^o \sin\omega t$: ○, $\kappa = 0.025$; □, $\kappa = 0.05$; Δ, $\kappa = 0.1$; and ♦, static airfoil.

Figure 15 Dynamic load loops for $\alpha(t) = 0^o + 7.5^o \sin\omega t$ (a) $\kappa = 0.025$, (b) $\kappa = 0.05$ and (c) $\kappa = 0.1$; _____, increasing α; ----, decreasing α; and ....., static values.

Figure 16 Selected smoke flow visualization pictures for an oscillating airfoil at $\alpha(t) = 0^o + 15^o \sin\omega t$ and $\kappa = 0.05$. (a) $\alpha_u = -14.44$ deg, (b) $\alpha_u = 0$ deg, (c) $\alpha_u = 9.8$ deg, (d) $\alpha_u = 13.6$ deg, (e) $\alpha_u = 13.7$ deg, (f) $\alpha_u = 14.38$ deg, (g) $\alpha_d = 14.64$ deg, (h) $\alpha_d = 14.2$ deg, (i) $\alpha_d = 9.78$ deg, (j) $\alpha_d = 3.33$ deg, (k) $\alpha_d = -2.31$ deg, (l) $\alpha_d = -8.31$ deg and (m) a conceptual sketch of (f). Flow is from left to right. Subscripts u and d denote upstroke and downstroke, respectively.

Figure 17 Composite plot of representative MHFS signals for $\alpha(t) = 0^o + 15^o \sin\omega t$ at $\kappa = 0.05$. Point 1 identifies transition, 1-2 attached turbulent boundary layer, 3-4 separated turbulent boundary layer, 4 onset of turbulent boundary layer reattachment, 5 end of relaminarization, 6 laminar separation and 7 laminar reattachment. Δ, flow reversal and $\blacktriangledown$, turbulent separation.

Figure 18 Boundary layer events for $\alpha(t) = 0^o + 15^o \sin\omega t$ at $\kappa = 0.05$: (a) flow reversal (open symbols) and turbulent separation (solid symbols), (b) transition, and (c) reattachment and relaminarization.

Figure 19 Dynamic load loops for $\alpha(t) = 0^o + 15^o \sin\omega t$ (a) $\kappa = 0.025$, (b) $\kappa = 0.05$ and (c) $\kappa = 0.1$; _____, increasing α; ----, decreasing α; and ....., static values.

Figure 20 Representative MHFS signals for $\alpha(t) = 10^o + 15^o \sin\omega t$ at $\kappa = 0.1$. (a) $S_{124}-S_{72}$ and (b) $S_{63}-S_2$. Δ, flow reversal; $\downarrow$, turbulent separation; $\blacktriangledown$, passage of LEV; and ∇, passage of secondary vortex. Point 1 denotes transition, points 2–3 turbulent breakdown and 3–4 separated flow.

Figure 21 Selected sequences of boundary-layer events both prior to, during, and post stall at $\kappa = 0.1$ for $\alpha(t) = 10^o + 15^o \sin\omega t$. (a) upward spread of flow reversal for 12.9 deg $< \alpha_u <$ 21.6 deg; (b) turbulent breakdown and the formation of a LEV at $\alpha_u = 21.9$ deg; (c) LEV growth and rearward convection for $\alpha_u = 22.4$ deg – 24.4 deg; (d) LEV catastrophic detachment at $\alpha_u = 24.7$ deg; (e)

separated flow for $\alpha_d > 14.1$ deg; (f) and (g) rearward reattachment for $\alpha_d < 14.1$ deg; (h)–(n) are the conceptual sketches of (a)–(g), respectively.

Figure 22 Loci of boundary-layer (a) transition, (b) flow reversal (o) and turbulent breakdown (•), (c) LEV, (d) secondary vortex, (e) reattachment, and (f) relaminarization at $\kappa = 0.1$ for $\alpha(t) = 10^\circ + 15^\circ \sin\omega t$. Note that only the clearly identifiable critical flow points were plotted. ♦, static airfoil.

Figure 23 Variation of dynamic loads with reduced frequency for $\alpha(t) = 10^\circ + 15^\circ \sin\omega t$. (a) $\kappa = 0.1$, (b) $\kappa = 0.05$, and (c) $\kappa = 0.025$. 1, onset of flow reversal; 2, end of upward spread of flow reversal; 3, turbulent breakdown; 4, lift stall; 4–5, full stall; 6, onset of secondary vortex; 7, onset of flow reattachment; and 8, end of flow reattachment. ____, increasing α; ----, decreasing α; ....., static values; M, moment stall; and L, lift stall.

Figure 24 Effect of reduced frequency on boundary layer and stall events for $\alpha_m = 10^\circ$ and $\Delta\alpha = 15^\circ$: (a) flow reversal and separation; (b) LEV; (c) secondary vortex; (d) transition; and (e) reattachment. o, $\kappa = 0.05$; □, $\kappa = 0.1$; and Δ, $\kappa = 0.2$. Solid symbols denote flow reversal and open symbols turbulent breakdown. Note that for (e) and (f) the case of $\kappa = 0.2$ is omitted for clarity. ♦, static airfoil.

Figure 25 Effect of oscillation amplitude on flow reversal (open symbols) and turbulent breakdown (solid symbols) with $\alpha_m = 10^\circ$ and $\kappa = 0.1$. o, $\Delta\alpha = 5^\circ$; □, $\Delta\alpha = 10^\circ$; Δ, $\Delta\alpha = 15^\circ$; and ◊, $\Delta\alpha = 20^\circ$. ♦, static airfoil.

Figure 26 Dynamic load loops at $\kappa = 0.05$. $\alpha_m = 10^\circ$: (a) $\Delta\alpha = 5^\circ$ and (b) $\Delta\alpha = 10^\circ$. $\alpha_m = 15^\circ$: (c) $\Delta\alpha = 10^\circ$ and (d) $\Delta\alpha = 15^\circ$. ___, increasing α; ----, decreasing α; ....., static values; M, moment stall; and L, lift stall.

LIST OF FIGURES IN APPENDIX

LIST OF TABLES

1. INTRODUCTION

1.1 Problem Statement

The study of unsteady flow past airfoils has received much attention due to both its research and technological significance. The flow past static airfoils is relatively straightforward and is fairly well understood. It can be described as consisting of a trailing edge turbulent separation point that progresses upstream with increasing incidence until the point at which it encounters a laminar separation bubble, a region of "dead" flow delimited by a laminar separation point and turbulent reattachment point, as is shown in Figure 1. This causes the bubble to "burst" and leads to lift and moment stall. Note that the presence and size of a laminar separation bubble is dependent on airfoil geometry. The addition of another independent variable, time, complicates this process and is still not fully understood.

The process of dynamic stall has been shown by previous research to be quite complex. Consequently, the understanding of its effect on aircraft stall characteristics demands much effort, particularly on the dynamic retreating blade stall problems of helicopters. It is well known that dynamic stall limits the performance of modern helicopters [3, 4, 9, 20, 22], causes increased torsional loading [11, 20], reduces aerodynamic damping [20] and vibrations [20, 22, 24, 27], and can possibly be used to increase the performance of various machines that encounter unsteady flow [3, 7, 8, 21, 27, 34].

Many researchers who have conducted experimental [2, 3, 11, 12, 13, 18, 21, 23, 25, 28, 29, 32, 36] or numerical [7, 15, 30] studies have described the process of dynamic stall. It begins with flow separation which progresses towards the leading edge of the airfoil. This is followed by the formation of a vortex over the leading-edge region of the airfoil, commonly referred to as the leading-edge vortex (LEV) or dynamic vortex, and its subsequent growth and convection over the airfoil, which is the distinguishing feature of dynamic stall. The presence of this vortex produces a nonlinearly fluctuating pressure field and causes the maximum loads, negative moments and the stall angle to exceed those of a static airfoil. As the vortex passes over the surface of the airfoil and into the wake, both moment and lift stall occur and the boundary layer is in a state of total separation.

Reattachment begins once the angle of attack is sufficiently low, and progresses from the leading edge towards the trailing edge. An excellent review on unsteady airfoils is given by McCroskey [27] and an excellent paper describing dynamic stall experiments was written by McCroskey *et al.* [28]. Also, Leishman's book [20] provides an excellent fundamental background in the area of helicopter aerodynamics with chapters focused on unsteady aerodynamics and dynamic stall.

The structure of the boundary layer over a dynamic airfoil is composed of many flow phenomena and is dependant on many parameters. A complete list of these parameters would include airfoil geometry, Reynolds number, Mach number, type of unsteadiness (plunging, pitching or translation), motion waveform (sinusoidal, constant-ramp rate or arbitrary), reduced frequency, mean angle of attack and oscillation amplitude, although it is the effect of the parameters which describe the unsteady motion which are dominant [2, 3, 24, 28, 29]. Also, depending on the magnitude of the maximum angle of attack, three different unsteady flow cases or phenomena are observed: attached flow, light stall and deep stall. The attached flow case occurs when the airfoil is oscillated and the maximum angle of attack is less then the static-stall angle. This type of flow is characterized by fully attached flow throughout the cycle with little hysteresis in the loads or deviation from static values. The light stall case occurs when the airfoil's maximum angle of attack is just past the static-stall angle. In this case, separation does occur and a leading-edge vortex is formed, but the airfoil never stalls. Also, the loads are increased and hysteresis is present. When the airfoil is oscillated such that its maximum angle of attack is well beyond the static-stall angle, the airfoil penetrates the deep stall regime. A stronger leading-edge vortex forms resulting in a large overshoot in the maximum lift coefficient and stall angle over that of a static airfoil. This is accompanied by large hysteresis in the dynamic load loops. McCroskey [27] provides a sketch of the basic features of the boundary layer over an oscillating airfoil for the light and deep stall cases, and is reproduced in Figure 2.

Of the many experimental studies which have focused on unsteady airfoils, many possess resolution issues with their measurements and/or the values of the parameters chosen, as listed above, are outside the range applicable to the dynamic stall of helicopter rotors, as stated by Johnson and Ham [11]. An example of the former are the experiments of

Carr *et al.* [2] whose measurements consisted of 17 pressure taps spread around the whole airfoil and 6 single hot-wires placed in the boundary layer of the top surface of the airfoil. An example of the later are the experiments of Bass *et al.* [1] which were carried out at reduced frequencies between 0.5 and 10, and maximum angle of attack below 9 degrees. In making these statements, the author's intention is not to discredit their experiments or results, but to point out the possibility for improvement.

1.2 Objectives

The purpose of this work was to investigate and characterize, in greater detail than previously done, the behaviour of the unsteady boundary layer developed over a sinusoidally oscillated NACA 0012 airfoil. This was carried out for various combinations of reduced frequency and oscillation parameters, which include mean angle of attack and oscillation amplitude, corresponding to conditions prior to, during and post static stall. An array of closely-spaced, multiple hot-film sensors provided a non-intrusive way of establishing the spatial and temporal progression of the critical boundary layer flow points. These include the state of the boundary layer (i.e. laminar, laminar-to-turbulent transition, or turbulent), the points of separation and reattachment, the flow reversal point, the presence and length of the laminar separation bubble, and the formation, growth, convection and shedding of the leading-edge vortex. Detailed surface pressure distributions, which when integrated numerically generate the unsteady lift and pressure drag forces and pitching moments, were obtained to characterize the variation of the loads with angle of attack. The combination of these two techniques made possible for the contribution of the various boundary layer events to the unsteady loads and delay in stall angle to be established and the stalling mechanism to be determined. The wake velocity profiles, mean and *rms*, were measured and used to correlate the boundary layer events to the characteristics of the airfoil wake. Smoke flow visualization was also carried out to supplement the quantitative experiments and assist in the description of the boundary layer events.

Three main oscillation categories, corresponding to the attached-flow, light stall, and deep stall cases, were studied. It is anticipated that this work will contribute to a deeper

understanding of the complex behaviour of the unsteady separated flows and dynamic stall phenomena over an airfoil oscillating in pitch. The present work will also provide experimental test data for use with the validation process of computational methods.

2. BACKGROUND

Research into unsteady airfoils is quite extensive. This includes experimental, theoretical and numerical investigations. The majority of published works can be categorized based on the type or form of the unsteady motion, the most common of which are constant-pitching and oscillating in pitch motions. Furthermore, many researchers have focused their efforts on controlling the effects of the dynamic motion of the airfoil on the passing fluid.

2.1 Constant-Pitching Airfoil

A review of literature will identify the constant-pitching airfoil as a very popular unsteady motion that has been studied. This can be attributed to two factors. Firstly, it simulates the conditions of an aircraft during post-stall manoeuvring and also displays the dynamic stall characteristics inherent in the retreating blade dynamic stall problem of helicopter rotor blades. Secondly, it does not include a downstroke motion and thus simplifies the problem somewhat. In fact, Johnson and Ham [11] believe that it is a pitching airfoil, not an oscillating one, that best models a stalling rotorblade, however McCroskey, a name synonymous with retreating blade dynamic stall and unsteady airfoils, always studies oscillating airfoils, which implies the contrary.

As in the oscillating case, there are many parameters involved. The ones describing the motion of the airfoil are different from the oscillating case, namely the mean angle of attack, oscillation amplitude and reduced frequency are replaced by starting angle, stopping angle, and pitch rate, $\dot{\alpha}c/2U_\infty$ (where $\dot{\alpha}$ is the angular velocity, c is the airfoil chord and U_∞ is the free-stream velocity). The effects of these parameters, as well as others, on the phenomenon of dynamic stall have been studied and documented. The process of dynamic stall has also been considered.

The main experimental technique used to gather information about dynamic stall has been surface mounted pressure transducers distributed over the airfoil [8, 12, 13, 21]. These provide both the pressure distribution over the airfoil and, when integrated numerically, the

dynamic loads and moments. Also, limited use has been made of surface mounted hot film gauges [21], although with poor resolution, flow visualization and other techniques which will be discussed later.

A thorough description of the process of dynamic stall can be formulated from the various referenced works [8, 12, 13, 21]. Note that Francis and Keesee [8] have observed that the qualitative features of dynamic stall remain independent of pitch rate and amplitude and thus a general description follows. As the airfoil begins to increase in angle of attack, a separation point is seen to progress from the trailing edge towards the leading-edge region [13]. The pressure distribution resembles that corresponding to attached flow although the magnitudes surpass those of the equivalent steady flow values [8]. As this separation point reaches a quarter of the chord downstream from the leading edge, Jumper *et al.* [13] describe a "catastrophic" separation of the flow causing the formation of a large vortex in the leading-edge region. This vortex is seen as a large suction pressure peak [8]. Both the lift and profile drag coefficients, C_L and C_D, are seen to increase at a larger rate [13, 21]. The suction pressure peak shifts towards the trailing edge [8], an indication that the vortex has begun to convect downstream over the airfoil [13, 21]. At this point moment stall occurs [13, 21]. As the vortex travels over the airfoil it begins to grow and covers an increasing portion of the airfoil [8]. Subsequently, lift stall occurs and the maximum drag and minimum pitching moment coefficients are reached as the vortex is shed into the wake [21] resulting in a fully separated boundary layer.

The convection speed of the leading-edge vortex, U_{LEV}, has been estimated and results vary. Jumper *et al.* [12] indicate that Robinson *et al.* [35] found a convection speed on the order of 40% of the free-stream velocity whereas Lorber and Carta [21] found that the convection speed is a function of the pitch rate and varied from 13% to 33% of the free-stream velocity for nondimensional pitch rates of 0.001 and 0.02, respectively.

The effect of nondimensional pitch rate has been documented a great deal and has been found to be the dominant parameter. Increasing the pitch rate causes a delay in the development of the previously described flow events and consequently a delay in the dynamic-stall angle. It also strengthens the vortex and leads to increased maximum lift coefficient, C_{lmax}, and negative pitching moment, $C_{m,min}$. The pitch rate also seems to

influence the lift-curve slope, $C_{l\alpha}$, prior to the formation of the LEV although its exact relation seems uncertain. Francis and Keesee [8] have determined that the lift-curve slope increases with increased pitch rate, a finding which contradicts the results of Lorber and Carta [21] and Jumper *et al.* [13], which were determined through experimental and theoretical studies, respectively.

Studies of the effects of some of the other parameters have shown a weak dependence on Reynolds number and that at higher Mach numbers, the LEV is not as strong due to compressibility [21]. Also, Jumper *et al.* [12] have shown that the location of the pitching axis influences the flowfield and tends to delay the dynamic-stall angle as the pitching axis location moves downstream. Interestingly, Francis and Keesee [8] do show that their exists "a point of diminishing returns" and that stall is delayed at a lower rate at higher pitch rates than at lower pitch rates. Also, maximum performance is achieved when the pitching motion does not exceed the dynamic-stall angle (performance is defined as the area between the dynamic lift curve and maximum static lift value).

2.2 Harmonically Oscillating Airfoil

The harmonically oscillating airfoil, the focus of this work, is more complex than the previous airfoil motion in that the pitch rate is variable. In particular, the pitch rate for a sinusoidally oscillated airfoil is positive for half the cycle and negative for the rest, termed upstroke and downstroke, respectively, during which the pitch rate can be either increasing or decreasing. As such, the flow phenomena, although similar, require an in-depth analysis to fully understand the process of dynamic stall.

As in the previous subsection, various references allow the sequence of unsteady boundary layer events which occur throughout one oscillation cycle to be summarized [2, 14, 18, 20, 23, 24, 25, 28, 36]. An important detail that must be pointed out prior to discussing the dynamic stall process is that of flow separation. In the case of a steady airfoil, the locations of turbulent trailing-edge separation and flow reversal are one and the same, however for an unsteady airfoil these are two distinct points [2]. The following description applies specifically to a NACA 0012 airfoil which penetrates into the deep stall regime. The

reason for this will be discussed later. As the airfoil's incidence surpasses the static-stall angle, the boundary layer remains thin and there is no sign of flow separation [2, 20, 28], although the presence of a laminar separation bubble has been identified near the leading edge [2, 18, 25, 28]. With further increase in angle of attack, a thin layer of flow reversal appears at the trailing-edge region causing the boundary layer downstream of the flow reversal point to thicken [2, 14, 28]. Also, this portion of the boundary layer shows a wavy pattern due to the formation of eddies [2, 24, 28]. This flow reversal point travels towards the leading edge of the airfoil with increasing incidence [2, 24, 28], as does the laminar separation bubble [25]. The forward most position of the flow reversal point, as identified by Carr *et al.* [2] and McCroskey *et al.* [28], is approximately 30% of the chord downstream of the leading edge. At this point, a further increase in angle of attack leads to a sudden and immediate separation of the boundary layer upstream of the previously identified location of flow reversal [2, 18, 28]. This leads to the formation of a leading-edge vortex (LEV) [2, 18, 28]. This vortex convects over the airfoil at an approximate speed of 30% of the free-stream velocity, U_∞, according to Chandrasekhara and Carr [3], 35-40% of U_∞ according to Carr *et al.* [2] and McCroskey *et al.* [28], or 55% of U_∞ as Ericsson and Reding [7] have cited. The motion of the vortex causes both moment stall and an increase in the lift-curve slope [2, 25, 28]. As the cycle continues, lift stall occurs and finally a minimum in the moment coefficient is reached, indicating that the leading-edge vortex was shed into the wake [2, 23, 25, 28]. Some controversy exists concerning the position of the LEV at the moment of lift stall. McCroskey *et al.* [28] locates it at the midchord while Panda and Zaman [32] declares that loss of lift occurs when the LEV is shed into the wake. Note that since McCroskey *et al.* [28] based their findings on surface pressure distributions and Panda and Zaman [32] only conducted wake velocity surveys, the location corresponding to the results of McCroskey *et al.* may be more reliable. The flow at this point is fully separated, although a secondary vortex has also been observed to form and get shed into the wake after the LEV [2, 28, 32]. This somewhat smaller vortex is seen as a small pressure peak and produces small but noticeable peaks in the lift and moment coefficient curves [23, 28]. As the angle of attack decreases, reattachment eventually occurs near the leading edge and propagates downstream at a rate of about 25-35% of the free-stream velocity [2, 28]. It is interesting to note that it

has been found that the load and moment coefficient curves do not return to their unstalled values until the airfoil passes through its minimum angle of attack and the cycle restarts [2, 28].

With respect to the stalling mechanism, it has traditionally been thought to result from the bursting of the laminar separation bubble due to the forward motion of the flow reversal point, although this bursting has little effect on the dynamic loads [11]. The description provided above is mainly based on the work of Carr *et al.* [2] and McCroskey *et al.* [28] who found that, in general, dynamic stall resulted from the sudden breakdown of the turbulent boundary layer and that dynamic stall due to bubble bursting only occurred in special cases. This was determined by comparing the results of a regular NACA 0012 airfoil to one with modified leading edge geometries which promoted the formation of a bubble, noting that there were differences, and to a NACA 0012 airfoil with a boundary layer trip which completely eliminated the bubble, noting that the basic stall characteristics remained unaffected [2, 28]. This is the reason for which the description of the dynamic stall process provided above is specific to a NACA 0012 as other geometries may influence the stalling mechanism.

It has been observed that significant hysteresis in the aerodynamic loads only occurs when the airfoil oscillates in and out of stall [2]. However, hysteresis in the separation and reattachment or the transition and relaminarization points occur even for the light stall case [18]. Leishman [20] states that the lag in the reattachment of the fully separated flow is due to the "reverse kinematic induced camber effect on the leading edge pressure gradient by the negative pitch rate". He also affirms that the presence of hysteresis generates a reduction in aerodynamic damping.

As already stated, there are many parameters involved, each of which has a degree or level of influence on the fluid mechanics. Recall that, generally, the qualitative features of dynamic stall remain similar, although variations in the parameters do affect the details [20, 28]. The airfoil geometry has been found to be of lesser importance than the parameters describing the motion [29], although variations in geometry can be used to modify the loads, the dynamic-stall angle and the nature of the stalling mechanism, as discussed previously [28, 29]. McCroskey *et al.* [29] found that airfoils with enhanced static-stall characteristics

are inclined to exhibit better dynamic-stall characteristics, although this improvement quickly fades as the airfoils are subjected to deep stall. It seems that the effect of Reynolds number has not really been settled. Carr *et al.* [2] state that the effect of Reynolds number is small, and yet Martin *et al.* [23] declare that an increase in Reynolds number promotes the onset of dynamic stall, increases the maximum normal force coefficient and delays the angle at which the maximum normal force and minimum moment coefficients occur. Also, comparing the descriptions of the flow over an oscillating airfoil from experiments conducted at low Reynolds number (on the order 10^4) to those at high Reynolds number (on the order 10^6), there seems to be some disparity. Furthermore, an increase in the speed of the flow, in terms of the Mach number, seems to promote stall [3].

Focusing on the more dominant parameters, those describing the unsteady motion of the airfoil, a larger influence on the unsteady airfoil characteristics is observed. The effect of increasing the mean angle of attack is to shift the flow characteristics from the attached flow regime, to the light stall regime and subsequently the deep stall regime [20]. The oscillation amplitude partly controls the strength and timing of the leading-edge vortex [2]. Increasing the reduced frequency leads to a delay in the appearance of the flow reversal point and consequently, the formation of the leading-edge vortex and the dynamic stall process are deferred to later in the cycle [2, 3, 14, 23, 25, 28, 32]. In fact, for a sufficiently high reduced frequency, a value of 0.05 seems to be the dividing mark, stall can be averted until the downstroke part of the cycle [7, 28]. In addition, the strength of the LEV, and thus the peak load and moment coefficients, and the amount of hysteresis are increased [23, 25, 28].

The wake behind an oscillating airfoil is also of interest. McAlister and Carr [24] have noted that the wake vortex pattern in the dynamic case is stronger to that of a static airfoil. Also, the experiments of Park *et al.* [33], who measured the mean and *rms* wake velocity profiles, show that the location of the peak mean velocity deficit follows the motion of the trailing edge of the airfoil, although a phase lag was present. They also showed that an increase in the mean angle of attack caused an increase in the velocity defect, wake thickness and turbulence intensity. Interestingly, in the oscillation case of $\alpha=4°+7.4°\sin\omega t$, part of the cycle shows a large velocity deficit in the wake. They attribute this to the flow characteristics of deep stall even though the maximum incidence of the airfoil barely exceeds

the static-stall angle. Though this may be questionable, the velocity defect present is most probably due to the separation of the flow over the airfoil, although not to the degree that they allude to. On another note, Panda and Zaman [32] have developed a method of calculating the lift coefficient from the wake velocity field, although their results have been validated by few direct experimental measurements.

Looking at the theoretical or numerical studies performed with the goal of simulating numerically or solving theoretically the flow over an oscillating airfoil, it is evident that this is an important step in the evolution of the study of dynamic stall. To date, many studies have used a multitude of different techniques or means to theoretically or numerically study the flow and/or loads in the dynamic case, a small selection of which include references number [7], [13], [15], [26], [27] and [30]. Although their results are promising, they all possess some degree of inadequacy.

2.3 Theoretical Models

The work of Ericsson and Reding [7] constitute one of the many dynamic stall prediction efforts. Their work focuses mainly on the constant-pitching NACA 0012 airfoil. They describe unsteady stall as being composed of or characterized by two different flow phenomena, the first being quasi-steady in nature and the second being transient in nature. The first comprises a delay of stall due to time lag and boundary layer improvement effects. The second involves the forward movement of the separation point and the following "spillage" of a leading-edge vortex.

The time lag effects occur before a variation in the state of the flow can influence the separation-induced aerodynamic loads or due to the time that is required to convect the boundary layer reaction to a change in pressure gradient from the leading edge to the separation point. They suggest that the dynamic overshoot of the static-stall angle, α_{ss}, can be subdivided into two parts: $\Delta\alpha_{tl}$, which simply shifts the static characteristic in the $\alpha(t)$ frame due to a purely convective flow time-lag effect, and $\Delta\alpha_s = \Delta\alpha_{s1} + \Delta\alpha_{s2}$, which generates the large lift coefficient overshoot over the maximum static value. The contribution of $\Delta\alpha_{s1}$ comes from the forward motion of the separation point and the $\Delta\alpha_{s2}$

increment originates from the formation and shedding of the leading-edge vortex. The accelerated flow and moving wall or "leading-edge-jet" effects, as described by Ericsson and Reding, increase the tangential wall velocities and improve the boundary layer characteristics during the upstroke portion of the oscillation cycle. They both contribute to $\Delta\alpha_{s1}$, which results in a delay in flow separation to a higher effective angle of attack and a considerable overshoot of static stall. Once the static-stall angle has been exceeded by $\Delta\alpha_{sep} = \Delta\alpha_{tl} + \Delta\alpha_{s1}$, Ericsson and Reding propose that a massive separation of the boundary layer occurs, caused by the upstream motion of the separation point and the subsequent formation and convection of the leading-edge vortex. This formation and motion of the LEV dominate the lift increase and contributes to $\Delta\alpha_{s2}$. It is important to note, however, that Ericsson and Reding's model does not predict the presence of a thin layer of flow reversal in a thickened turbulent boundary layer, which has been experimentally identified, nor does it describe the nature of the leading-edge vortex, after its formation, as the cycle ensues.

Conversely, Jumper *et al.* [12, 13] studied the effects of the unsteadiness of the flow (neglecting the wake) and the motion of the airfoil in the directions, both, tangent and normal to the surface using a modified momentum-integral method. They validated the results predicted by the model against flow visualization and surface pressure measurements. Their results indicated that the increment in the lift coefficient for a NACA 0015 airfoil pitching at a constant rate about the midchord could be determined using the relation $\Delta C_l = 3.14\dot{\alpha}_{ND}[1 + 2/3(t/c)]$, where $\dot{\alpha}_{ND} = 0.5c\dot{\alpha}/U_\infty$ is the non-dimensional pitch rate and t/c is the thickness ratio. This increment is due to the rotation of the airfoil. They also found that the effect of the pitching motion on the coefficient of lift-curve slope, $C_{l\alpha}$, for a flat plate could be estimated by the relation $C_{l\alpha} \approx 3.6 + 2.68\exp(-\dot{\alpha}_{ND} \times 10^3 / 4.216)$. This is caused by the vortices being shed into the wake causing a "time lag" thus resulting in a higher lift coefficient in the unsteady case compared to the steady case for a given angle of attack. In their study of the effect of pitching axis location, they found that the slope of the coefficient of lift curve is independent of the location whereas the increment in the lift coefficient does depend on pitch location. It is of note that the momentum-integral method provides a way of studying the effect of the pitch location on separation.

2.4 Experimental Techniques

While researchers improve the theoretical and computational methods, there is a need for further experimental work so as to extend the level of understanding of unsteady separated flows and to provide those researchers with a means to validate their work. The bulk of experimental work has been focused on the measurement of the unsteady aerodynamic loads. Other experimental techniques which have been used by researchers include hot-wire anemometry, single surface-mounted heated wall-shear stress gages, laser Doppler velocimetry, surface pressure transducers, particle image velocimetry and flow visualization methods. These have been used to study the numerous critical flow points and stall events, which include: 1) the locations of boundary layer transition, separation (laminar and turbulent), flow reversal and reattachment; 2) the formation and growth of the leading-edge and secondary vortices; 3) the characteristics of the laminar separation bubble. Be this as it may, many of the previously mentioned techniques possess limitations or drawbacks.

Flow visualization is an invaluable tool which provides a description of the flow characteristics. Although it is primarily qualitative, quantitative measurements can occasionally be made. The use of surface pressure taps to describe the pressure distribution is a very popular technique as it offers a method of obtaining the aerodynamic loads, through integration of the surface pressures, and a description of the unsteady boundary layer. However, this usually requires a large model so as to accommodate the maximum number of orifices and internally mounted miniature pressure transducers, which is limited. Hot-wire probes are useful in determining the flow velocity (with no flow reversal) at any location although they are intrusive and only provide pointwise information. The laser Doppler velocimetry technique improves on this in that it is non-intrusive although it is still pointwise, relatively expensive and could possibly be limited to the poor signal-to-noise ratio and data rate near a surface. Particle image velocimetry conveniently provides global flowfield measurement although it is expensive and is not suited for studying the flow near a surface. Lastly, single surface-mounted heated wall-shear stress gages are non-intrusive and are capable of providing on-surface measurements of the shear stresses, as well as an

indication of flow state. The weakness of this technique is in the resolution of the measurements.

2.5 Dynamic Stall Control

Given the natural tendency of researchers to desire to control or manipulate something once the underlying physics have been understood, there have been many studies concerned with the control of the dynamic stall phenomenon. A few typical control methods are covered in references [4], [9], [10], [22] and [34].

Chandrasekhara *et al.* [4] designed a NACA 0012 airfoil whose leading edge could be dynamically deformed. They found that in order for control to be efficient, the shape or curvature of the leading edge should be transformed slowly to allow the flow to adjust. They also found that the leading-edge vortex could be completely eliminated by a particular leading edge shape, which remained constant. McCroskey *et al.* [29] also studied the effect that airfoil shape had on dynamic stall and the load coefficients. However, in their case they did not only vary the leading edge shape but used separate airfoils of varying geometry. They found that the airfoils with the better static-stall characteristics are liable to also have improved dynamic-stall characteristics.

Another technique used involves suction and/or blowing from slots, leading edge and flap-shoulder. Greenblatt *et al.* [9] found that excitation from the leading edge increased the maximum lift coefficient, prevented lift stall and decreased the magnitude of the minimum moment coefficient. Excitation from the flap-shoulder produced an increase in lift coefficient that was sustained throughout the cycle and eliminated moment stall. Similarly, Magill et al. [22] used pulsed vortex generator jets, located near the leading edge of the airfoil, and found that they could increase the maximum lift coefficient and prevent the large negative value of moment coefficient. Furthermore, a closed-loop control system, which only activated the jets when stall was about to occur, was able to produce the same increase in lift coefficient as an open-loop control system but used 75% less air.

Rennie and Jumper [34] used a trailing edge flap as a means of controlling the loads on an unsteady airfoil. In particular, they showed that their control system could constrain

the normal force coefficient to a value of approximately zero while the airfoil underwent a constant-pitch rate motion. Alternatively, Hsiao *et al.* [10] implemented a leading edge oscillating flap to improve dynamic stall characteristics. Their findings identify the vortex shedding frequency as the optimum excitation frequency of the flap. Furthermore, the larger the oscillation amplitude of the flap, the larger is the increase in lift coefficient, although there comes a point after which no further improvement is observed.

3. EXPERIMENTAL METHODS AND APPARATUS

3.1 Flow Facilities and Test Models

The experiments were conducted in the *Joseph Armand Bombardier* wind tunnel located in the Aerodynamics Laboratory of the Department of Mechanical Engineering of McGill University. This is a subsonic wind tunnel of open-return suction type, which is equipped with a specially designed acoustic silencer at the exit so as to reduce the high tone noise (Figures 3a and 3c). A combination of honeycomb and three anti-turbulence screens at the entrance produce a high quality flow with a turbulence intensity of 0.03% at a free-stream speed of 35 m/s (Figures 3b and 3c). This wind tunnel has a total length of 18.3 meters, a contraction ratio of 9.5 to 1 and a test section that measures 0.9 m × 1.2 m × 2.7 m. The flow speed is calibrated against the fan speed, which is precisely regulated by a digital controller. A smoke tunnel was also used to visualize the flow around the airfoil, which was recorded with a 60 Hz video camera at a shutter speed of 1/1000s.

The test models used in this experiment were fabricated from solid aluminum and machined into a NACA 0012 airfoil profile with a chord length, c, and span of 15 cm and 37.5 cm, respectively. This shape airfoil is typical of those used in experiments to simulate helicopter rotor blades [2, 3, 4, 5, 14, 18, 22, 23, 24, 25, 26, 30, 32, 33]. Circular end plates of 30 cm diameter with sharp edges fabricated from a transparent acrylic material were fitted to either end of the airfoil so as to ensure a two-dimensional flow distribution over the majority of the airfoil span [19]. The spacing between the endplates and the airfoil was kept to minimum in order to reduce the amount of flow through the gaps. The two-dimensional uniformity of the flow was verified by traversing a hot-wire probe, located at 10% of the chord downstream from the leading edge of the airfoil and 5 mm above it, along the span of the airfoil. This check resulted in a non-uniformity of ±4% of the free stream value. The airfoil was mounted horizontally in the wind tunnel using a support system, which was part of a specially designed mechanism used to oscillate the model sinusoidally (Figure 4). The mechanism, capable of oscillating the model at various mean angles, amplitudes and frequencies, consisted of a four bar linkage and flywheel. The mean angle of attack, α_m, was

varied by changing the rotating shaft at specific radial shaft-connector locations. The oscillation amplitude, $\Delta\alpha$, was adjusted by changing the position of attachment of the coupler to a circular disk which acted as the crank in the four bar mechanism. The oscillation frequency, f_o, capable of being set between 0 and 8.5 Hz, was done so by adjusting the power supply to a dc motor which drove a timing belt and pulley system. The pitching axis of the airfoil was located at ¼-chord, the approximate location of the aerodynamic center for angles of attack a few degrees below the static stall angle [20]. Also, McAlister *et al.* [25] found that the ¼-chord location is an appropriate pitch axis since the motion of the center of pressure during the stalled portion of the cycle are centred at about the ¼-chord. Jumper *et al.* [12] discuss the effect of the location of pitching axis location on dynamic stall.

The instantaneous angle of attack of the airfoil, $\alpha(t) = \alpha_m + \Delta\alpha \sin\omega t$ (where $\omega = 2\pi f_o$ is the circular frequency and t is time), and the phase reference signal, $\tau = \omega t$, were recorded using a potentiometer (TRW type DP 801) with an accuracy of $\pm 0.1^o$, which was coupled to the airfoil shaft. By connecting the output signal of the potentiometer to a Hewlett-Packard model HP 3582A spectrum analyser, the oscillation frequency was measured to an accuracy of ± 0.02 Hz.

Of the two models fabricated, one was covered with a sheet of multi-element hot film sensors, the details of which will be covered in the following section. The other model had 61 pressure taps, distributed over the upper and lower surfaces, machined into it. Note that this number of pressure taps is greater than that used by many researchers [2, 5, 12, 13, 23, 25, 28, 29, 34]. In conjunction with seven fast-response miniature pressure transducers (Type YQCH-250-1), this allowed for the surface pressure distributions to be acquired. The orifices had a diameter of 0.35 mm and were staggered 1.5 mm apart in the streamwise direction so as to avoid the wake effect of each orifice on the ones downstream, also done by Chen and Ho [5]. The positions of the pressure taps are illustrated in Figure 5.

3.2 Multi-Element Hot-Film Sensor (MHFS) Array

The unique hot-film sensor arrays provide a non-intrusive method of simultaneously identifying the various boundary-layer and stall events. The MHFS array that was created

consisted of 140 sensors that were arranged in a straight-line pattern with spacing, s, of 1.25 mm. The fabrication process consists of overlaying a 8 μm thick sheet of copper over a 2 μm thick sheet of nickel which is placed on top of a 50 μm thick polyimide substrate. A specially designed template is then used to electron-beam evaporate the copper and nickel onto the polyimide substrate into the required pattern as illustrated in Figure 6. This generates an array of nickel sensors with copper coated nickel leads which allow magnet wire to be attached at either end of the leads and taken out through the endplates without disturbing the flow (Figures 6b and 4c). The sensors have a nominal resistance of 8 ohms and have dimensions: 2 μm thick, 0.1 mm wide and 2 mm long. The MHFS array was then adhered to the model surface using double-sided Mylar tape (50 μm thickness) which prevented any surface deformities from occurring. Sensors 1 to 121 ($S_1 - S_{121}$), sensor 122 (S_{122}) and sensors 123 to 140 (S_{123}-S_{140}) were located on the upper surface, the leading edge stagnation point (LESP) when the airfoil is at an incidence of zero degrees, and the lower surface, respectively. Note that the sensor numbers indicate their locations along the airfoil surface, and is proportional to the distance covered from the leading edge stagnation point. Also note that although the sensors introduce a surface roughness to the airfoil of 10 μm, this is a great deal smaller than the critical roughness height required to trip the laminar boundary layer, and their effect will therefore be neglected in this study. Similar multi-element hot-film sensor arrays were used and described by Lee [16], Lee and Basu [17, 18] and Lee and Gerontakos [36].

3.3 Instrumentation and Data Processing

Three sets of measurements, excluding flow visualization, were conducted throughout this experiment. Data acquisition and post processing for each set was carried out on a Pentium II PC with a 16 bit A/D converter board. Figure 7a shows a picture of the experimental set-up which includes the various components used to acquire and process the data. The block diagram of the experimental set-up and the instrumentation system, including data acquisition and processing system, is depicted in Figures 7b, 7c and 7d.

3.3.1 Surface Pressure Measurements

The pressure transducers that were used had a dynamic range on the order of 10 kHz, far greater than that which was required. The output signals from the pressure transducers were low pass filtered at 250 Hz, amplified using a multi-channel AA Lab model G3006 pressure measurement system and sampled at a rate of 200 Hz. The pressure transducers were calibrated against a water column manometer (WS-Minimeter model A-0702-89), the result of which was a relation between pressure transducer voltage output and absolute pressure.

As described previously, surface pressure distributions were obtained using a model airfoil which had 61 pressure orifices distributed over its surface. Tygon tubing was used to connect these orifices, which had brass inserts, to the external pressure transducers. In the case of the static airfoil, only one pressure transducer was used in conjunction with a scanning valve mechanism. This mechanism provides 48 inputs and a single output that is connected to the pressure transducer. It can scan through the inputs one at a time or all very quickly. This allowed the input to the pressure transducer to be easily shifted between pressure orifices, although the remaining 13 pressure taps, which could not be connected to the scanning valve, had to be connected to the pressure transducer manually. For each orifice the output signal of the pressure transducer was sampled for 10 seconds, converted to pressure, and a mean value was calculated and recorded before proceeding to the next orifice. This was carried out for various angles of attack between zero and twenty degrees.

In the case of the dynamic, or oscillating, airfoil, the use of the scanning valve was impractical and so the data was acquired in batches. As a result of the availability of seven pressure transducers, data for only seven pressure taps could be taken simultaneously along with the phase information provided by the potentiometer. Data was taken for between 30 and 100 cycles of oscillation, depending on reduced frequency. Once all the data was acquired, the post processing consisted of phase-averaging the data and numerical integration so as to generate the unsteady aerodynamic loads and pitching moments.

For the oscillating cases it was important to determine what effect, due to compressibility, the 18-cm long and 0.75-mm i.d. Tygon tubing, which separated pressure tap

from pressure transducer, had on the unsteady pressure signals. This was done using a method described by Chen and Ho [5], Lee and Basu [17] and Rennie and Jumper [34]. It consisted of exposing a pressure transducer to a controlled acoustic sound source and comparing its output (i.e. magnitude and phase) to the sound source. The apparent effect is a simple time lag in all pressure signals with frequency above 2.95 Hz, and sets a limit in the reduced, or nondimensional oscillation, frequency, $\kappa = \omega c/2U_\infty$, of 0.0993 at a Reynolds number of 135,000. As a result, the curves of lift, pressure drag and pitching moment, for any case with reduced frequency above this limit can only be used qualitatively.

3.3.2 Hot –Wire Wake Measurements

The wake of the airfoil at a distance of one chord downstream from the trailing edge was examined using a 5-μm-diameter miniature hot-wire probe (DISA P11) with a Dantec 56C17 constant-temperature anemometer (CTA). The overheat ratio was set at 1.6 and the signal was low-pass filtered. This probe, supported by a sting, was mounted on a six-axis computer controlled traversing mechanism, portrayed in Figure 8, which allowed for precise positioning of the probe. The position along the vertical axis was accurate to within 5 μm. The hot-wire probe was calibrated versus wind speed and its signal was sampled at 2 kHz. Instantaneous wake velocities, for 100 to 150 cycles of oscillation, were recorded and phase-averaged to yield the mean and fluctuating velocity fields at various points during the oscillation cycle. It is important to note that as a single wire, this velocity data contains not only the u-component of the velocity but the total magnitude of the velocity. Similar wake measurements were conducted by Park *et al.* [33], but for different oscillation cases, and Panda and Zaman [32] performed wake surveys using a cross-wire probe.

3.3.3 Multi-Element Hot-Film Sensor Measurements

Being limited by the 16 channels on the A/D board, one channel of which being reserved for the potentiometer output which provided a reference signal, the 140 hot-film sensors were sampled in batches of 15. Fifteen AA Lab model AN-2000 constant-

temperature anemometers (CTAs) were used to obtain the time history of the wall shear stress at each sensor location. BNC cables were used to connect the sensors from their magnet wire to the constant-temperature anemometers. To ensure that only a small amount of heat was introduced, with the goal of minimizing their effect on each other or the boundary and shear layer, the overheat ratio was set to 1.09. By observing the outputs of sensors that were heated individually and in groups, the previously mentioned effect was verified and found to be negligible. To simplify the post processing and analysis of the data, the operating conditions of each hot-film sensor, which includes the overheat ratio and dc offset voltage, were set to be nearly the same. The signals generated by the CTA's were low-pass filtered, amplified and sampled at a frequency of 2kHz. The conditioned signal was also sent to a four-channel oscilloscope (LeCroy model 9304) which provided on-line time history traces of four of the fifteen operating sensors. Similar set-ups were used and are described by Lee and Basu [18] and Lee [16].

An important yet difficult aspect of the multiple hot-film sensors is their calibration. In this experiment, the goal was to identify the critical flow points. This is done by evaluating and comparing the qualitative behaviour of the sensor signals and not the absolute values of the wall shear stresses. This alleviated the need for the calibration of each individual hot-film sensor and the difficulties that are inherent in this task as described by Desgeorges *et al.* [6]. Note that the comparison required the signals be self-scale normalized to a peak-to-peak value of one.

As was mentioned earlier, the critical flow points, or boundary-layer events, can be identified by the qualitative behaviour of the sensor outputs. It is important to note that the static and dynamic airfoils are analysed differently. In fact, the dynamic oscillation of the airfoil facilitates the identification of the critical flow points due to its transient nature. The description of the identifying features of the various boundary-layer events will be provided in the respective sections which discuss them. Lastly, it is important to note that the hot-film sensors have the unique capability of identifying the presence and the spatial-temporal progress of the boundary-layer events.

3.3.4 Smoke Flow Visualization

Smoke flow visualizations of the behaviour of the flow over a static and an oscillating airfoil were conducted with two goals in mind. The first and most important was a qualitative examination and understanding of the spatial and temporal progression of the critical flow points which occur over the airfoil. The second was a quantitative investigation of the position of the turbulent boundary layer flow separation near the trailing edge of the static airfoil. After the flow visualization was captured on videotape, a frame grabber was used to digitize various images from the video. The flow visualization technique used a 50 μm Nicrome wire coated with SAE W-40 oil which was burned, producing smoke, using a Variac transformer.

3.4 Test Parameters

The test parameters that were considered for the dynamic airfoil were the three variables which describe its oscillatory motion, these being the mean angle of attack, α_m, oscillation amplitude, $\Delta\alpha$, and reduced frequency, κ. The benchmark data to which the results of the dynamics cases would be compared, the static case, only had the angle of attack vary. Note that all experiments were run at a Reynolds number of 135,000 based on airfoil chord. The ranges of mean angle of attack and oscillation amplitude were chosen so as to thoroughly encompass the conditions of oscillating within, around and well beyond the static stall angle. As described by Leishman [20], the flow can be divided into three categories with respect to reduced frequency. The flow can be considered quasi-steady, unsteady and highly unsteady for reduced frequencies below 0.05, between 0.05 and 0.2, and above 0.2, respectively. The reduced frequencies chosen were, based on this, 0.025, 0.05, 0.1 and 0.2. Note that only the multi-element hot-film sensor experiments were run at a reduced frequency of 0.2 since the pressure data was limited to a value of reduced frequency nearing 0.1. To simplify the discussion of the results, focus will be placed on only one representative case for each flow regime. These are: 1) attached flow: $\alpha(t) = 0^\circ + 7.5^\circ \sin\omega t$ with $\kappa = 0.05$; 2) light stall: $\alpha(t) = 0^\circ + 15^\circ \sin\omega t$ with $\kappa = 0.05$; and 3) deep stall: $\alpha(t) = 10^\circ + 15^\circ \sin\omega t$ with

$\kappa = 0.01$. Some results for additional test cases will be presented in Appendix B. Table 1 specifies, by way of black dot, the combinations of mean angle of attack and oscillation amplitude that were covered. These represent at total of 36 – 48 cases for each measurement technique.

Table 1: Test Parameters

α_m \ $\Delta\alpha$	5°	7.5°	10°	15°
0°	●	●	●	●
5°			●	●
10°	●		●	●
15°	●		●	●

κ	0.025	0.05	0.1	0.2

4. RESULTS AND DISCUSSION

This chapter presents and discusses the experimental results obtained from the aforementioned four experimental techniques used, namely multiple hot-film sensor measurements, surface pressure measurements, smoke-flow visualization, and wake velocity surveys. Two sections, with the latter subdivided into three sections, divide this chapter into steady and unsteady airfoils. In Section 4.1, the general behaviour of the boundary layer and aerodynamic loads of a static airfoil positioned at different angles of attack will be discussed, paying particular attention to the motion of the critical flow points and the stalling mechanism. Section 4.2 discusses the unsteady boundary layer and stall events as well as the dynamic loads developed on an airfoil oscillated harmonically in pitch, and is subdivided into attached flow, light stall and deep stall cases. Particular attention is given to the characteristics of the boundary layer and aerodynamic load curves, and also the effects of the oscillation parameters on these.

4.1 Static Airfoil

The characteristics of a static NACA 0012 airfoil were studied first in order to assist in the study of the unsteady boundary layer and stall events of an airfoil oscillating harmonically in pitch and to provide a frame of reference for the dynamic airfoil results. This includes the study of the critical boundary-layer flow points, which include the leading-edge laminar separation and peak transition points, and the trailing-edge turbulent flow separation point, the aerodynamic loads, and the wake velocity profiles.

Figure 9a shows the movement of the locations of leading-edge laminar separation and peak transition, and trailing-edge turbulent flow separation points with increasing incidence at a Reynolds number of 135,000. Agreement between three of the experimental techniques (i.e., multiple hot-film sensors, pressure measurements and flow visualization) presents itself quite readily in the fact that both the rear-to-front progression of the critical flow points and the lift-curve slope, $C_{l\alpha} = 0.08$ per degree, are linear for angles of attack below 10 deg, the angle which marks the beginning of the pre-stall loss of lift (Figure 9b). However, the rates of progression of the three critical flow points, which are roughly

0.03125, 0.117 and 0.047 for the laminar separation, peak transition and turbulent separation points, respectively, are different. Furthermore, for angles of incidence greater than 10 deg, both the progression of the critical flow points and the slope of the coefficient of lift varied nonlinearly and rapidly.

The hot-film measurements also show that for angles of attack below 6 deg, the boundary-layer transition to turbulence occurred by the mechanism of laminar instability (i.e., the growth of the Tollmien-Schlichting instability), similar to that found on a flat plate, and that for angles of attack greater or equal to 6 deg, transition was preceded by a separation of the laminar boundary layer and the separation bubble came into the picture (i.e., transition to turbulence by the mechanism of a short separation bubble). The details concerning the technique used to identify the laminar separation and transition locations are illustrated in Figures 10a and 10b and are discussed later on. It is evident, from Figures 9a and 9c, that the laminar separation bubble decreased in length and moved towards the leading edge as incidence was increased. Johnson and Ham [11], McAlister *et al.* [25] and O'Meara and Mueller [31] also found the laminar separation bubble to travel upstream with increased incidence. Confirmation of the presence of the laminar separation bubble was provided by the presence of plateaus in the surface pressure distributions for angles below 13 deg (Figure 9d), which also provided a means of estimating the length of the bubble. It is of note that the bubble lengths, estimated from both the multiple hot-film sensors and the surface pressure distributions, are similar. For angles greater than 13 deg, the boundary layer, as indicated by the flat surface pressure distribution, completely separated from the leading edge, corresponding to a sharp static stall at an angle of 13 deg (Figures 9d and 9b). This leads to the conclusion that for a static NACA 0012 airfoil at a Reynolds number of 135,000, the stalling mechanism is of a sharp leading-edge stall type and was triggered by bubble bursting. Carr *et al.* [2] came to a similar conclusion, although their Reynolds number was much higher (on the order of 10^6).

In Figures 10a and 10b, outputs of a few of the hot-film sensors have been selected and illustrated so as to demonstrate the non-intrusive technique used to identify the laminar separation point, the state of the boundary layer and the peak transition point. The numbers shown on the right side of the sensor outputs correspond to the sensor numbers as well as the distance over the surface, s/c, from the leading edge. In Figure 10a the hot-film voltage

output levels are self-scale normalized to a peak-to-peak value of 1 whereas in Figure 10b they are not. The laminar separation point was recognized directly from the 180° out-of-phase phenomenon, which occurred across sensors in the leading-edge region. It is obvious from Figure 10a that there existed an 180° phase shift between sensors S_{108} and S_{109}, locating the laminar separation point at a distance of approximately 11.3% of the chord from the leading edge. The leading-edge turbulent reattachment and trailing-edge turbulent separation points could not be detected with these sensors due to the random, wide-band frequency content of the turbulent surface shear-stress signals. Alternatively, the flow visualization pictures allowed the trailing-edge turbulent separation point to be located, although this was not possible for the leading-edge turbulent reattachment point due to the small size of the laminar separation bubble. Figure 10b displays the normalized hot-film outputs for different boundary layer states. It shows that the output corresponding to a laminar boundary layer had low voltage amplitudes (sensor S_{114}). With increasing instability in the boundary layer, periodic turbulent bursts began to appear with an associated increase in the hot-film output *rms* (root-mean-square) values, indicating the beginning, or onset, of the transition process (sensor S_{105}). Peak transition was identified as being the point at which the *rms* value reached a maximum (sensor S_{98}). This was followed by a turbulent boundary layer, which was characterized by a small decrease in the *rms* level (sensor S_{96}). The onset and end of transition was found to generally cover approximately 4-5% of the airfoil chord length. As previously mentioned, the interpretation of the hot-film sensor outputs for a dynamic airfoil is more straightforward due to the fact that the changes between flow states are more readily identifiable than in the steady case.

Figure 11 displays smoke flow visualization pictures for angles of attack between 2 and 20 degrees. From these pictures, the state of the boundary layer at the given angles of attack can be seen. Although the laminar separation bubble is too small to be seen (similar to the observations of Martin *et al.* [23], who were also unable to see the bubble in their flow visualization experiments), the trailing-edge turbulent separation point is visible and, as described above, its motion with increased incidence was evaluated. From the information gathered from the multiple hot-film sensors and the flow visualization pictures, a schematic diagram of the boundary layer over a NACA 0012 airfoil at an angle of attack between 6 and 13 degrees, and Reynolds number of 135,000 is illustrated in Figure 1. On the lower surface,

the boundary layer consists of a stagnation point just aft of the leading edge and a small region of separated flow near the trailing edge. On the upper surface, moving from the leading edge towards the trailing edge, the boundary layer consists of laminar flow that, due to an adverse pressure gradient, separates from the surface becoming a separated laminar shear layer. This shear layer undergoes transition to turbulence and consequently the turbulent shear layer is able to reattach. These points encompass a region of recirculating, or reverse, flow. The turbulent boundary layer will remain attached to the airfoil up to a certain point at which it separates. The motion of these points with increasing incidence was described above. Further insight into the flow over a static airfoil was obtained from the wake velocity survey.

The wake behind the static airfoil was characterized by both the mean and *rms* velocities. The mean wake velocity, U, consisted of a region of velocity deficit whose magnitude and size increased with larger angle of attack (Figure 12a). This trend was also seen in the profiles of the *rms* wake velocity, u′, which, in addition, possessed two local minima separated by a small distance. As the angle of attack was increased, there came a point when a severe increase in both the width and magnitude of the velocity deficit was observed. This, as expected, marked the angle at which stall occurred. It is interesting to note that as the angle of attack was increased, and hence the location of the trailing edge moved with respect to the centerline at y/c = 0, the centers of the profiles, both the mean and *rms*, followed its motion until stall occurred, at which point the centers shifted up to approximately the centerline and subsequently, with a further increase in angle of attack, remained fixed.

In summary, for a static NACA 0012 airfoil at a Reynolds number of 135,000, the critical flow points, which include the laminar separation, peak transition and trailing-edge turbulent separation points, along with the lift curve show a linear variation with increased incidence for angles of attack below 10 deg, which corresponds to the pre-stall loss of lift. Following this the variations become nonlinear, up to the static-stall angle of 13 degrees. Transition to turbulence was caused by the Tollmien-Schlichting instability for angles of attack below 6 deg and by the transition of separated laminar shear layers for angles greater or equal to 6 deg. Lastly, the stalling mechanism was determined to be of sharp leading-edge stall type and was triggered by the bursting of the laminar separation bubble.

4.2 Oscillating Airfoil

The behaviour of the unsteady boundary layer events developed on the upper surface of a NACA 0012 airfoil oscillated sinusoidally was investigated. Oscillations within, through and well beyond the static-stall angle (α_{ss} = 13 deg), corresponding to the attached flow, light and deep stall, respectively, were performed. Note that for each flow regime, the results of a single oscillation case, which is representative of that regime, will be presented in detail.

4.2.1 Airfoil Oscillating Within the Static-Stall Angle

The oscillation case which is representative of the attached flow regime is described by an oscillation about $\alpha_m = 0$ deg with $\Delta\alpha = 7.5$ deg amplitude ($\alpha(t) = 0^o + 7.5^o \sin\omega t$, where $\omega = 2\pi f$) at a reduced frequency, κ ($= \pi fc/ U_\infty$), of 0.05. Figures 13a and 13b illustrate the representative multiple hot-film sensor signals corresponding to this oscillation case. The lowest curve represents the variation in the potentiometer voltage and therefore the phase information. Recall that the sensor outputs are self-scale normalized. The various boundary layer events are identified from the trends in the sensor outputs. A relatively smooth signal indicated a laminar boundary layer whereas a signal with significant fluctuations was a sign of turbulence. Transition, which transformed a laminar boundary layer signal to a turbulent one, was determined from a rapid increase in the hot-film heat transfer level. The reverse was applied for its return back to a laminar state (i.e. relaminarization indicated by a drop in the hot-film heat transfer level). Note that this type of transition is of by-pass type as opposed to the instability mechanism and laminar bubble transition processes observed for a static NACA 0012 airfoil. The separation of the boundary layer, be it laminar or turbulent, was identified by a decrease in the overall hot-film signal, and vice versa for its reattachment. Lastly, the stagnation point was found due to the fact that, as a stagnation point, the local velocity is zero resulting in a reduction in heat transfer and thus a minimum in the hot-film signal.

The presence and motion of these trends allowed for detailed measurements of the boundary layer events that they represent. Referring to Figure 13a, transition and its return to a laminar flow state were apparent as the angle of attack increased and then decreased. It was found that transition was delayed relative to the static case and that the motion of the forward progressing transition and rearward travelling relaminarization points behaved in a non-linear manner (Figures 14a and 14b). The present measurements also indicated that, for an airfoil oscillated with the maximum angle of attack, α_{max}, below the static-stall angle, α_{ss}, (*i*) the flow remained attached throughout the cycle (except in the leading-edge region where the laminar separation bubble was present and the region close to the trailing edge where flow separation always persisted) and classical linear inviscid theory can be applied to approximate the airfoil's behaviour; (*ii*) there existed a wake vortex pattern, which was similar to the characteristics of the Karman vortex shedding, indicating the boundary layer on the airfoil was laminar; (*iii*) turbulence followed laminar separation and a small bubble was formed, as in the static case, at relatively high incidence; (*iv*) the laminar separation bubble (as indicated in Figure 13a by the line of laminar separation between sensors S_{114} and S_{109}) was shortened and had a bubble length, l_b, of 4.5% of the airfoil chord compared to a static value of 11% of the airfoil chord at an angle of 7.5 deg; (*v*) there existed a small hysteresis in the transition-relaminarization cycle; (*vi*) the lift coefficient versus incidence curve of the dynamic case led that of the static case and, compared to the static case, had a higher lift-curve slope, $C_{l\alpha}$ (= $dC_l/d\alpha$), but was accompanied by an increased moment coefficient, C_m (= $m_p/0.5\rho\, U_\infty^2 c^2$; Figure 15b); and (*vii*) the load hysteresis loops were narrow and there was little deviation of the coefficient of drag, C_d (= $d/0.5\rho\, U_\infty^2 c$), values from those of the static case.

The nature of the attached boundary layer flow at different instantaneous angles of attack can also be illustrated from the three-dimensional composite plots of the phase-averaged mean velocity and turbulence intensity profiles of the airfoil wake (Figure 12b). The sinusoidal hill of velocity deficit resulted from the periodic movement of the trailing edge, which also produced high-level turbulence intensity double peaks. Similar results were obtained by Park *et al.* [33], although at a significantly lower Reynolds number. Also, a comparison between Figures 12a and 12b show that for an oscillating airfoil whose maximum angle of attack is 7.5 deg, the wake thickness, velocity deficit and turbulence

intensity were similar to those of the static airfoil with incidence around 7 deg. Note, however, that there existed a phase difference between the motion of the trailing edge of the airfoil and the sinusoidal hill of velocity deficit and turbulence intensity, an observation also made by Park *et al.* [33].

Although the above generally describes the attached flow regime, a certain sensitivity to the oscillation parameters, specifically the reduced frequency, does exist. The primary effect of the reduced frequency in the attached flow regime was to delay the forward motion of the transition point (Figur 14a), and to allow the turbulent boundary layer to withstand this delay, without experiencing any flow reversal, at significantly larger incidence than would be possible for a static airfoil. As the reduced frequency increased, the onset of laminar-to-turbulent transition and its return to a laminar state were increasingly delayed and promoted, respectively, and the degree of hysteresis in this cycle was slightly reduced. Moreover, the laminar separation bubble was found to be inactive and its length remained insensitive to the reduced frequency. Observations made from the dynamic load loops, illustrated in Figure 15, show that for increased reduced frequency (*i*) the maximum lift coefficient showed little change; (*ii*) the lead of the dynamic lift coefficient versus incidence curve over that of the static case decreased; and (*iii*) the amount of hysteresis in the load curves increased. With respect to the wake profiles, the most significant influence that the reduced frequency had was to increase the phase delay between the motions of the airfoil and the velocity deficit.

In summary, for an airfoil oscillated below the static-stall angle, the boundary layer events were delayed non-linearly relative to the static case when the angle of attack was increasing (i.e., they occurred further downstream from the leading edge for a given angle of attack, or at a larger angle of attack for a given location on the airfoil). On the other hand, these events occurred earlier on the downstroke. The effect of the oscillation was to increase the lift-curve slope, lift coefficient and positive values of the moment coefficient relative to the static case, but the pressure drag coefficient remained comparatively unchanged. It is also interesting to note that the multiple hot-film sensor measurement of the instantaneous leading-edge stagnation point, identified by the locus of the minimum sensor voltages (indicated by the dashed lines in Figure 13b) in the leading-edge region of the airfoil, also provides an alternative means for determining a wing's instantaneous angle of attack and could be used as a wing-stall-warning indicator.

4.2.2 Airfoil Oscillating Through the Static-Stall Angle

As opposed to the previous case where the angle of attack never came close to the static-stall angle, in the light stall case the maximum angle of attack surpasses the static-stall angle to some extent. A typical light stall case, possessing both representative unsteady boundary layer and leading-edge vortex phenomena, is one with 0 deg mean angle and 15 deg amplitude ($\alpha(t) = 0^\circ + 15^\circ \sin\omega t$) at a reduced frequency of $\kappa = 0.05$. Referring to Figure 16, which presents flow visualization images at particular angles of attack, the sequence of events which occurred on the upper surface of the unsteady airfoil can be derived, though only qualitatively. As the airfoil pitched up, the first instance of flow reversal was observed at approximately 9.8 deg (Figure 16c), far later than in the static case, where separation occurred at 5 deg. This flow reversal point propagated gradually upstream towards the leading edge of the airfoil, reaching 40% of the chord downstream from the leading edge at an instantaneous angle of attack of 13.7 deg (Figure 16e). Immediately after oscillating through 13.7 deg, a vortex-type disturbance, termed the leading-edge vortex (LEV), of length approximately 30% of the chord formed close to the leading edge of the airfoil (Figure 16f). Simultaneously, a weaker vortex, termed trailing edge vortex (TEV), was also observed near the trailing-edge region, depicted schematically in Figure 16m. The leading-edge vortex was subsequently disrupted and shed downstream at approximately 14.2 deg on the downstroke (Figure 16h). The boundary layer remained separated over the rear half of the airfoil during the downstroke (Figure 16i), between approximately 13.3 deg and 9.78 deg, at which time it began to reattach. This reattachment point travelled downstream and full reattachment occurred towards the end of the downstroke at around –8.31 deg (Figure 16l).

The qualitative analysis above can be expressed quantitatively from the multiple hot-film measurements (Figure 17). Note that multiple cycles are shown to demonstrate the reproducibility of the measurements. Similar to the attached flow case, by-pass transition initiated near the trailing edge and travelled upstream (Figures 17 and 18b). Comparing its progress in both the light stall and static cases (Figure 18b), it is evident that, due to the unsteady motion, it is greatly delayed to higher angles of attack. Also, the existence of a slightly elongated laminar separation bubble, of length about 11.2% of the chord, can be

identified from sensors S_{118} to S_{105}. Note that in Figure 17, points 6 and 7 identify the laminar separation and reattachment points, respectively, at sensor S_{109}. Bearing in mind the signal trends used in the attached flow case to identify the various boundary-layer features, sensor S_{84} (Figure 17) provides a clear example of their application in the light stall case. Point 1 indicates by-pass transition from a laminar state to an attached turbulent state, which persists up to point 2. At point 3, the turbulent boundary layer separates and remains separated until reattachment begins at point 4. After the turbulent boundary layer has reattached, it returns to a laminar state, indicated by point 5. The progression of the reattachment and relaminarization points are presented in Figure 18c.

In addition to the hot-film sensor trends discussed in the section of the attached flow case, an additional feature is present. The presence of a significant, or noticeable, local minimum in the attached turbulent flow signal is indicative of the occurrence of flow reversal, characterized by a thin layer at the bottom of a thickened turbulent boundary layer. As indicated in Figure 17, flow reversal, denoted by the open triangles, first occurred near the trailing edge and rapidly progressed towards the leading edge, also shown in Figure 18a, with increased incidence. Once the flow reversal point reached the location marked by s/c of 0.4 (Figure 18a), or a surface distance of 40% of the chord downstream from the leading edge, a turbulent separation at a surface distance of 30% of the chord downstream from the leading edge followed (Figures 17 and 18a). A vortex, of approximate length 30% of the chord, was seen to form immediately afterwards at an angle of attack of about 14.4 deg between sensors S_{118} and S_{87}, however this vortex had little time to grow and was disrupted once the maximum angle of attack had been reached. Note, from either Figure 17 or by comparing Figures 18a and 18c, the presence of a significant phase lag or hysteresis in the separation, or flow reversal, and reattachment of the boundary layer flow, which ultimately leads to the observed growing hysteresis in the dynamic loads (Figure 19b).

Referring to Figure 19b, which presents the dynamic load curves for the oscillating case of 0 deg mean angle, 15 deg amplitude and a reduced frequency of 0.05, numerous characteristics are apparent. The degree of hysteresis, compared to the attached flow case, is larger, due to the hysteresis in the separation and reattachment points. Stall is delayed beyond the static-stall angle, by 1.6 deg for this specific case, and the maximum lift, drag and negative moment coefficients surpass their static case counterparts. Focussing on the lift

coefficient versus incidence curve, the overshoot in the maximum lift coefficient, $\Delta C_{l\max} = 0.56$, can be attributed to the presence and forward motion of the flow reversal, $\Delta C_{fr} = 0.38$, and the leading-edge vortex, $\Delta C_{l\text{LEV}} = 0.18$, although the contribution of the later was of secondary importance due to the lack of time for the leading-edge vortex to develop. The boundary between the two contributions was marked by the increase in the lift curve slope. On the other hand, as the angle for moment stall coincides with this boundary point, it can be concluded that the leading-edge vortex was the main contributor to the large negative peak in the moment coefficient, $C_{m,\min}$, of -0.02.

As in the attached flow case, the state of the boundary layer can also be deduced from the three-dimensional composite plots of the phase-averaged mean and *rms* wake velocity profiles (Figure 12c). As the oscillation cycle begins, the profiles resemble those of the attached flow case, signifying that the boundary layer was attached. At a certain critical angle of attack, there is a sudden increase in both the magnitude and width of the deficit in both the mean and *rms* profiles. As the airfoil's incidence continued to increase, there was a gradual return to a sinusoidal hill of velocity deficit. This suggests that flow separation occurred abruptly, causing an increase in wake width, but that reattachment proceeded more gradually. These findings are consistent with the results of the multiple hot-film measurements.

In this case of light stall, lift stall was found to be the result of the rapid trailing-edge stall. It was found that the instantaneous angle of attack at which trailing-edge stall occurred did not significantly diverge from the static-stall angle. Furthermore, moment stall occurred rather abruptly at the instant when the boundary layer separated from the airfoil near the top of the oscillation. This was followed by a negative contribution to the net aerodynamic damping during the initial part of the downstroke.

The influence of reduced frequency, as presented in Figure 18a, is to delay the occurrence of flow reversal and hence postpone the various boundary layer events. It is interesting to note, however, that the extent and abruptness of the separation did not vary considerably with reduced frequency. Furthermore, the effect of the reduced frequency on the hysteresis of the lift, drag and moment coefficient curves varies (Figure 19). As the reduced frequency is increased, the degree of hysteresis decreases, remains relatively unchanged and increases for the lift, drag and moment coefficient curves, respectively.

In summary, light stall shares some of the general features of classical static stall, such as loss of lift and significant increases in drag and nose-down pitching moment when the angle of attack exceeded a certain value. Also, an improvement in the lift and lift-curve slope similar to the attached flow case was observed. However, the behaviour of the light stall case was characterized by increasing hysteresis in the aerodynamic loads and pitching moments, caused by the asymmetry in the flow reversal and reattachment points. Furthermore, the effect of the leading-edge vortex, which was formed, was minimal due to its inability to grow and develop.

4.2.3 Airfoil Oscillating Well Beyond the Static-Stall Angle

For an oscillating airfoil that considerably exceeds the static-stall angle, the degree of complexity of the unsteady boundary layer and stall events is higher due to the upward motion of the flow reversal and turbulent breakdown, and the ensuing formation of a stronger leading-edge vortex. For this reason, the majority of experimental work has focused on oscillations which produce this deep dynamic-stall phenomenon. A representative oscillation case which possesses this complex behaviour is described by a mean angle of 10 deg, oscillation amplitude of 15 deg and reduced frequency of 0.10. The boundary layer features, representative of the deep stall regime, will be described for this typical oscillation case.

Figure 20 presents the representative multiple hot-film sensor signals for this oscillation case. Based on the trends described in the previous two sections, the majority of the flow features can be identified. Similar to the attached flow and light stall cases, the boundary layer transition and its relaminarization, which is of by-pass type, can clearly be identified from the sharp rise and fall of the hot-film levels during each cycle of oscillation. The boundary layer remained attached, except in the trailing-edge region, for angles of attack around the static-stall angle (α_{ss} = 13 deg). As opposed to the trailing-edge flow separation which the static airfoil suffered from, a flow reversal, characterized by a thin layer beneath a thickened turbulent boundary layer, occurred in the dynamic case for angles beyond the static-stall angle. The flow reversal, identified in Figure 20 by the symbol Δ, was initially observed at 12.9 deg on the upstroke at a surface distance from the leading edge of 88.4% of the airfoil chord (s/c = 0.884 or sensor S_{20}). With a further increase in angle of attack, this

flow reversal spread upstream gradually up to sensor S_{92}, located around the quarter-chord pitching axis, at an approximate angle of attack of 21.6 deg on the upstroke. Upstream of the flow reversal bifurcation point the boundary layer remained attached to the airfoil, between sensors S_{106} and S_{92} (s/c = 0.138 – 0.26), and was preceded by a laminar separation bubble, between sensors S_{188} and S_{111} (s/c = 0.034-0.095), of length 6.1% of the airfoil chord, significantly shorter than in the static case. Immediately following this, at an angle of attack of 21.8 deg on the upstroke, a sudden breakdown of the attached turbulent boundary layer took place at approximately a surface distance of 14% of the chord downstream from the leading edge. As in the previous oscillation regime, flow reversal was identified by the local minimum in sensors S_{20} to S_{92}. The turbulent breakdown was identified from the monotonic decrease in sensor S_{106}, located at s/c equal to 0.14, and is denoted by the ↓ sign. Note that due to the presence of random turbulent fluctuations, the flow reversal near the trailing edge (between sensors S_{18} and S_2) was intermittent and could not be identified.

As the airfoil's incidence continued to increase, the turbulent breakdown spread quickly, disrupting the laminar separation bubble and initiating the formation of a leading-edge vortex with a length of 10.4% of the chord at an angle of attack of 21.9 deg. The leading-edge vortex (LEV) grew and convected rapidly downstream with increased incidence for angles of attack between 21.9 deg and 24.4 deg. Near the top of the pitch-up motion, at an angle of 24.5 deg, the leading-edge vortex spanned 90% of the airfoil chord length. After this vortex passed off the airfoil, a secondary vortex was observed to form at an incidence of 21.8 deg during the downstroke and subsequently convected downstream. Both the leading-edge and secondary vortices were identified by local maxima in the sensor signals, caused by the enhanced mixing that they induce and hence improved heat transfer, and are identified by the symbols ▼and ∇, respectively. A short time after the secondary vortex passed off the trailing edge, the separated turbulent boundary layer began to reattach to the airfoil, at an angle of 14.1 deg during the downstroke, and became fully reattached once the airfoil reached an angle of attack of 1.1 deg. Furthermore, almost immediately after local reattachment occurred, the local boundary layer returned to a laminar state. Figure 21 presents the flow structure around the airfoil using flow visualization pictures.

The previously described boundary layer events can be described in more general terms while referring to flow visualization images and corresponding conceptual sketches

(Figure 21). As the airfoil motion began the upstroke portion of the oscillation cycle, the boundary layer was fully attached. As the angle of attack neared the static-stall angle, flow reversal occurred and spread upstream with increased incidence. At a certain critical angle, the attached turbulent boundary layer broke down causing a vortex to form in the leading-edge region (LEV). As the angle of attack increased further, this vortex grew and convected over the airfoil. At around the maximum angle of attack, the leading-edge vortex was shed into the wake causing the boundary layer to be fully detached from the surface of the airfoil. This detachment of the boundary layer persisted during the initial part of the downstroke motion until a point at which reattachment began near the leading-edge region and progressed gradually downstream with decreased incidence. Note that the presence of a secondary vortex, as identified by the multiple hot-film measurements, could not be ascertained from the flow visualization due to its weak nature (the fact that it is weak is determined from the dynamic load loops and will be discussed later). However, the generation and shedding of two distinct vortices from the upper surface of the airfoil have been observed by Martin *et al.* [23], McCroskey *et al.* [28] and Panda and Zaman [32]. With respect to the stalling mechanism, it is important to note that the multiple hot-film sensor signals concluded that the NACA 0012 airfoil did not stall due to bubble bursting, as observed in the static case where the sharp leading-edge stall was cause by the bursting of the laminar separation bubble. It began with an abrupt turbulent separation, a small distance downstream of the bubble reattachment point, which quickly travelled towards both the leading and trailing edges with increased incidence. Once it reached the bubble, it caused the bubble to burst thereby resulting in an abrupt breakdown of the flow field and the formation of a leading-edge vortex. The role of the bubble was merely to cause transition to turbulence for angles of attack equal to or greater than 6.5 deg. This stalling mechanism, although contrary to the beliefs of Johnson and Ham [11], agrees with the conclusions of Carr *et al.* [2], McAlister *et al.* [25] and McCroskey *et al.* [28]. The abovementioned boundary layer events are also reflected from the wake flow measurements shown in Figure 12d.

The composite three-dimensional presentation of the phase-averaged streamwise mean and fluctuating velocity profiles during one cycle of oscillation is presented in Figure 12d. It can clearly be seen that there is a significant variation in the wake thickness, velocity deficit and turbulence levels at different stages of deep stall. The various boundary layer

events can be categorized into six regions, labelled A through F. Regions A and B indicate the wake corresponding to the flow regimes of attached flow and the onset and end of the forward motion of the flow reversal, and were characterized by a narrower and more quiet turbulence field, compared to those of a static airfoil or regions C through E. Region C identifies the time interval during which the turbulent boundary layer thickens and breaks down causing the subsequent formation and convection of a leading-edge vortex. The wake flows in this region were characterized by a large increase in both the mean and fluctuating velocity profiles and the wake thickness. Region D represents the massive separation, due to the shedding of the leading-edge vortex, by way of a sharp increase in both the wake thickness and deficit and the velocity fluctuations as well. The process of flow reattachment during the downstroke portion of the oscillation is contained in the region labelled E. The wake flow characteristics returned to the unstalled values in region F. The variation in the wake thickness, velocity deficit and turbulence intensity at different angles of attack throughout the oscillation cycle are more clearly presented in the two-dimensional plots in Figure 12e. A more detailed description of the motion of the various critical flow points is presented in Figure 22.

Figure 22a shows that the unsteady transition point moved upstream gradually in a linear manner, similar to the static case, although comparatively it was delayed and at a lower rate of about 40% of the free-stream velocity ($d(s/c)/d\alpha = 0.145$). Figure 22b shows that the flow reversal also moved gradually upstream, at an approximate speed of 20% of the free-stream velocity (similar to the speed of the trailing-edge flow separation of a static airfoil prior to the pre-stall loss of lift), up to an uppermost position on the surface of about 26% of the chord downstream from the leading edge. Recall that for an unsteady airfoil, the locations of flow reversal and turbulent separation are two distinct points, as there can exist a turbulent boundary layer that has a region of reversed flow near the surface but does not show any significant variation in the boundary layer thickness nor any effect on the external free-stream. The detection, therefore, of the breakdown of the turbulent boundary layer could provide a sign of dynamic stall and possibly its control. The motion of the loci of both the leading-edge and secondary vortices, shown in Figures 22c and 22d, respectively, indicate that these vortices progressed downstream at estimated convection speeds of 45% and 30% of the free-stream velocity, respectively. Also, the reattachment point was found to

travel downstream at about 15% of the free-stream velocity (Figure 22e). Comparing Figures 22a and 22f and Figures 22b and 22e, the existence of hysteresis between the transition and relaminarization points and the unsteady separation and reattachment points, respectively, can be established.

In addition, by correlating the multiple hot-film sensor signals with the dynamic load loops computed from the surface pressure measurements, the variations in the lift, drag and moment coefficient curves, especially the stall angle delay and the lift increment, both before and during stall could be quantified. Figure 23 displays the dynamic lift, drag and moment coefficient curves and also identifies the various important points on those curves. Focusing on Figure 23a, detailed information can be obtained. Prior to occurrence of flow reversal, there is a slight increase in the lift coefficient, $\Delta C_{l\text{at}}$, of 0.12, due to the attached flow effect, but the lift-curve slope, $C_{l\alpha}$, remained relatively unchanged compared to the static curve. Furthermore, the lift-curve slope continued in a linear manner between points 1 and 2, corresponding to the onset and end of the upstream expansion of flow reversal, which occurred at angles of attack of 12.9 deg and 21.6 deg, respectively. However, there was a large increase in the lift coefficient, $\Delta C_{l\text{fr}}$, of 0.78 between these two points. A subsequent sudden rise in the lift, drag and negative moment coefficients, as well as the lift-curve slope, was observed with the occurrence of the turbulent breakdown and the ensuing initiation, growth and convection of the leading-edge vortex between points 3 and 4. The increment in the lift coefficient generated between points 3 and 4, $\Delta C_{l\text{LEV}}$, was 0.61, somewhat less than that generated between points 2 and 3. A total increment in the dynamic lift coefficient, $\Delta C_{l\text{max}}$, of 1.46 (which is composed of the individual abovementioned increments), compared to the maximum lift coefficient in the static case, $C_{l\text{max,ss}}$, of 0.92, was achieved. The lift coefficient underwent a severe drop once the leading-edge vortex almost completely passed off the trailing edge (the vortex was located at 90% of the chord downstream of the leading edge at the dynamic-stall angle, α_{ds}, of 24.7 deg), at point 4, and complete stall persisted until point 5. At point 6, corresponding to an angle of attack of 21.8 deg on the downstroke, a slight increase in the lift coefficient due to the presence and convection of the secondary vortex was observed. The extent of increase also indicated that the secondary vortex was not very strong. During post stall, the drop in the lift and drag coefficients persisted through the fully separated flow (points 6 – 7) until the boundary layer fully reattached to the airfoil

surface (point 8). Similarly, the drag coefficient did not begin its dramatic rise until the onset of flow reversal, corresponding to point 2, and the increment in the drag coefficient caused by the upstream motion of the flow reversal was 0.31. Once turbulent breakdown occurred and the leading-edge vortex formed and convected over the airfoil, an additional rapid increase in the drag coefficient was observed. A maximum drag coefficient of 0.91 at the dynamic-stall angle of 24.7 deg, identified by the symbol L at point 4, compared to a static-stall drag coefficient of 0.0625 for the static case was observed. There was a sharp decrease in the drag coefficient immediately following lift stall, between 24.7 deg of the upstroke to 24.2 deg of the downstroke, after which the drag coefficient returned to values comparable to those prior to the turbulent breakdown. Moment stall, corresponding to the angle at which the pitching moment coefficient suffered from a drastic drop and is denoted by M, occurred at the end of the upstream progression of the flow reversal (point 2). The accumulation of negative moment occurred concurrently with the increase in drag coefficient, reaching a peak at the moment of lift stall, or when the leading-edge vortex reached 90% of the airfoil chord downstream from the leading edge. The negative peak moment coefficient was 0.0395 compared to 0.006 for the dynamic and static cases, respectively. The considerable overshoot of the lift, drag and moment coefficients, compared to the static values, is attributed to the transient effects, as suggested by Ericsson and Reding [7], or to the apparent camber effects, as suggested by Jumper *et al.* [12].

Of the many parameters which can be varied, the reduced frequency, as other researchers and this study have found, is the most influential, especially in the deep stall regime where the unsteady boundary layer events are most pronounced. For this reason, special attention was given to the effects of the reduced frequency on the unsteady boundary layer and deep stall events, and the dynamic loads for the oscillation case described by a mean angle of 10 deg and oscillation amplitude of 15 deg (Figures 23 and 24). Figure 23 displays the dynamic load curves for three values of reduced frequency. From the lift coefficient curves, it can be seen that the difference in loads between the upstroke and downstroke diminishes with increased reduced frequency, although the return to unstalled values occurs later on in the cycle. Also, the peak loads (i.e. maximum lift, drag and negative moment coefficients) increase with larger reduced frequency as do both the lift and moment stall angles. This agrees with the observation that the wake flow structures decrease

with decreasing reduced frequency. Table 2 summarizes these values for this and other oscillating cases.

Figure 24a shows that for cases where the reduced frequency is below 0.2, the approximated linear rear-to-front progression of the flow reversal persisted, and was followed by an abrupt separation (denoted by the solid symbols) over the front portion of the airfoil. In addition, these phenomena occurred at successively later times and increased rates as the reduced frequency was increased. The locations of onset and maximum travel of the flow reversal were found to be insensitive to the reduced frequency. In other words, the flow reversal always developed near the trailing edge and travelled upstream reaching a maximum location on the surface of 26% of the chord downstream from the leading edge regardless of the reduced frequency, although the speed at which it travelled upstream was a function of reduced frequency. Also, when turbulent breakdown occurred, this was always observed at around 14% of the chord downstream from the leading edge, however at a delayed phase angle with increasing reduced frequency. The values of the delay in stall angle due to the progression of flow reversal, $\Delta\alpha_{fr}$, and the corresponding increment in the lift coefficient, ΔC_{lfr}, at different reduced frequencies are summarized in Table 2 and show an improvement with increased reduced frequency.

Figures 24b and 24c indicate the spatial-temporal movement of the leading-edge and secondary vortices, respectively, for reduced frequencies between 0.05 and 0.2. Increasing the reduced frequency caused a delay in the formation and rearward convection of both the leading-edge vortex and secondary vortex. At low reduced frequencies, the spillage of the leading-edge vortex occurred before the end of the upward pitching motion, while at reduced frequencies greater or equal to 0.2, this event was noticeably delayed and the convection of the leading-edge vortex occurred during the early stages of the downstroke motion. However, once the leading-edge vortex formed, it seemed to convect over the airfoil at the same rate of approximately 45% of the free-stream velocity, implying that no advantage was gained, in terms of confining the leading-edge vortex over the surface of the airfoil, by changing the reduced frequency. The vortex shedding phenomenon was not fundamentally different, but both its strength and its phase depended on the reduced frequency. The pre-stall increase in the lift-curve slope was, however, more obvious with increasing reduced frequency (Figure 23), and the post-stall continuous drop in the lift coefficient became much

less significant with decreasing reduced frequency. Similar to the leading-edge vortex, the downstream convection speed of the secondary vortex was also found to be insensitive to the reduced frequency and at a relatively constant value of about 30% of the free-stream velocity. Note that for reduced frequencies below 0.1 no secondary vortex was observed. The variation of the dynamic-stall angle, α_{ds}, and the delay in stall due to the formation and convection of the leading-edge vortex, $\Delta\alpha_{LEV}$, as well as the accompanied increase in the lift coefficient, ΔC_{lLEV}, with reduced frequency is presented in Table 2. A comparison of these values shows that the reduced frequency not only caused a systematic delay in the onset of dynamic stall, but also determined whether the airfoil stalled well before, near or after the maximum angle of attack was attained. The increasing delay in the onset of dynamic stall as the reduced frequency was increased is directly related to the delay in the forward movement of the trailing edge flow reversal and the turbulent breakdown.

Figures 24d and 24e show that the trend in the delay (or promotion) of the forward (or rearward) transition (or reattachment) points along the airfoil upper surface always displayed a linear behaviour, similar to that observed for a static airfoil for angles of attack less than 10 deg, but at a propagation rate insensitive to the reduced frequency. The phases or the instantaneous angles of attack at which the onset and end of the boundary layer transition and reattachment were observed, however, to be a strong function of the reduced frequency, which consequently caused a pronounced hysteresis in the transition and reattachment. Also, the laminar bubble length remained basically unchanged with increasing reduced frequency.

The influence of the oscillation amplitude, and consequently the maximum incidence, on the unsteady boundary layer separation was investigated by varying the magnitudes of the amplitude while keeping the mean angle and reduced frequency constant at values of 10 deg and 0.1, respectively (Figures 25 and 26). The airfoil exhibited both flow reversal and leading-edge turbulent separation for all the cases shown. However, for oscillation amplitudes between 10 deg and 20 deg, which correspond to deep stall cases, the deep dynamic stall was characterized by the movement of the flow reversal and turbulent separation, and a massive leading-edge vortex formed and developed, as a result of the breakdown of the boundary layer in the leading-edge region, and subsequently detached catastrophically. Similar to the case of the reduced frequency, the essential factor involved in these changes was the strength and timing of the dynamic stall vortex, while the position

where these phenomena were observed remained fixed irrespective of the variation in the maximum angle of attack. The deep dynamic stalling mechanism was of abrupt leading-edge stall type. For the light stall case, corresponding to an oscillation amplitude of 5 deg, the flow reversal moved to an uppermost on the surface of about 40% of the chord downstream from the leading edge and was followed by a turbulent breakdown at a distance from the leading edge of about 30% of the chord and the formation of a large vortex-like disturbance of about 30% of the airfoil chord in length with increasing airfoil incidence. The dynamic trailing-edge stall is responsible for the observed lift stall in this case. The effects of the amplitude are also revealed in the changes in the shape and magnitude in the dynamic load curves (Figure 26), however the basic phenomena, or trends, remained roughly the same. No significant difference in the maximum values of the lift, drag and negative moment coefficients was observed with changes in the oscillation amplitude as long as the maximum angle of attack was kept constant. A further increase in the mean angle (or in reduced frequency at the same values of mean angle and oscillation amplitude) produced additional increases in the vortex strength and in the peak values of the aerodynamic loads. The effects of the oscillation parameters (these being reduced frequency, mean angle, oscillation amplitude and maximum incidence) on the critical boundary layer flow points and the characteristics of the aerodynamic loads are summarized in Table 2.

In summary, the aerodynamic loads depend primarily on the time history of the angle of attack for the portion of the oscillation cycle where the angle of attack exceeded the static-stall angle. The dominant effect resulting from the gradual rear-to-front movement of the flow reversal and the formation and rapid convection of the leading-edge vortex was to produce values of the lift, drag and moment coefficients that were far in excess of their static counterparts. The dynamic vortex originated very close to the leading edge following moment stall, M, and produced a large negative pitching moment, high drag and an additional increment in the lift as it passed over the airfoil. However, it is worth noting that for flows described by a low Reynolds number, as in this study, the presence and upstream motion of the flow reversal contributed extensively to the increase in the lift and drag coefficients, but not to any noticeable variation in the moment coefficient. Furthermore, while it appeared that the dynamics of the laminar separation bubble played a significant role in the events of dynamic stall, the bubble itself had little effect on the aerodynamic loads, or

even the airfoil pressure distribution. The hysteresis observed in the dynamic load loops originated from the asymmetry in the locations, or angles of attack, of the separation and reattachment points. Moreover, although the boundary layer reattached all the way to the trailing edge well before the minimum angle of attack was reached, it was only after the next upstroke began that the loads returned to their unstalled values.

5. CONCLUSIONS

An experimental study of the behaviour of the unsteady boundary layer and dynamic loads developed on a NACA 0012 airfoil oscillated sinusoidally both below, through, and well beyond the static stall angle at a Reynolds number 135,000 was carried out by using a combination of experimental techniques, which include multiple hot-film sensor arrays, surface pressure measurements, smoke-flow visualization and wake velocity surveys. The results indicated that, in general, the unsteady motion improved the characteristics of the boundary layer and stall events and were highly influenced by the reduced frequency. Only small values of reduced frequency were required to delay the onset of the various boundary layer events and produce considerable deviations in the magnitudes of the peak values of the lift, drag and moment coefficients relative to the static case. Furthermore, the laminar separation bubble was shortened and played a passive role in the dynamic stalling mechanism, serving only to initiate transition to turbulence. Brief conclusions for both static and unsteady airfoils are drawn.

5.1 Static Airfoil

For a static NACA 0012 airfoil, the characteristics of the boundary layer and stall events can be summarized as:

a) The leading-edge laminar separation, laminar-to-turbulent transition and trailing-edge turbulent flow separation were found to propagate linearly towards the leading edge, although at different rates for angles below 10 deg, similar to the linear trend in the lift coefficient versus incidence curve prior to the pre-stall loss of lift, which occurred at 10 deg.
b) The boundary-layer transition process occurred by the mechanism of the Tollmien-Schlichting instability for angles of attack below 6 deg, and by the transition of separated laminar shear layers for angles greater or equal to 6 deg.

c) The transition process covered, in general, about 4 to 5 percent of the airfoil chord length.
d) The static-stall angle, α_{ss} = 13 deg, along with the surface pressure distributions and progression of the critical flow points, indicated that the static-stalling mechanism was of leading-edge stall type and was attributed to the bursting of the leading-edge laminar separation bubble.
e) The laminar separation bubble moved upstream and shortened with increasing airfoil incidence.

5.2 Oscillating Airfoil

5.2.1 Airfoil Oscillating Within the Static-Stall Angle

For the attached flow oscillating case, the results were found to be comparable to the static case, however, with small deviations, and are described as follows.

a) Boundary-layer transition and its return to a laminar state were delayed during the upstroke and promoted during the downstroke, respectively, in a nonlinear manner, relative to the static case, and produced hysteresis in that cycle.
b) The flow remained attached throughout the cycle (except in the leading-edge region where the laminar separation bubble was present and the region close to the trailing edge where flow separation always persisted) and classical linear inviscid theory can be applied to approximate the airfoil's behaviour.
c) The laminar separation bubble was shortened relative to the static case.
d) The aerodynamic forces and pitching moments followed the general trends of those of the static airfoil, however, there was a small improvement in the lift coefficient and lift-curve slope. This was accompanied by an increased moment coefficient and little deviation in the drag coefficient, relative to the static case.

e) The wake thickness, velocity deficit and turbulence intensity were similar to those of the static airfoil at similar angles of attack.
f) The primary effect of increasing the reduced frequency in the attached flow regime was to 1) increasingly delay and promote the forward motion of the transition and relaminarization points, respectively, reducing slightly the degree of hysteresis, and 2) to allow the turbulent boundary layer to withstand the delay in the transition point, without experiencing any flow reversal, at significantly larger incidence than would be possible for a static airfoil.
g) The laminar separation bubble was found to be inactive and its length remained insensitive to the reduced frequency.

5.2.2 Airfoil Oscillating Through the Static-Stall Angle

For the light stall oscillating case,

a) There existed a region of revered flow within an attached turbulent boundary layer, which travelled up to 40% of the airfoil chord downstream from the leading edge with increased incidence, and was followed by an abrupt turbulent breakdown at approximately 30% of the chord downstream from the leading edge during the upstroke as the airfoil neared the top of the oscillation cycle. A premature vortex-like disturbance, termed the leading-edge vortex, of length of about 30% of the chord was subsequently formed.
b) The growth of the vortex was cut short due to the change in pitch direction, and was shed.
c) Significant hysteresis in the unsteady lift, drag and pitching moment loops was observed, which was caused by hysteresis in the separation-reattachment cycle.
d) The stall angle was delayed relative to the static case and the maximum lift, drag and negative pitching moment coefficients surpassed their static case counterparts.

e) The increment in the lift due to flow reversal overwhelmed that due to the LEV, indicating the underdevelopment of the vortex, although the leading-edge vortex was the main contributor to the large negative peak in the moment coefficient.
f) There is a sudden increase in both the magnitude and width of the deficit in both the mean and *rms* profiles, which coincides with the turbulent breakdown.
g) Lift stall was found to be the result of the abrupt trailing-edge stall.
h) As reduced frequency was increased, there was a delay in the occurrence of flow reversal and hence postponed the various boundary layer events. Also, the degree of hysteresis decreases, remains relatively unchanged and increases for the lift, drag and moment coefficient curves, respectively.

5.2.3 Airfoil Oscillating Well Beyond the Static-Stall Angle

For the deep stall oscillating case,

a) The boundary layer prior to stall consisted of flow reversal which moved upstream at approximately a constant rate up to s/c equal to 0.26, independent of reduced frequency, and a subsequent abrupt turbulent breakdown at around s/c equal to 0.14. This led to the formation and ensuing growth and convection of a strong leading-edge vortex.
b) The events of flow reversal, turbulent breakdown and convection of the leading-edge vortex contributed to the observed overshoot in the lift, drag and pitching moment coefficient relative to the static values.
c) The leading-edge vortex and secondary vortex (secondary vortex only observed for reduced frequencies greater or equal to 0.1) convected downstream at 45% and 30%, respectively, of the free-stream velocity for all values of reduced frequency, suggesting that no "LEV-trapping advantage" was accomplished by changing the reduced frequency.

d) After lift stall occurred, the boundary layer underwent a process of reattachment of the separated turbulent flow followed by its return to a laminar state.

e) There existed a considerable hysteresis in the phases between the unsteady flow separation and reattachment points, which produced the observed large hysteresis in the dynamic load loops.

f) It was determined that the origin, strength and transient development of the leading-edge vortex and also the qualitative behaviour of the unsteady loads depended on all of the oscillation parameters, especially the reduced frequency.

g) There existed a delay in the trailing-edge flow reversal and leading-edge turbulent breakdown to large angles of attack with increased reduced frequency.

h) Moment stall occurred at the end of the upstream spread of flow reversal, while lift stall occurred when the leading-edge vortex reached 90% of the chord downstream from the leading edge.

i) It was found that dynamic stall, which was of leading-edge type, did not originate from the bursting of the laminar separation bubble, as is commonly believed, but with a sudden turbulent breakdown of the boundary layer in the leading-edge region.

6. REFERENCES

1. Bass, R.L., Johnson, J.E. and Unruh, J.F., "Correlation of lift and boundary-layer activity on an oscillating lifting surface," *AIAA Journal*, Vol. 20, No. 8, 1982, pp. 1051-1056.
2. Carr, L.W., McAlister, K.W. and McCroskey, W.J., "Analysis of the development of dynamic stall based on oscillating airfoil experiments," NASA TN D-8382, 1977.
3. Chandrasekhara, M.S. and Carr, L.W., "Flow visualization studies of the Mach number effects on dynamic stall of an oscillating airfoil," *Journal of Aircraft*, Vol. 27, 1990, pp. 516-522.
4. Chandrasekhara, M.S., Wilder, M.C. and Carr, L.W., "Unsteady stall control using dynamically deforming airfoils," *AIAA Journal*, Vol. 36, No. 10, 1998, pp. 1792-1800.
5. Chen, S.-H. and Ho, C.-M., "Near wake of an unsteady symmetric airfoil," *Journal of Fluids and Structures*, Vol. 1, 1987, pp. 151-164.
6. Desgeorges, O., Lee, T. and Kafyeke, F., "Multiple hot-film sensor array calibration and skin friction measurement," *Experiments in Fluids*, Vol. 32, 2002, pp. 37-43.
7. Ericsson, L.E. and Reding, J.P., "Fluid mechanics of dynamic stall Part I. Unsteady flow concepts," *Journal of Fluids and Structures*, Vol. 2, 1988, pp. 1-33.
8. Francis, M.S. and Keesee, J.E., "Airfoil dynamic stall performance with large-amplitude motions," *AIAA Journal*, Vol. 23, 1985, pp. 1653-1659.
9. Greenblatt, D., Neuburger, D. and Wygnanski, I., "Dynamic stall control by intermittent periodic excitation," *Journal of Aircraft*, Vol. 38, No. 1, 2001, pp. 188-190.
10. Hsiao, F.B., Liang, P.F. and Huang, C.Y., "High-incidence airfoil aerodynamics improvement by leading-edge oscillating flap," *Journal of Aircraft*, Vol. 35, No. 3, 1998, pp. 508-510.
11. Johnson, W. and Ham, N.D., "On the mechanism of dynamic stall," *Journal of the American Helicopter Society,* Vol. 17, No. 4, 1972, pp. 36-45.
12. Jumper, E.J., Dimmick, R.L. and Allaire, A.J.S., "The effect of pitch location on dynamic stall," *Journal of Fluids Engineering*, Vol. 111, 1989, pp. 256-262.
13. Jumper, E.J., Schreck, S.J. and Dimmick, R.L., "Lift-curve characteristics for an airfoil pitching at constant rate," *Journal of Aircraft*, Vol. 24, No. 10, 1987, pp. 680-687.

14. Kim, J.S. and Park, S.O., "Smoke wire visualization of unsteady separation over an oscillating airfoil," *AIAA Journal*, Vol. 26, No. 11, 1988, pp. 1408-1410.
15. Ko, S. and McCroskey, W.J., "Computations of unsteady separating flows over an oscillating airfoil," *AIAA Journal*, Vol. 35, No. 7, 1997, pp. 1235-1238.
16. Lee, T., "Investigation of unsteady boundary layer developed on a rotationally oscillating circular cylinder," *AIAA Journal*, Vol. 37, No. 3, 1999, pp. 328-336.
17. Lee, T. and Basu, S., "Nonintrusive measurements of the boundary layer developing on a single and two circular cylinders," *Experiments in Fluids*, Vol. 23, 1997, pp. 187-192.
18. Lee, T. and Basu, S., "Measurement of unsteady boundary layer developed on an oscillating airfoil using multiple hot-film sensors," *Experiments in Fluids*, Vol. 25, 1998, pp. 108-117.
19. Lee, T. and Birch, D., "The structure and induced drag of a tip vortex," To appear in *Journal of Aircraft*, Vol. 41, No. 1, 2004.
20. Leishman, J.G., "Principles of Helicopter Aerodynamics," Cambridge University Press, Cambridge, 2000.
21. Lorber, P.F. and Carta, F.O., "Airfoil dynamic stall at constant pitch rate and high Reynolds number," *AIAA Paper*, 87-1329, 1987, pp. 1-11.
22. Magill, J., Bachmann, M., Rixon, G. and McManus, K., "Dynamic stall control using a model-based observer," *Journal of Aircraft*, Vol. 40, No. 2, 2003, pp. 355-362.
23. Martin, J.M., Empey, R.W., McCroskey, W.J. and Caradonna, F.X., "An experimental analysis of dynamic stall on an oscillating airfoil," *Journal of the American Helicopter Society,* Vol. 19, No. 1, 1974, pp. 26-32.
24. McAlister, K.W. and Carr, L.W., "Water tunnel visualizations of dynamic stall," *Journal of Fluids Engineering*, Vol. 101, 1979, pp. 376-380.
25. McAlister, K.W., Carr, L.W. and McCroskey, W.J., "Dynamic stall experiments on the NACA0012 airfoil," NASA TP 1100, 1978.
26. McCroskey, W.J., "Inviscid flowfield of an unsteady airfoil," *AIAA Journal*, Vol. 11, No. 8, 1973, pp. 1130-1137.
27. McCroskey, W.J., "Unsteady airfoils," *Annual Revue of Fluid Mechanics*, Vol. 14, 1982, pp. 285-311.

28. McCroskey, W.J., Carr, L.W. and McAlister, K.W., "Dynamic stall experiments on oscillating airfoils," *AIAA Journal*, Vol. 14, No. 1, 1976, pp. 57-63.
29. McCroskey, W.J., McAlister, K.W., Carr, L.W., Pucci, S.L, Lamber, O. and Indergrand, R.F., "Dynamic stall on advanced airfoil sections," *Journal of the American Helicopter Society,* Vol. 26, No. 3, 1981, pp. 40-50.
30. McCroskey, W.J. and Philippe, J.J., "Unsteady viscous flow on oscillating airfoils," *AIAA Journal*, Vol. 13, 1975, pp. 71-79.
31. O'Meara, M.M. and Mueller, T.J., "Laminar separation bubble characteristics on an airfoil at low Reynolds number," *AIAA Journal*, Vol. 25, No. 8, 1987, pp. 1033-1041.
32. Panda, J. and Zaman, K.B.M.Q., "Experimental investigation of the flow field of an oscillating airfoil and estimation of lift from wake surveys," *Journal of Fluid Mechanics*, Vol. 265, 1994, pp. 65-95.
33. Park, S.O., Kim, J.S. and Lee, B.I., "Hot-wire measurements of near wakes behind an oscillating airfoil," *AIAA Journal*, Vol. 28, No. 1, 1990, pp. 22-28.
34. Rennie, R.M. and Jumper, E.J., "Experimental measurements of dynamic control surface effectiveness," *Journal of Aircraft*, Vol. 33, No. 5, 1996, pp. 880-887.
35. Robinson, M., Helin, H., Gilliam, F., Russell, J. and Walker, J., "Visualization of three-dimensional forced unsteady separated flow," *AIAA Paper*, 86-1066, 1986.
36. Lee, T. and Gerontakos. P., "Investigation of flow over an oscillating airfoil," *Journal of Fluid Mechanics*, paper in press.

Table 2 Effect of oscillation parameters on the critical unsteady aerodynamic values.

Oscillating case	κ	$C_{l,max}$	$\Delta C_{l,max}$	ΔC_{lat}	ΔC_{lfr}	ΔC_{lLEV}	L	α_{ds}	$\Delta\alpha_{fr}$	$\Delta\alpha_{LEV}$	α_1	α_2	$C_{m,min}$	$\Delta C_{m,min}$	M	C_{dmax}	ΔC_{dmax}
***Light stall*:**																	
$0^\circ + 15^\circ \sin\omega t$	0.025	1.38	0.46	0.00	0.23	0.23	13.3	13.3	3.3	1.2	8.6	12.0	-0.0175	-0.0135	13.0	0.31	0.248
	0.05	1.48	0.56	0.00	0.28	0.18	14.6	14.6	3.2	1.5	9.8	13.8	-0.020	-0.016	14.2	0.37	0.308
	0.1	1.57	0.65	0.00	0.65	---	14.9	14.9	3.8	---	11.0	14.9_d	-0.0175	-0.0135	14.8	0.37	0.308
	0.2*	---	---	---	---	---	15.0	15.0	3.8	---	11.3	14.7_d	---	---	---	---	---
$5^\circ + 10^\circ \sin\omega t$	0.025	1.33	0.41	0.00	0.20	0.21	13.1	13.1	3.0	1.2	9.0	12.1	-0.016	-0.012	12.0	0.26	0.198
	0.05	1.41	0.49	0.00	0.30	0.19	14.4	14.4	4.0	0.7	10.1	13.9	-0.019	-0.015	13.0	0.34	0.278
	0.1	1.51	0.59	0.00	0.59	---	14.9	14.9	3.2	---	10.6	14.9_d	-0.020	-0.016	14.3	0.36	0.298
	0.2*	---	---	---	---	---	15.0	15.0	3.3	---	10.8	14.7_d	---	---	---	---	---
$10^\circ + 5^\circ \sin\omega t$	0.025	1.30	0.38	0.00	0.20	0.18	14.0	14.0	2.9	0.9	10.2	13.0	-0.012	-0.004	13.1	0.26	0.198
	0.05	1.33	0.41	0.00	0.28	0.13	14.8	14.8	3.2	1.0	10.5	13.8	-0.014	-0.010	13.6	0.30	0.238
	0.1	1.40	0.48	0.00	0.48	---	14.9	14.9	3.0	---	12.0	14.9	-0.015	-0.011	14.7	0.302	0.258
	0.2*	--	---	---	---	---	15.0	15.0	3.2	---	12.2	15.0	---	---	---	---	---
***Deep stall*:**																	
$5^\circ + 15^\circ \sin\omega t$	0.025	1.53	0.73	0.17	0.28	0.28	15.2	15.2	4.2	1.8	9.2	13.4	-0.019	-0.015	13.2	0.43	0.368
	0.05	1.70	0.90	0.20	0.37	0.33	18.0	18.0	4.2	3.2	11.6	15.8	-0.025	-0.021	15.0	0.52	0.458
	0.1	2.02	1.22	0.23	0.50	0.49	20.0	20.0	4.2	3.0	12.8	17.0	-0.031	-0.027	17.5	0.77	0.708
	0.2*	---	---	---	---	---	21.4	21.4	4.3	3.1	13.0	18.2	---	---	---	---	---
$10^\circ + 15^\circ \sin\omega t$	0.025	1.47	0.67	0.08	0.34	0.27	17.5	17.5	5.1	2.1	10.5	15.5	-0.0215	-0.0175	15.1	0.425	0.363
	0.05	1.82	1.02	0.10	0.52	0.40	21.1	21.1	6.6	3.0	12.1	17.9	-0.0316	-0.0276	17.5	0.66	0.598
	0.1	2.44	1.52	0.12	0.78	0.61	24.7	24.7	8.4	3.5	12.9	21.1	-0.0395	-0.0350	21.6	0.91	0.823
	0.2*	---	---	---	---	---	23.8_d	23.8_d	9.4	3.6	16.5	24.1_d	---	---	---	---	---

CONTINUATION

$15^\circ + 15^\circ \sin\omega t$	0.025	1.51	0.71	0.08	0.42	0.21	20.1	20.1	6.1	1.9	12.1	18.2	-0.0196	-0.0156	17.5	0.50	0.438
	0.05	1.83	1.07	0.10	0.49	0.44	24.0	24.0	7.9	3.2	12.9	20.8	-0.0416	-0.0376	20.1	0.75	0.688
	0.1	2.18	1.38	0.15	0.73	0.50	28.7	28.7	8.1	4.7	15.9	24.0	-0.035	-0.031	23.3	1.10	1.038
	0.2*	---	---	---	---	---	28.8	28.8	8.2	4.7	15.9	24.1_d	---	---	---	---	---
$15^\circ + 10^\circ \sin\omega t$	0.025	1.31	0.51	0.05	0.33	0.13	18.6	18.6	4.7	1.9	12.0	16.7	-0.017	-0.013	16.9	0.414	0.352
	0.05	1.66	0.86	0.08	0.42	0.36	21.0	21.0	6.1	2.7	12.2	18.3	-0.026	-0.022	18.3	0.603	0.541
	0.1	1.97	1.17	0.12	0.53	0.52	24.0	24.0	6.3	3.8	13.9	20.2	-0.034	-0.0298	20.2	0.79	0.728
	0.2*	---	---	---	---	---	24.1_d	24.1_d	6.5	4.0	14.3	21.5_d	---	---	---	---	---
$15^\circ + 5^\circ \sin\omega t$	0.025	1.25	0.45	0.09	0.21	0.15	16.9	16.9	3.7	1.0	12.2	15.9	-0.014	-0.010	15.8	0.325	0.263
	0.05	1.43	0.63	0.11	0.28	0.20	18.0	18.0	3.2	2.0	12.8	16.8	-0.017	-0.013	17.0	0.40	0.328
	0.1	1.6	0.8	0.15	0.37	0.28	19.7	19.7	4.9	1.5	13.3	18.2	-0.021	-0.017	18.0	0.51	0.448
	0.2*	---	---	---	---	---	19.1_d	19.1_d	5.0	1.8	13.7	19.9_d	---	---	---	---	---

1) $C_{l\max}$ = maximum dynamic lift coefficient; $\Delta C_{l\max}$ = maximum lift increment = $\Delta C_{l\text{at}} + \Delta C_{l\text{fr}} + \Delta C_{l\text{LEV}}$; $C_{l\max,ss}$ = maximum static lift coefficient; $\Delta C_{l\text{at}}$ = lift increment due to attached flow effects; $\Delta C_{l\text{fr}}$ = lift increment due to flow reversal effect; $\Delta C_{l\text{LEV}}$ = lift increment due to LEV; L = lift stall; α_{ds} = dynamic stall angle; $\Delta\alpha_{fr}$ = angle delayed due to flow reversal effects; $\Delta\alpha_{\text{LEV}}$ = angle delayed due to LEV; α_1 and α_2 indicate the angles for the occurrence of flow reversal and turbulent separation denoted by points 1 and 2 in the dynamic load loops; $C_{m,\min}$ = peak dynamic pitching moment coefficient; $\Delta C_{m,\max} = C_{m,\max} - C_{m,\max,ss}$ = maximum pitching moment coefficient variation; $C_{m,\max,ss}$ = peak static pitching moment coefficient; M = moment stall angle; $C_{d,\text{man}}$ = maximum dynamic drag coefficient; $\Delta C_{d,\text{man}} = C_{d,\text{man}} - C_{d,\text{man,ss}}$ = maximum drag coefficient increment; $C_{d\text{man,ss}}$ = maximum static drag coefficient.
2) Static values: α_{ss} = static-stall angle = 13°; $C_{l\max,ss} = 0.92$; $C_{m,\min,ss} = -0.006$; L = M = 13°; $C_{d\text{man,ss}} = 0.0625$.
3) Superscript * indicates values obtained from MHFS measurements alone and subscript d indicates downstroke.

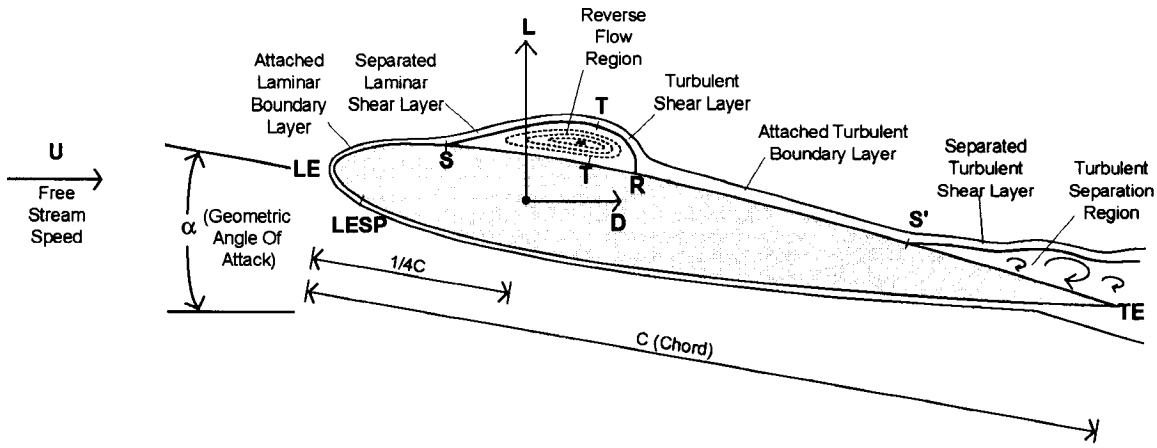

Figure 1 Conceptual sketch of the flow structure over a static NACA 0012 airfoil (valid for angles between 6 deg and the static-stall angle).

(a)

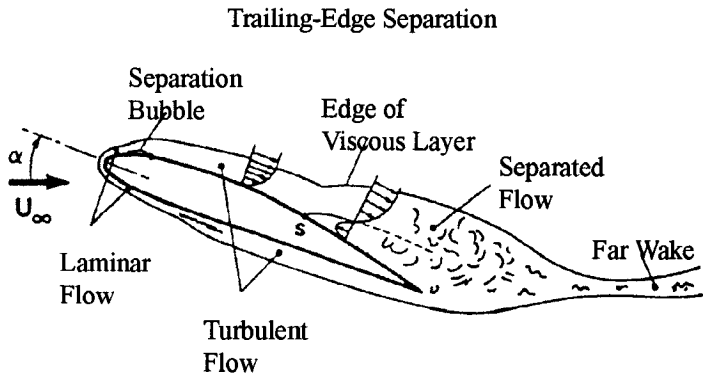

(b)

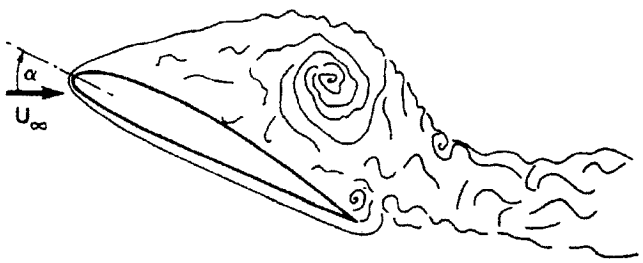

Figure 2 Conceptual sketches of flow fields during dynamic stall. (a) light stall and (b) deep stall (reproduced from [27]).

(a)

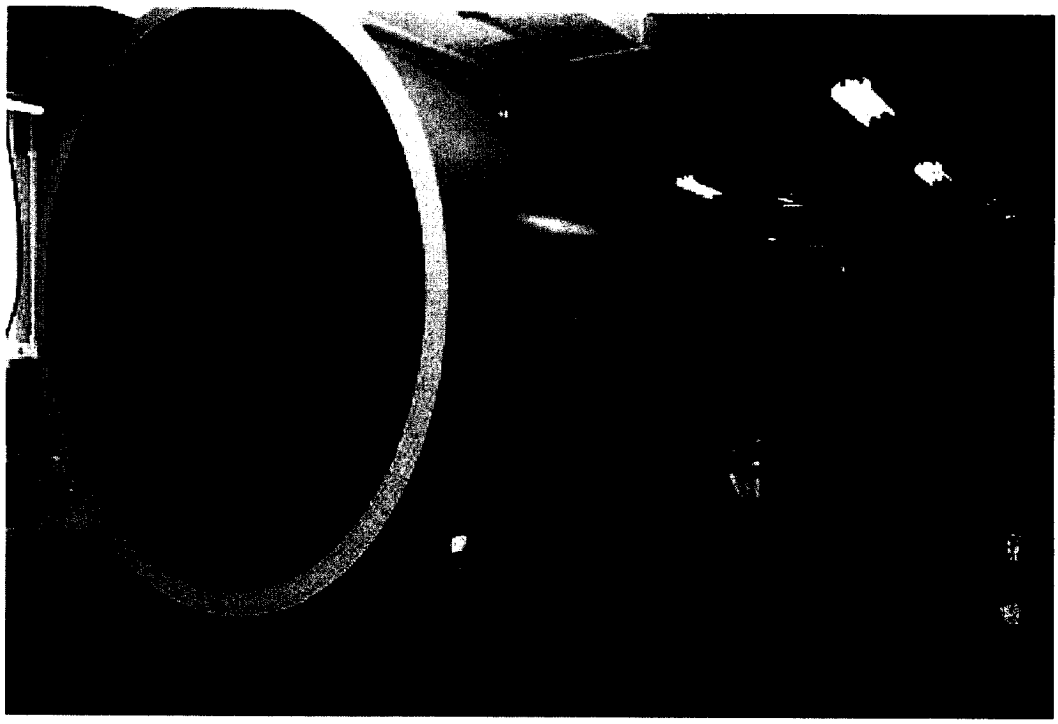

(b)

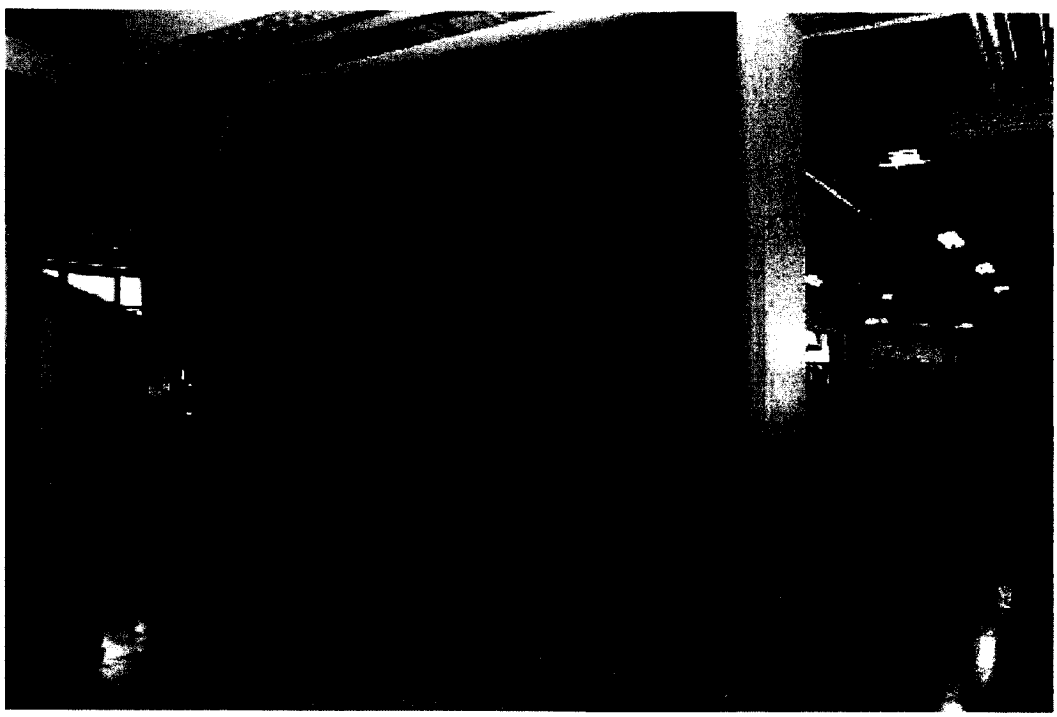

Figure 3 Photograph of the *Joseph Armand Bombardier* wind tunnel in the Aerodynamics Laboratory of the Department of Mechanical Engineering at McGill University. (a) Endview (diffuser with acoustic silencer), and (b) frontview (entrance). (c) Schematic diagram.

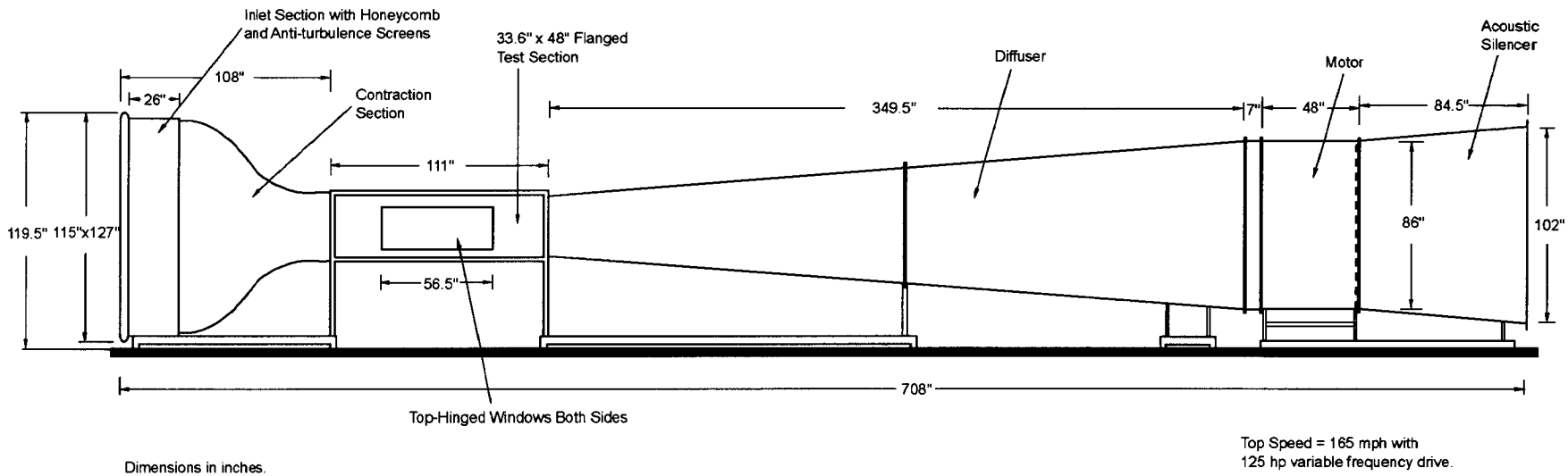

Figure 3 Photograph of the *Joseph Armand Bombardier* wind tunnel in the Aerodynamics Laboratory of the Department of Mechanical Engineering at McGill University. (a) Endview (diffuser with acoustic silencer), and (b) frontview (entrance). (c) Schematic diagram.

(a)

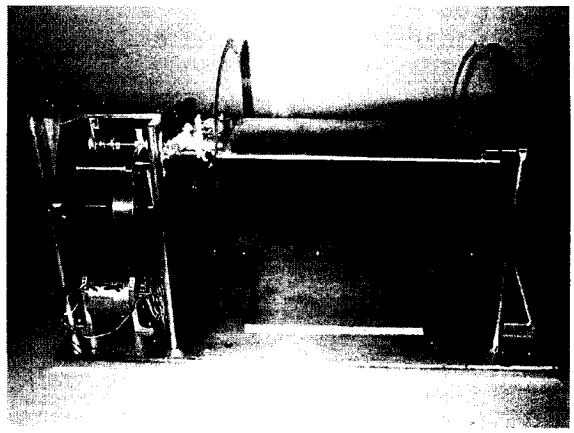

(b)

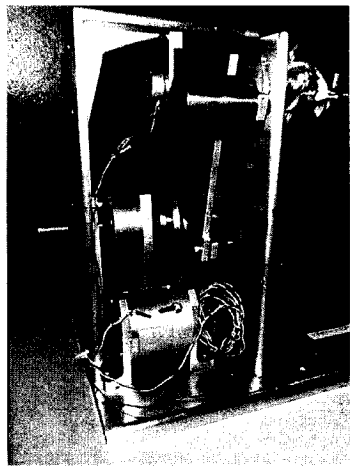

(c)

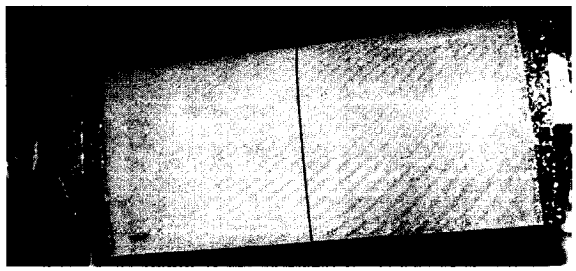

Figure 4 Photographs of (a) airfoil support, (b) oscillation mechanism and (c) NACA 0012 airfoil with MHFS array. Note that endplates are omitted for clarity.

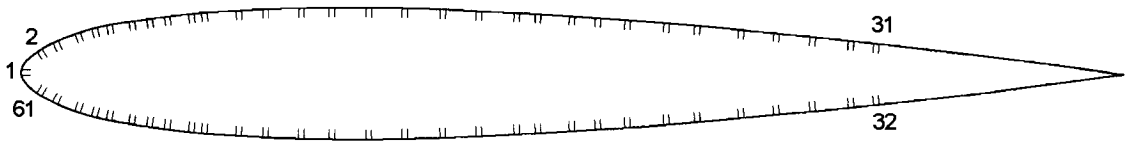

Location of Pressure Orifices:

	x/c		x/c		x/c
1	0.0000	11	0.1674	21	0.4741
2	0.0170	12	0.1988	22	0.5055
3	0.0314	13	0.2234	23	0.5293
4	0.0518	14	0.2566	24	0.5565
5	0.0671	15	0.2846	25	0.5922
6	0.0807	16	0.3186	26	0.6202
7	0.1011	17	0.3517	27	0.6602
8	0.1172	18	0.3866	28	0.6924
9	0.1334	19	0.4197	29	0.7256
10	0.1555	20	0.4545	30	0.7604
				31	0.7833

Figure 5 Schematic diagram of NACA 0012 airfoil model with pressure orifices. The pressure orifice locations are measured from the leading edge and the pressure orifices are symmetric about the chordline.

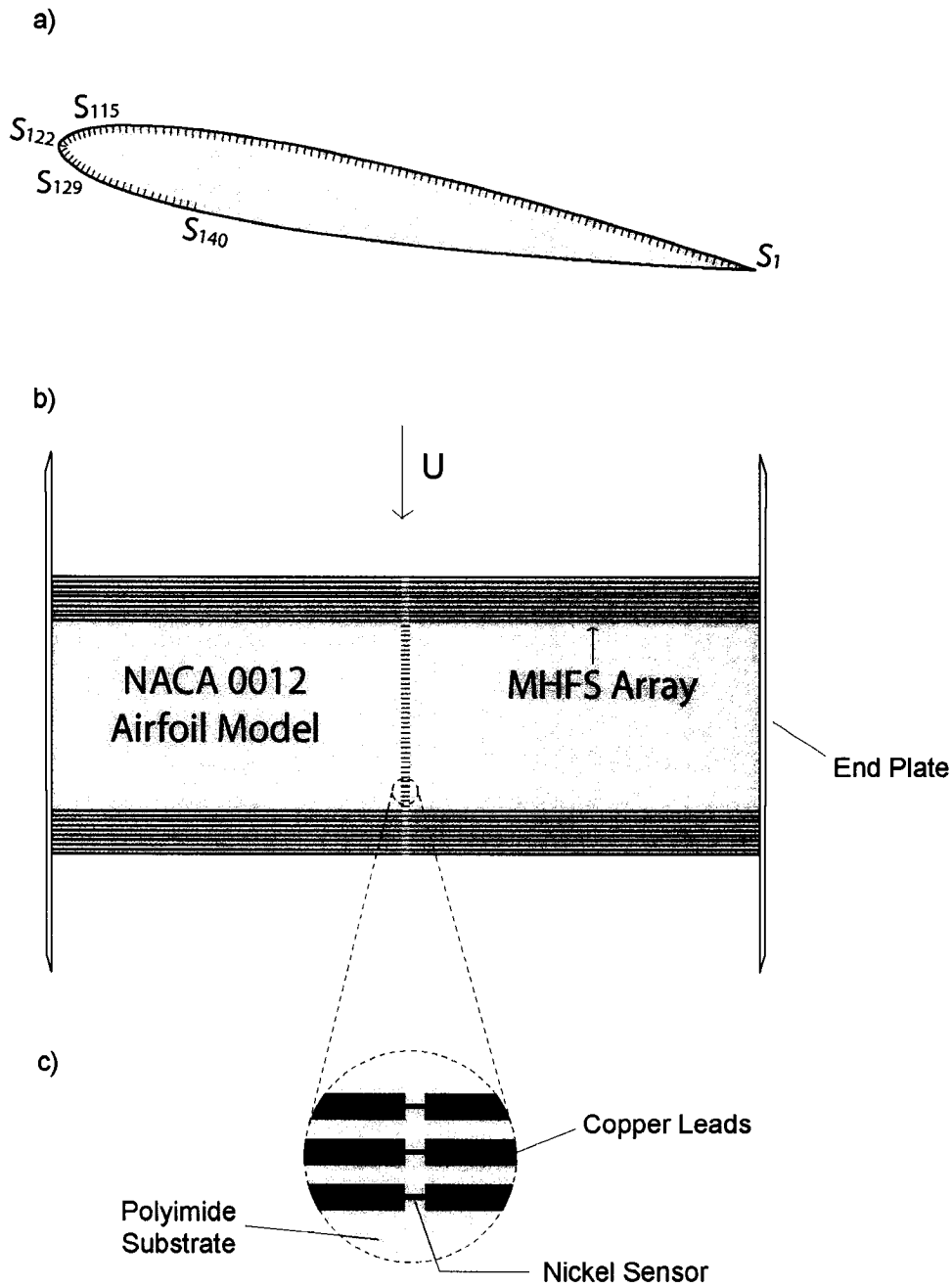

Figure 6 Schematic diagram of NACA 0012 airfoil model with MHFS array. (a) side view, (b) top view, and (c) exploded view of MHFS array.

(a)

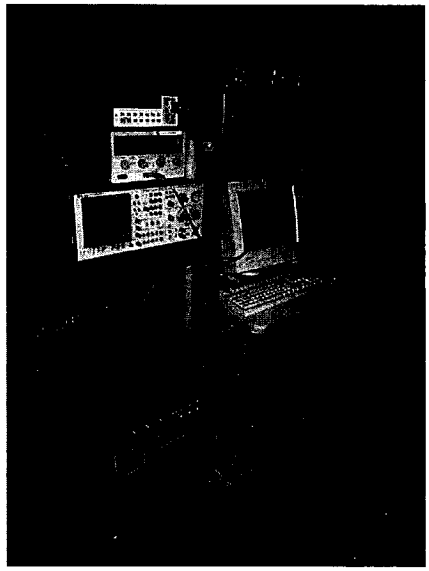

(b)

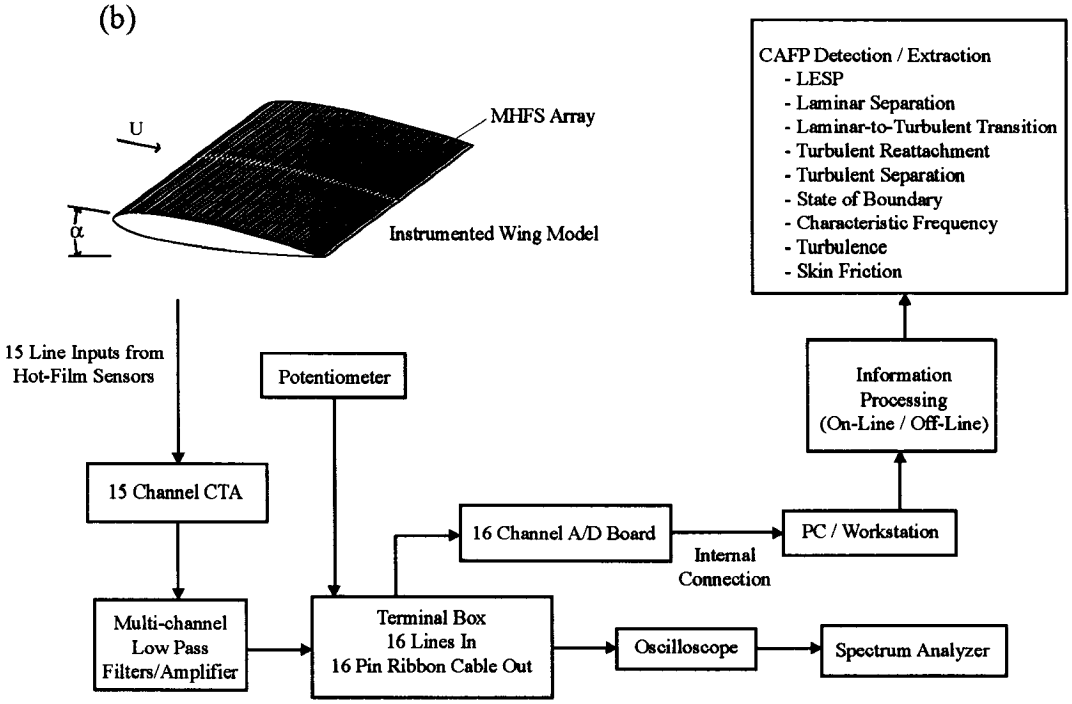

Figure 7 Experimental setup and instrumentation system. (a) Photograph and schematic of (b) MHFS, (c) surface pressure, and (d) hot-wire wake velocity measurments.

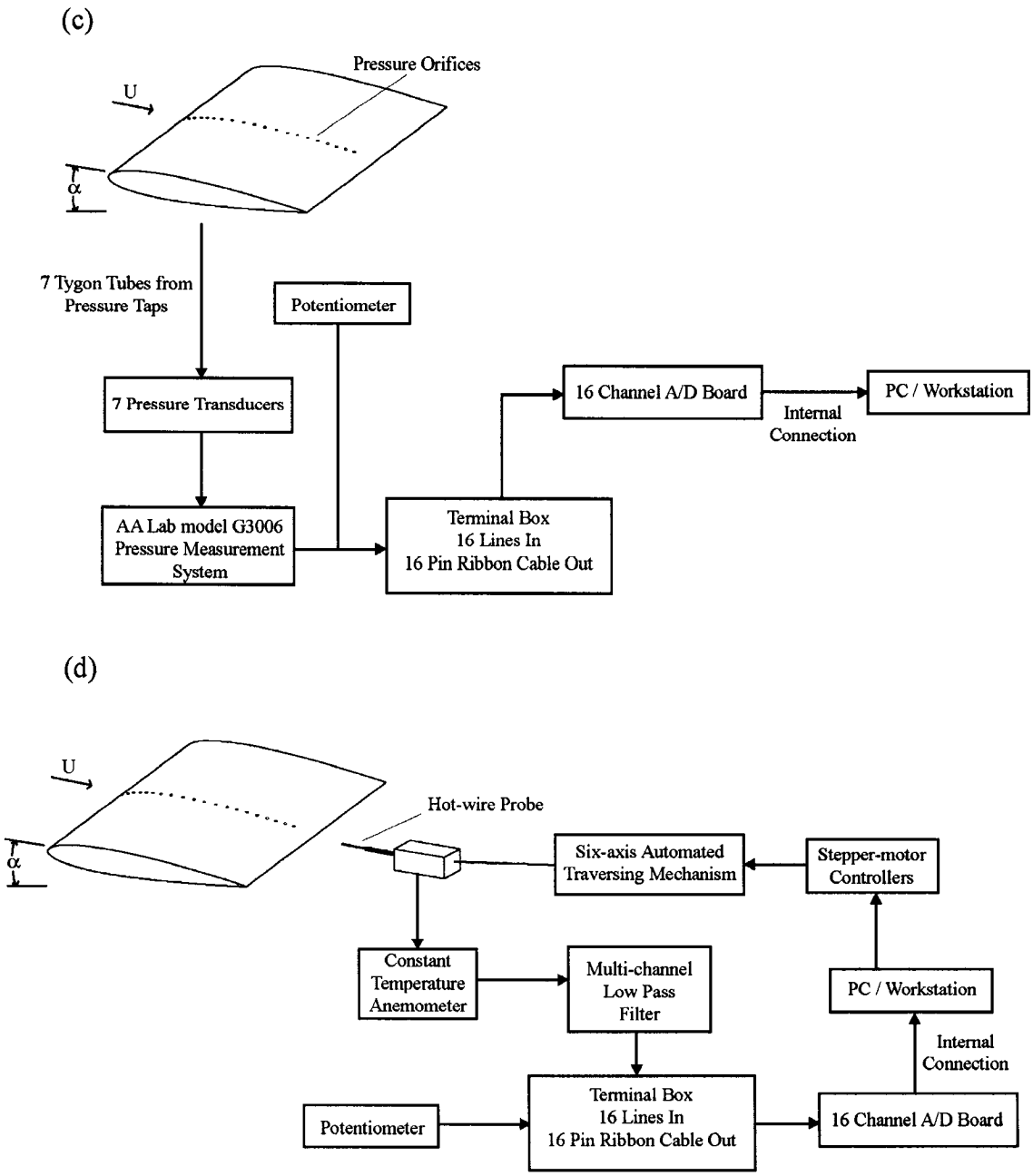

Figure 7 (Continued) Experimental setup and instrumentation system. (a) Photograph and schematic of (b) MHFS, (c) surface pressure, and (d) hot-wire wake velocity measurments.

Figure 8 Photograph of six-axis computer controlled traversing mechanism in the test section of the wind tunnel.

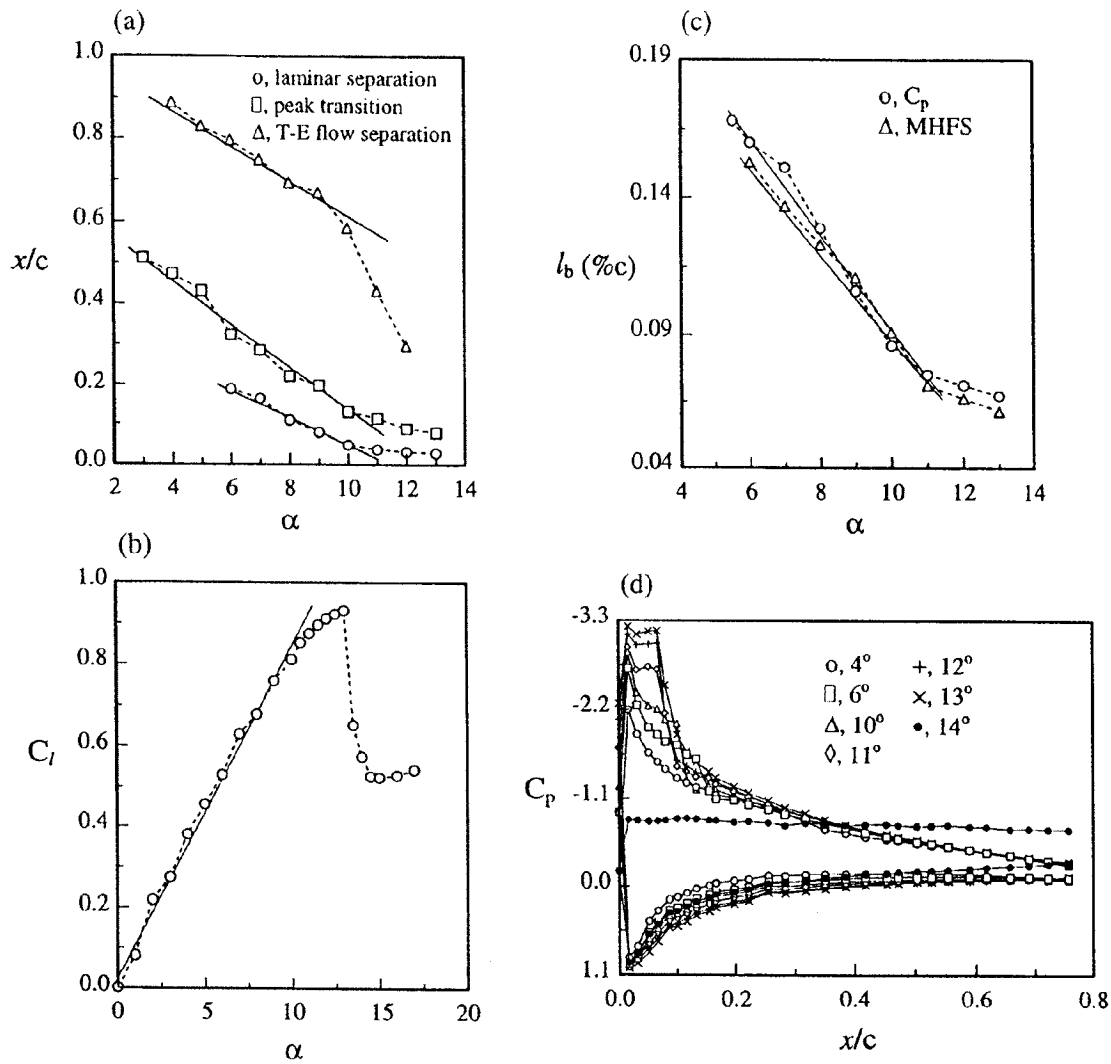

Figure 9 Boundary-layer events of a static NACA 0012 airfoil at Re = 1.35 x 10^5. (a) critical flow points, (b) C_l - α curve, (c) bubble length l_b, and (d) C_p distributions.

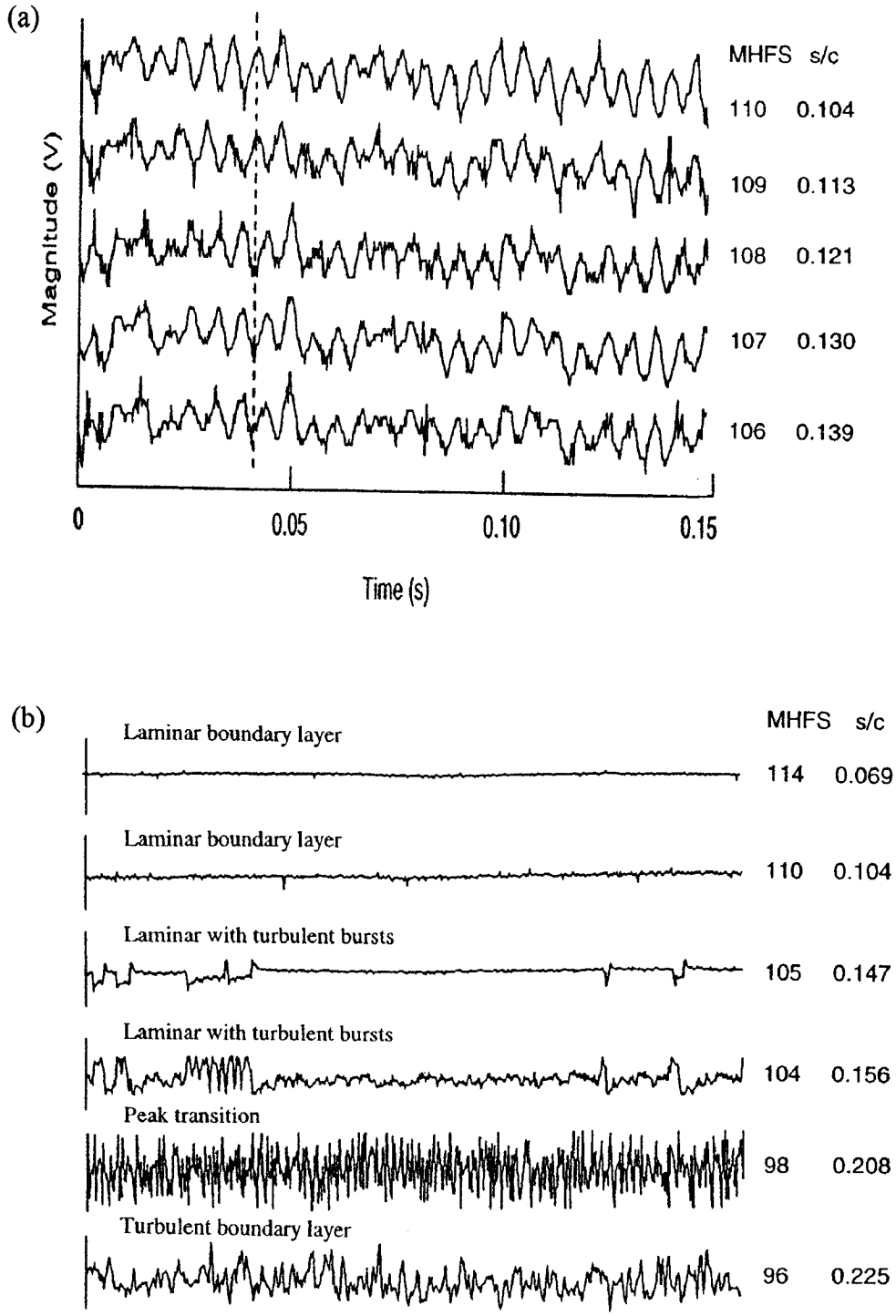

Figure 10 Identification of (a) laminar separation and (b) boundary-layer transition over a static NACA 0012 from MHFS signals.

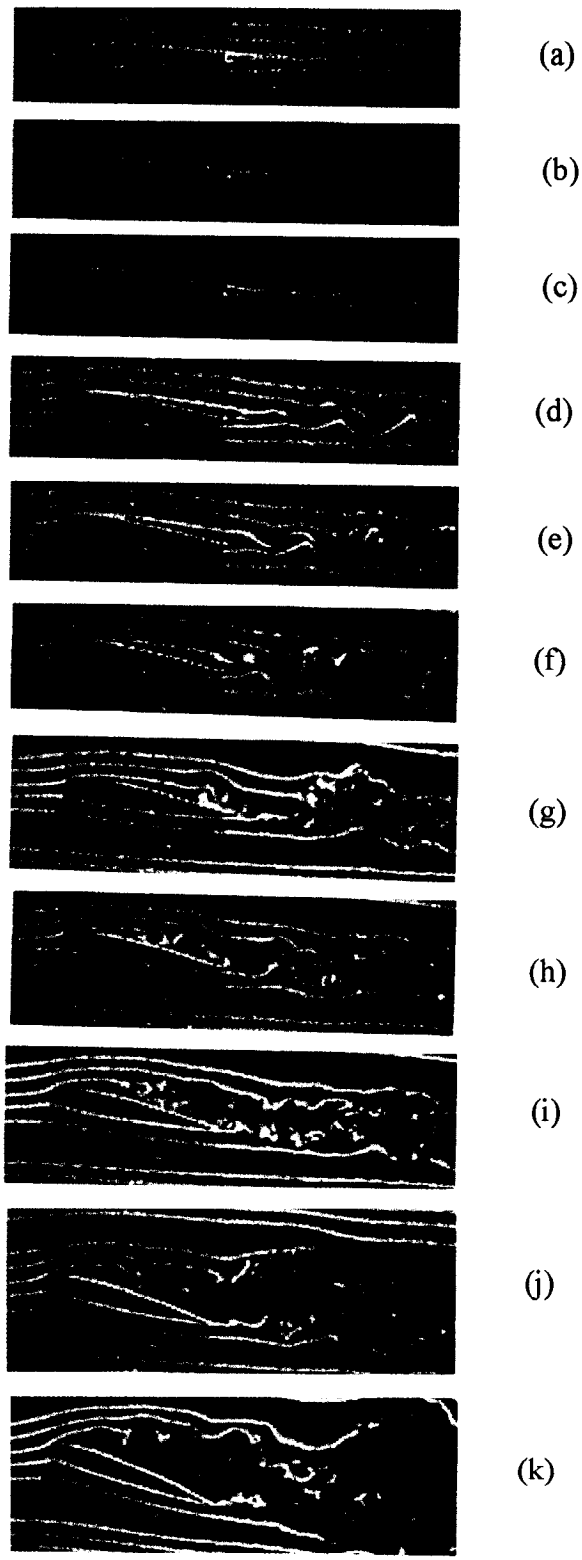

Figure 11 Smoke flow visualization pictures for a static NACA 0012 airfoil at angles of attack (a) 2 deg, (b) 4 deg, (c) 5 deg, (d) 6 deg, (e) 7 deg, (f) 8 deg, (g) 9 deg, (h) 10 deg, (i) 12 deg, (j) 15 deg and (k) 20 deg. The flow is from left to right.

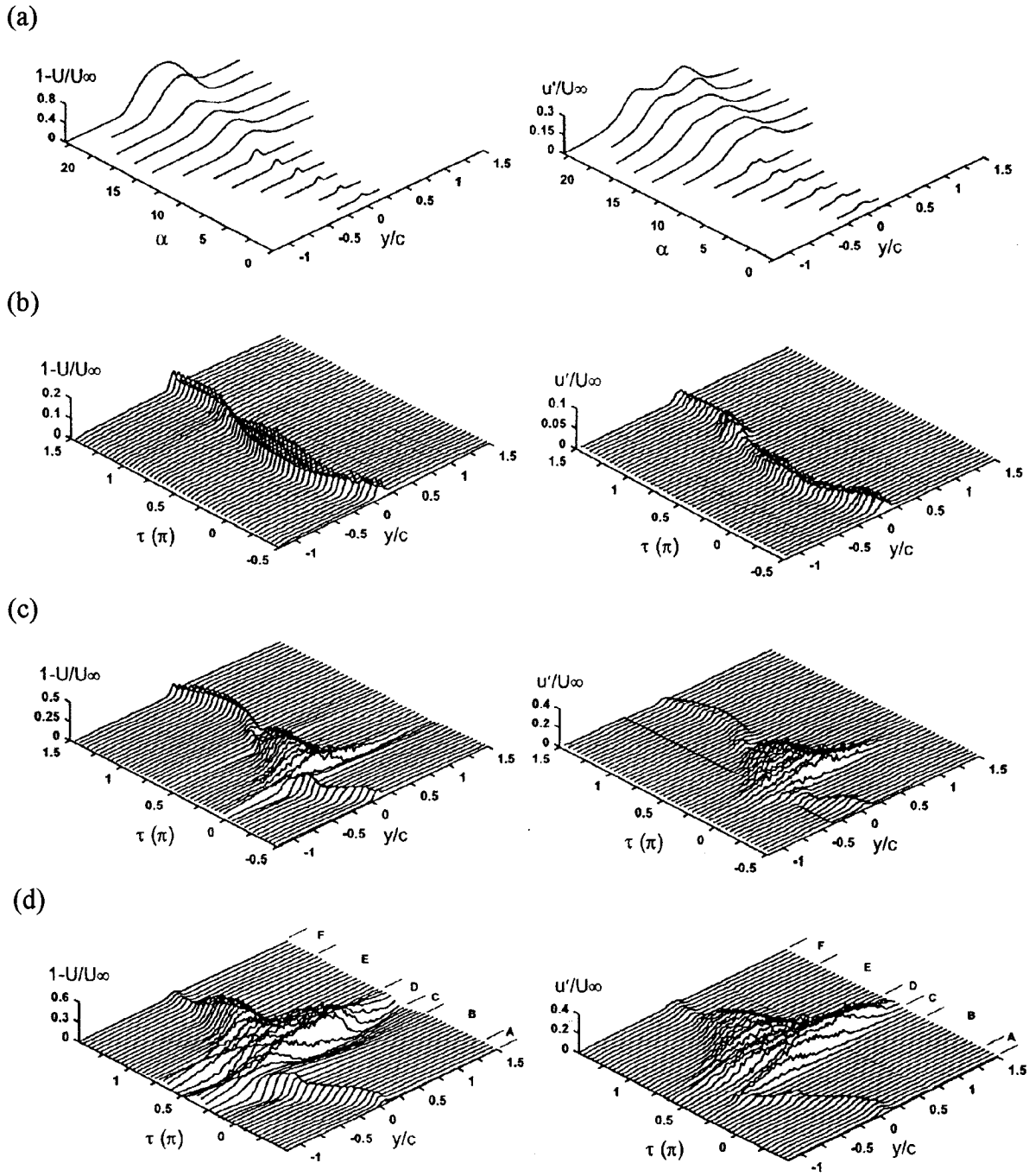

Figure 12 Typical 3-D representation of the wake mean and fluctuating velocity profiles. (a) static airfoil, (b) $\alpha(t) = 0° + 7.5° \sin\omega t$ and $\kappa = 0.05$, (c) $\alpha(t) = 0° + 15° \sin\omega t$ and $\kappa = 0.05$, and (d) $\alpha(t) = 10° + 15° \sin\omega t$ and $\kappa = 0.10$. (e) 2-D presentation of (d) at selected $\alpha(t)$ corresponding to Regions A-F with o, $\kappa = 0.05$; □, $\kappa = 0.10$; Δ, $\kappa = 0.20$ and; ____, static airfoil.

(e)

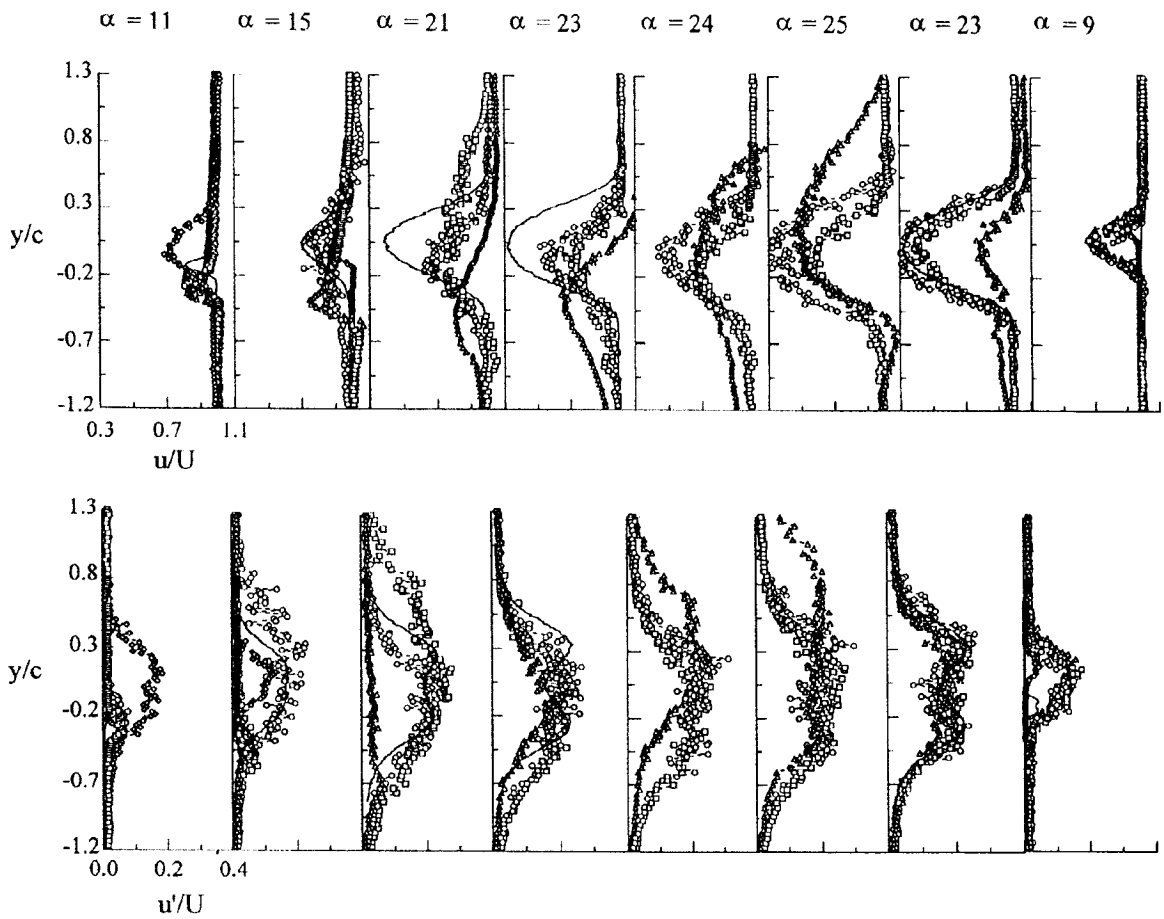

Figure 12 (Continued) Typical 3-D representation of the wake mean and fluctuating velocity profiles. (a) static airfoil, (b) $\alpha(t) = 0° + 7.5° \sin\omega t$ and $\kappa = 0.05$, (c) $\alpha(t) = 0° + 15° \sin\omega t$ and $\kappa = 0.05$, and (d) $\alpha(t) = 10° + 15° \sin\omega t$ and $\kappa = 0.10$. (e) 2-D presentation of (d) at selected $\alpha(t)$ corresponding to Regions A-F with o, $\kappa = 0.05$; □, $\kappa = 0.10$; Δ, $\kappa = 0.20$ and; ____, static airfoil.

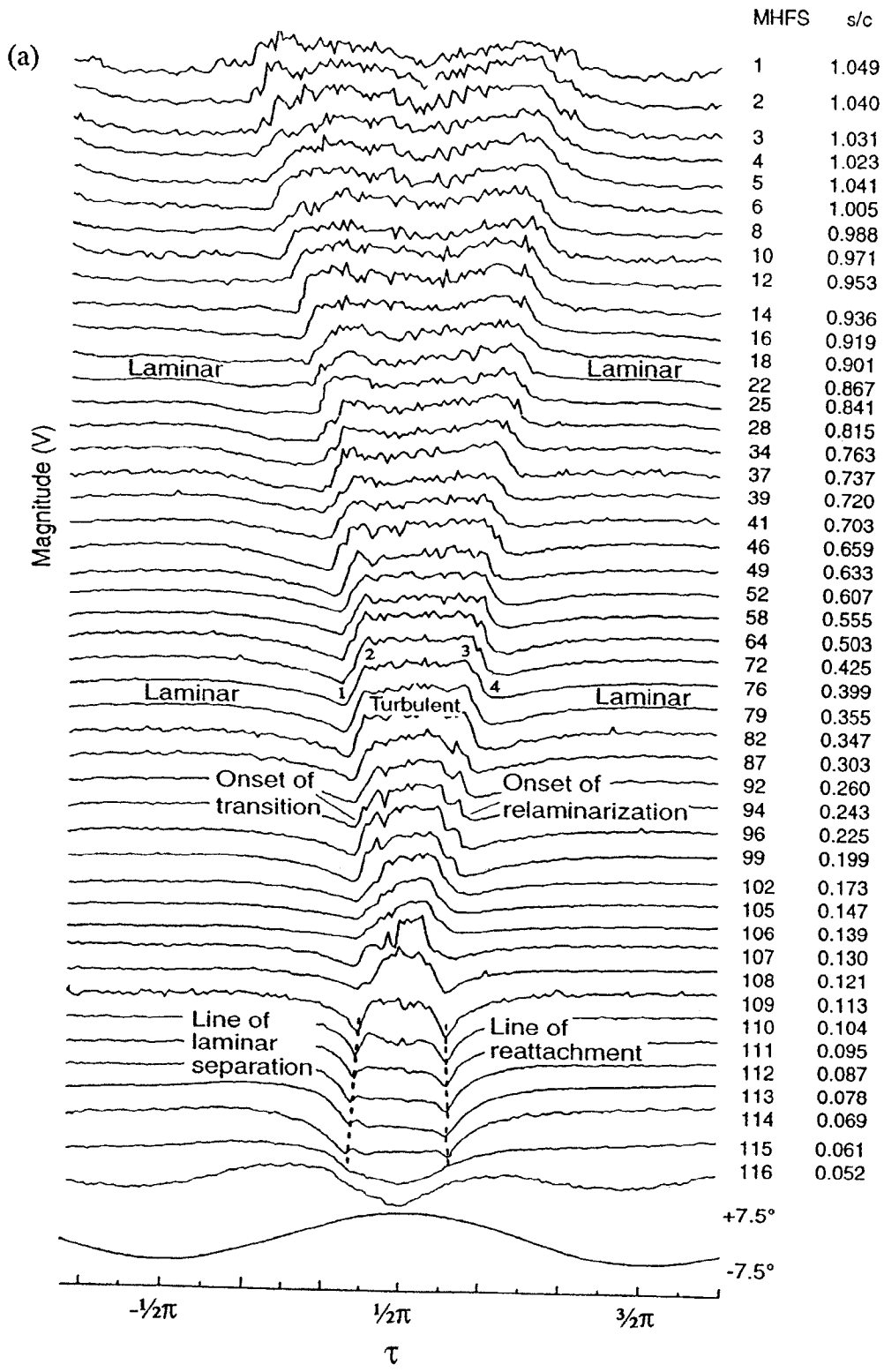

Figure 13 Representative MHFS signals for $\alpha(t) = 0° + 7.5° \sin\omega t$ at $\kappa = 0.05$. (a) S_1-S_{116} and (b) S_{114}-S_{126}. T_1 through T_{17} denote the locus of the leading-edge stagnation point (LESP). For sensor S_{76}, point 1 identifies transition, the region between points 2 and 3 indicates an attached turbulent boundary layer and point 4 denotes the return to a laminar boundary layer.

(b)

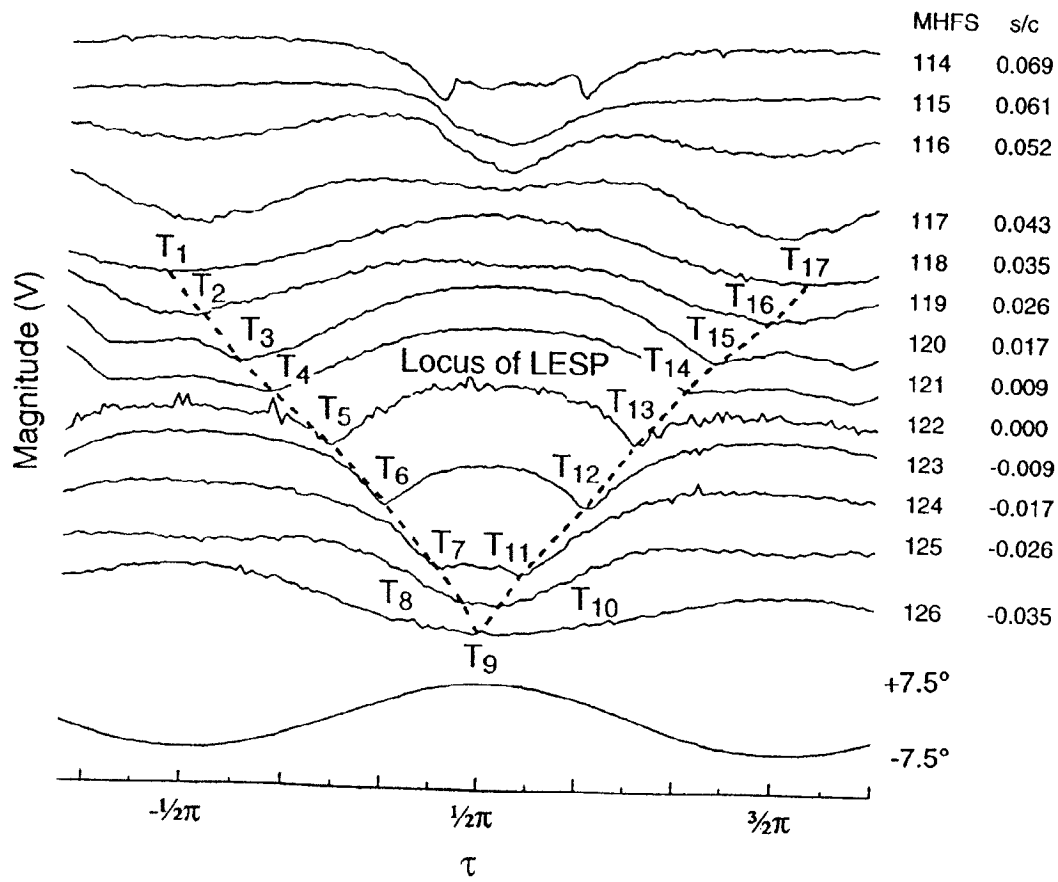

Figure 13 (Continued) Representative MHFS signals for $\alpha(t) = 0° + 7.5°\ \sin\omega t$ at $\kappa = 0.05$. (a) S_1-S_{116} and (b) S_{114}-S_{126}. T_1 through T_{17} denote the locus of the leading-edge stagnation point (LESP). For sensor S_{76}, point 1 identifies transition, the region between points 2 and 3 indicates an attached turbulent boundary layer and point 4 denotes the return to a laminar boundary layer.

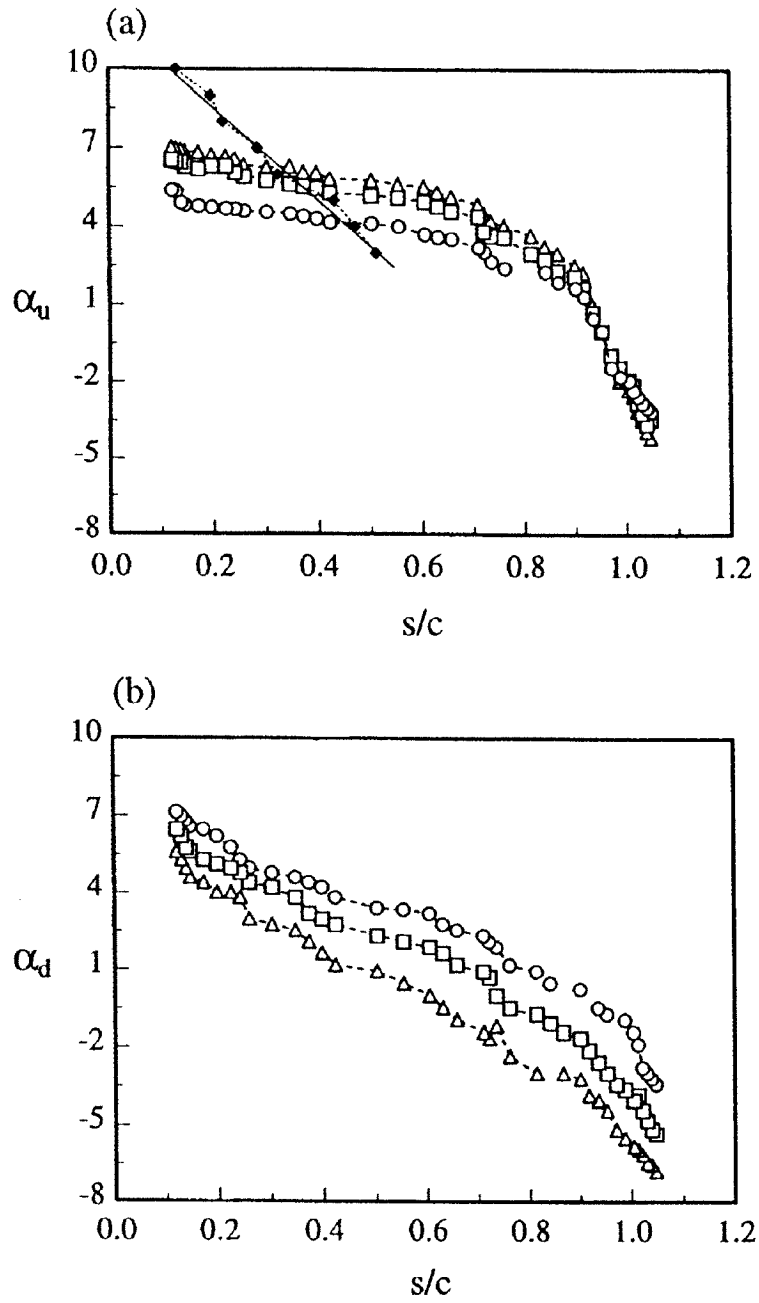

Figure 14 Loci of boundary layer (a) transition and (b) relaminarization for $\alpha(t) = 0° + 7.5° \sin\omega t$: o, $\kappa = 0.025$; □, $\kappa = 0.05$; Δ, $\kappa = 0.1$; and ♦, static airfoil.

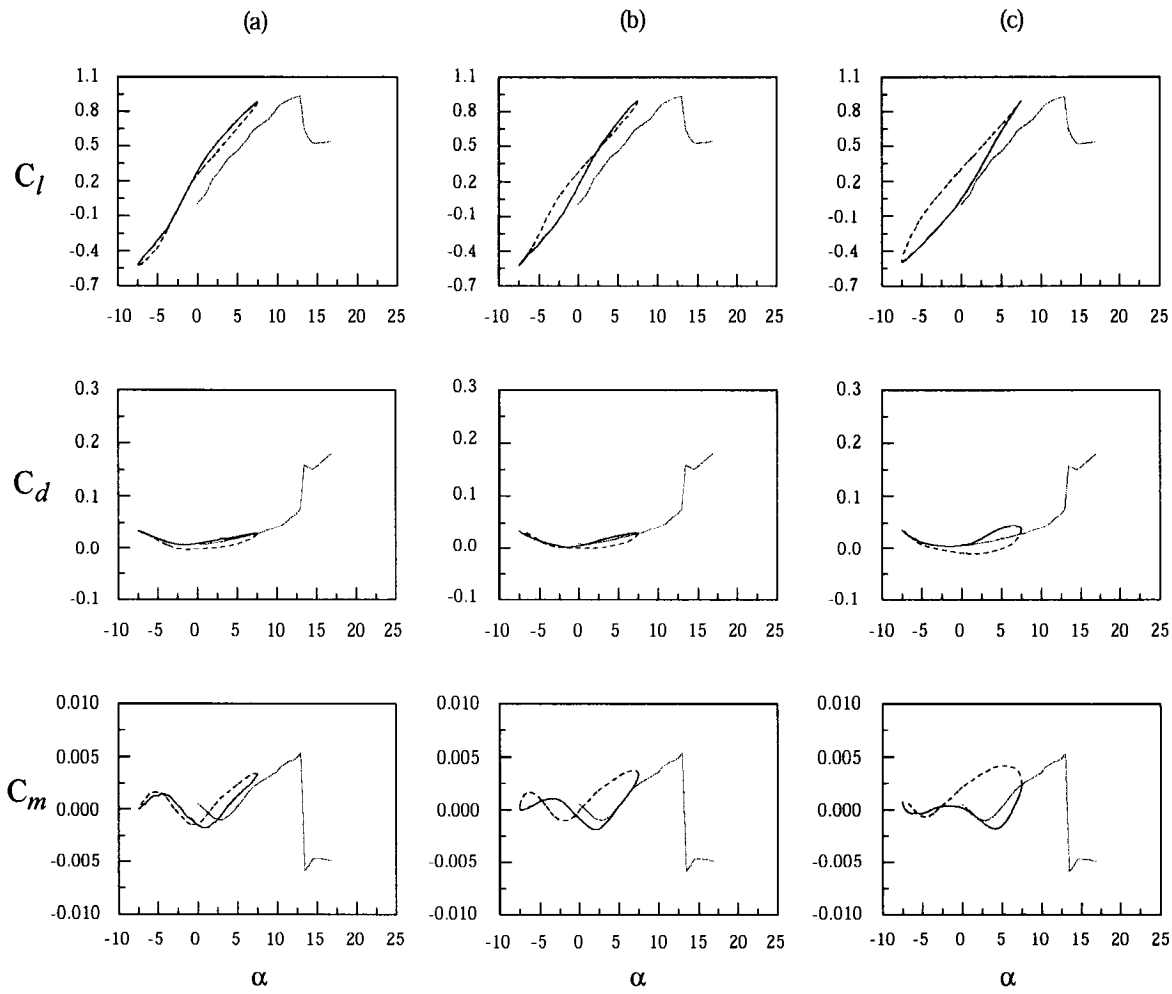

Figure 15 Dynamic loads loops for $\alpha(t) = 0° + 7.5° \sin\omega t$. (a) $\kappa = 0.025$, (b) $\kappa = 0.05$, and (c) $\kappa = 0.1$. ____, increasing α; – – –, decreasing α; ....., static values.

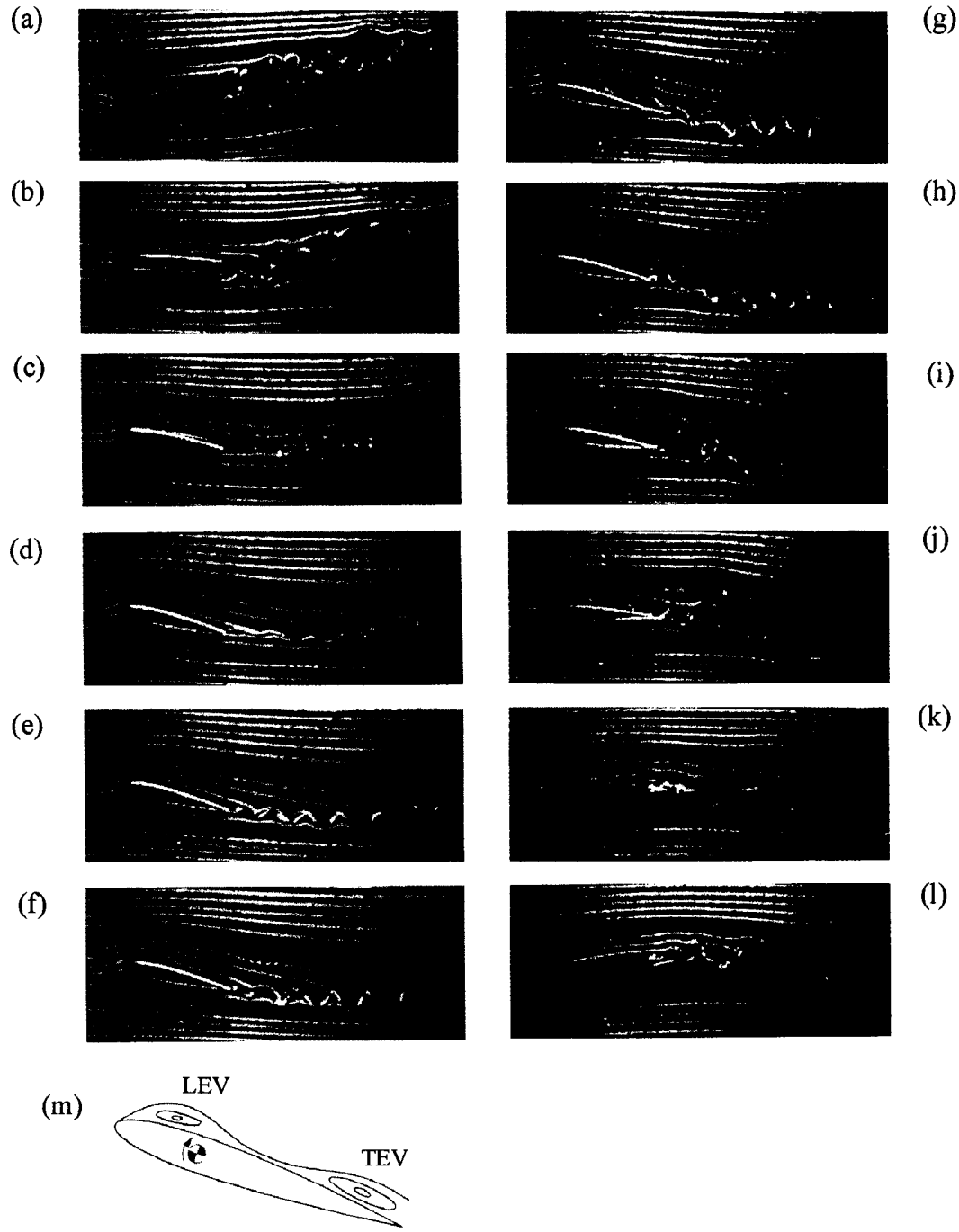

Figure 16 Selected smoke flow visualization pictures for an oscillating airfoil at $\alpha(t) = 0° + 15° \sin\omega t$ and $\kappa = 0.05$. (a) $\alpha_u = -14.44$ deg, (b) $\alpha_u = 0$ deg, (c) $\alpha_u = 9.8$ deg, (d) $\alpha_u = 13.6$ deg, (e) $\alpha_u = 13.7$ deg, (f) $\alpha_u = 14.38$ deg, (g) $\alpha_d = 14.64$ deg, (h) $\alpha_d = 14.2$ deg, (i) $\alpha_d = 9.78$ deg, (j) $\alpha_d = 3.33$ deg, (k) $\alpha_d = -2.31$ deg, (l) $\alpha_d = -8.31$ deg and (m) a conceptual sketch of (f). Flow is from left to right. Subscripts u and d denote upstroke and downstroke, respectively.

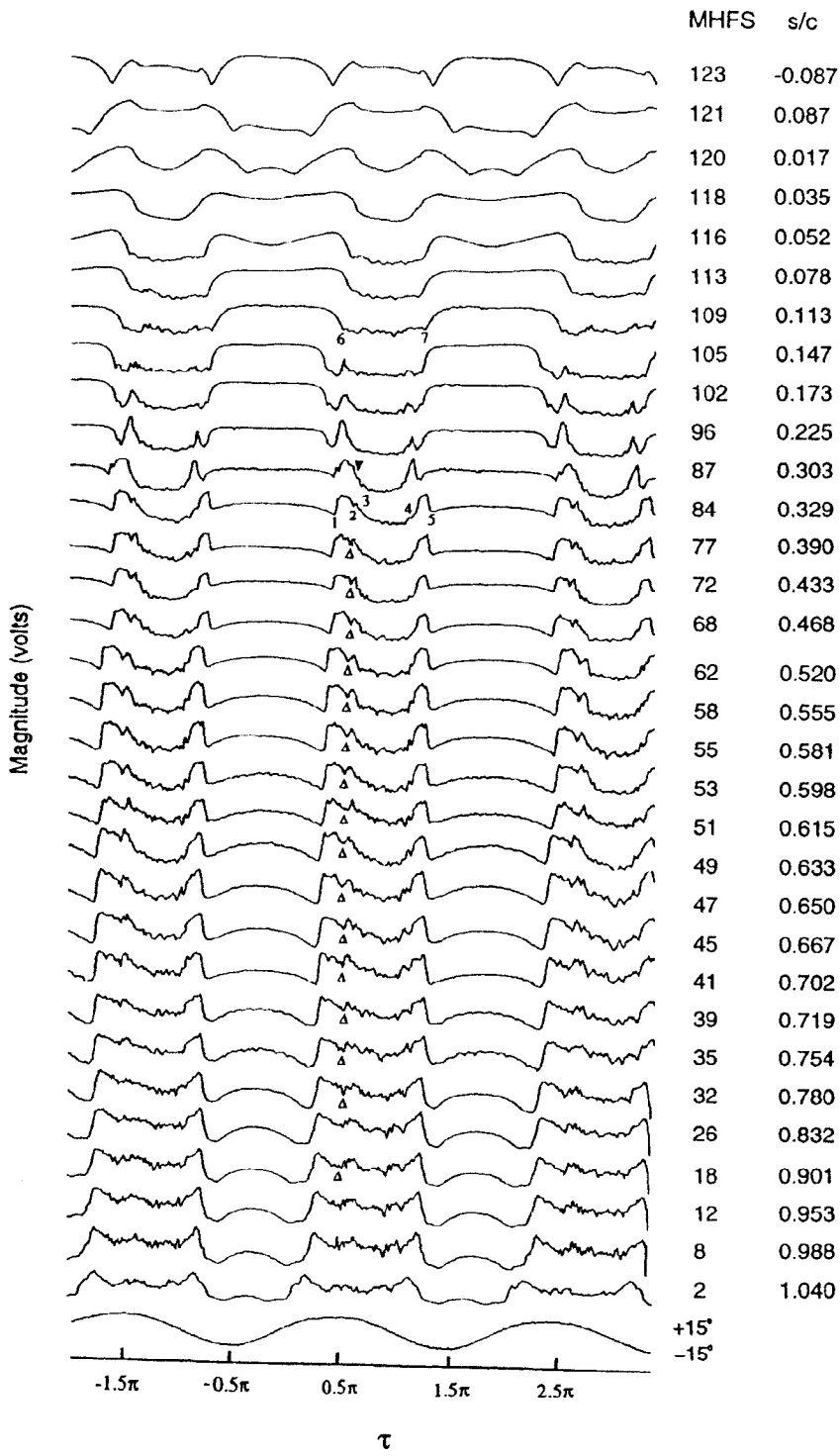

Figure 17 Composite plot of representative MHFS signals for $\alpha(t) = 0° + 15° \sin\omega t$ at $\kappa = 0.05$. Point 1 identifies transition, 1-2 attached turbulent boundary layer, 3-4 separated turbulent boundary layer, 4 onset of turbulent boundary layer reattachment, 5 end of relaminarization, 6 laminar separation and 7 laminar reattachment. Δ, flow reversal and ▼, turbulent separation.

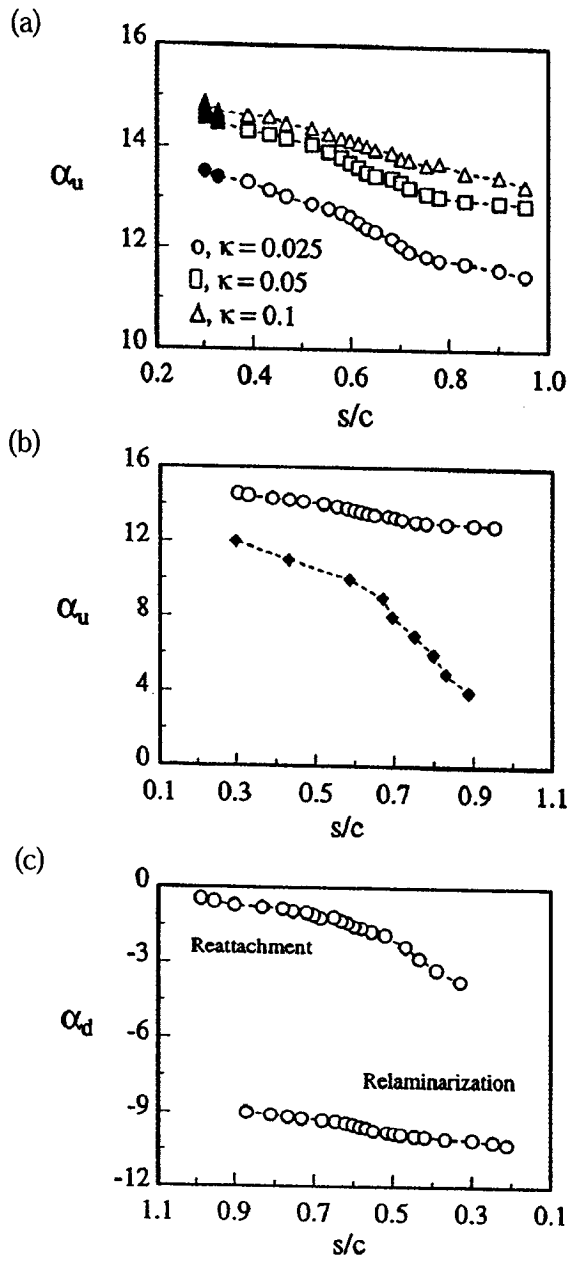

Figure 18 Boundary layer events for $\alpha(t) = 0° + 15° \sin\omega t$ at $\kappa = 0.05$: (a) flow reversal (open symbols) and turbulent separation (solid symbols), (b) transition, and (c) reattachment and relaminarization.

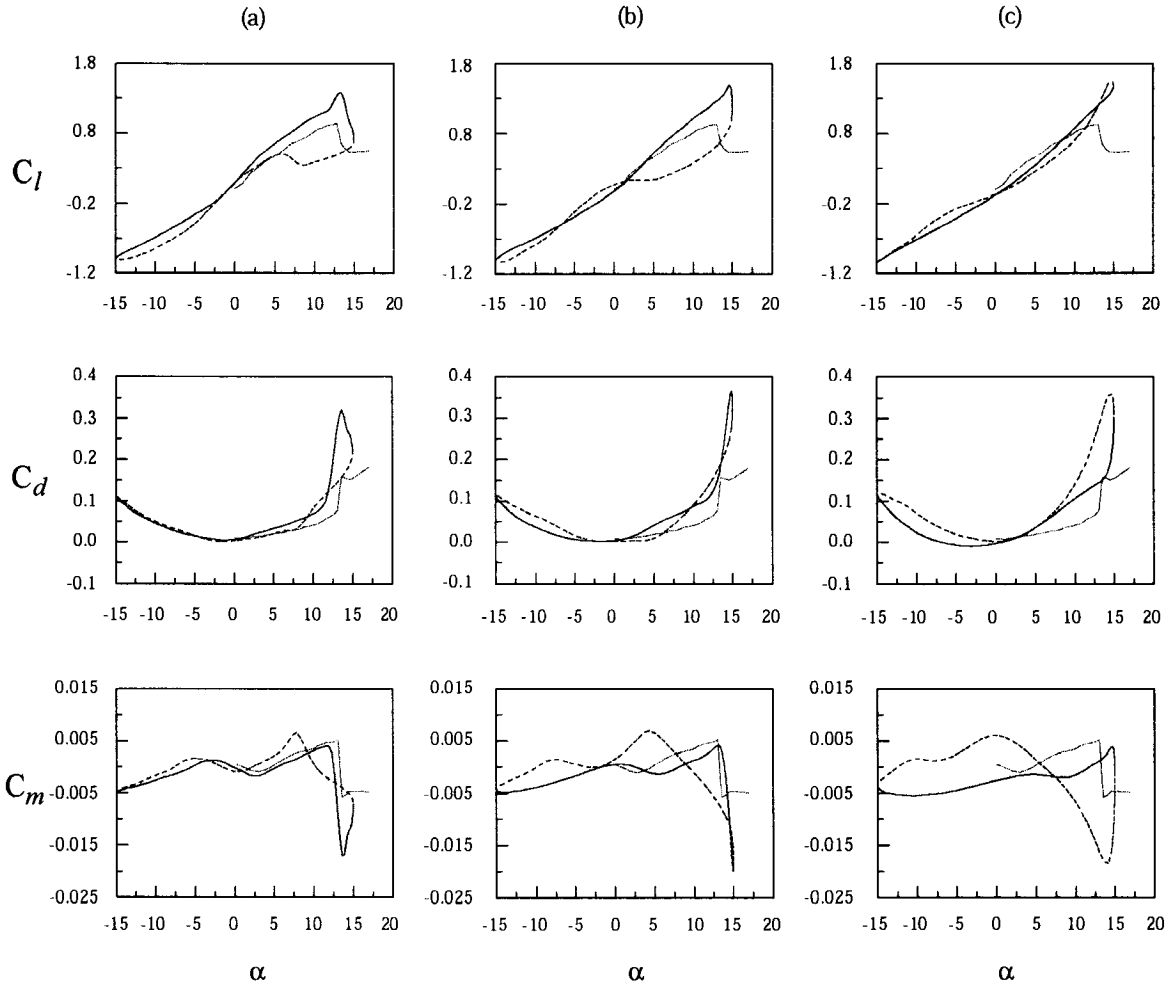

Figure 19 Dynamic loads loops for $\alpha(t) = 0° + 15° \sin\omega t$. (a) $\kappa = 0.025$, (b) $\kappa = 0.05$, and (c) $\kappa = 0.1$. ____, increasing α; – – –, decreasing α; ....., static values.

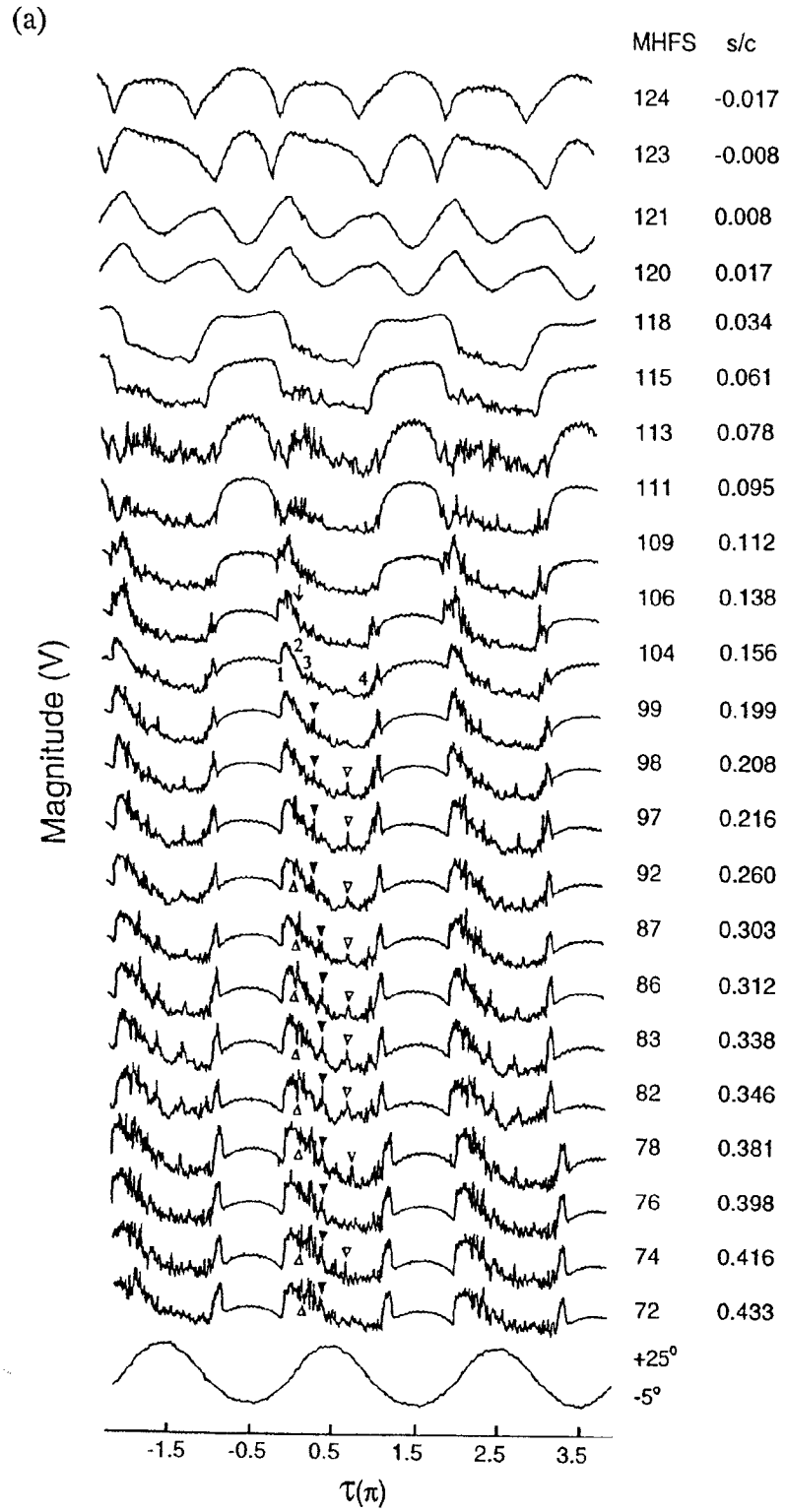

Figure 20 Representative MHFS signals for $\alpha(t) = 10° + 15° \sin\omega t$ at $\kappa = 0.1$. (a) S_{124}-S_{72} and (b) S_{63}-S_2. Δ, flow reversal; ↓, turbulent separation; ▼, passage of LEV; and ▽, passage of secondary vortex. Point 1 denotes transition, points 2-3 turbulent breakdown and 3-4 separated flow.

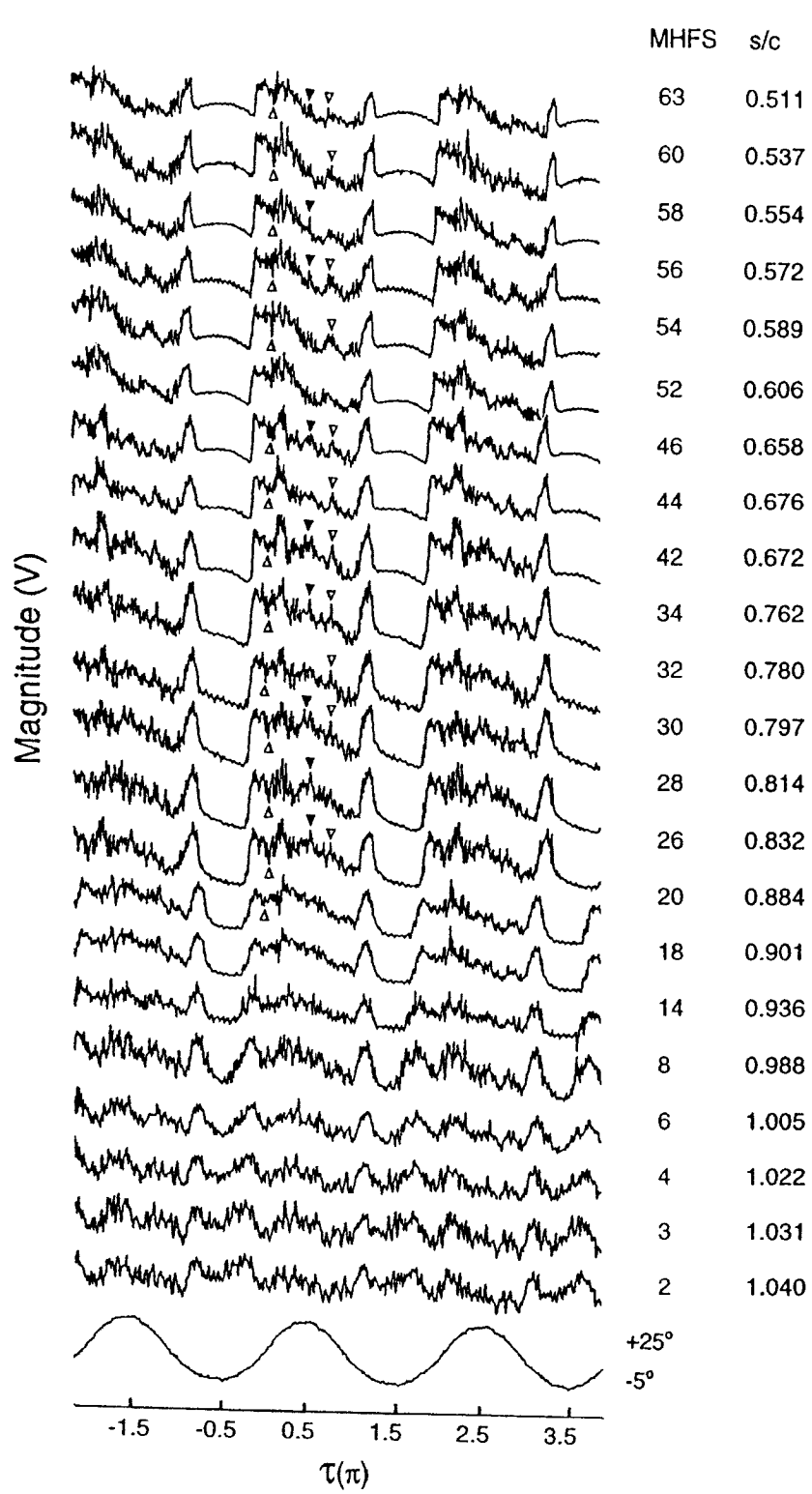

Figure 20 (Continued) Representative MHFS signals for $\alpha(t) = 10° + 15° \sin\omega t$ at $\kappa = 0.1$. (a) S_{124}-S_{72} and (b) S_{63}-S_2. Δ, flow reversal; ↓, turbulent separation; ▼, passage of LEV; and ▽, passage of secondary vortex. Point 1 denotes transition, points 2-3 turbulent breakdown and 3-4 separated flow.

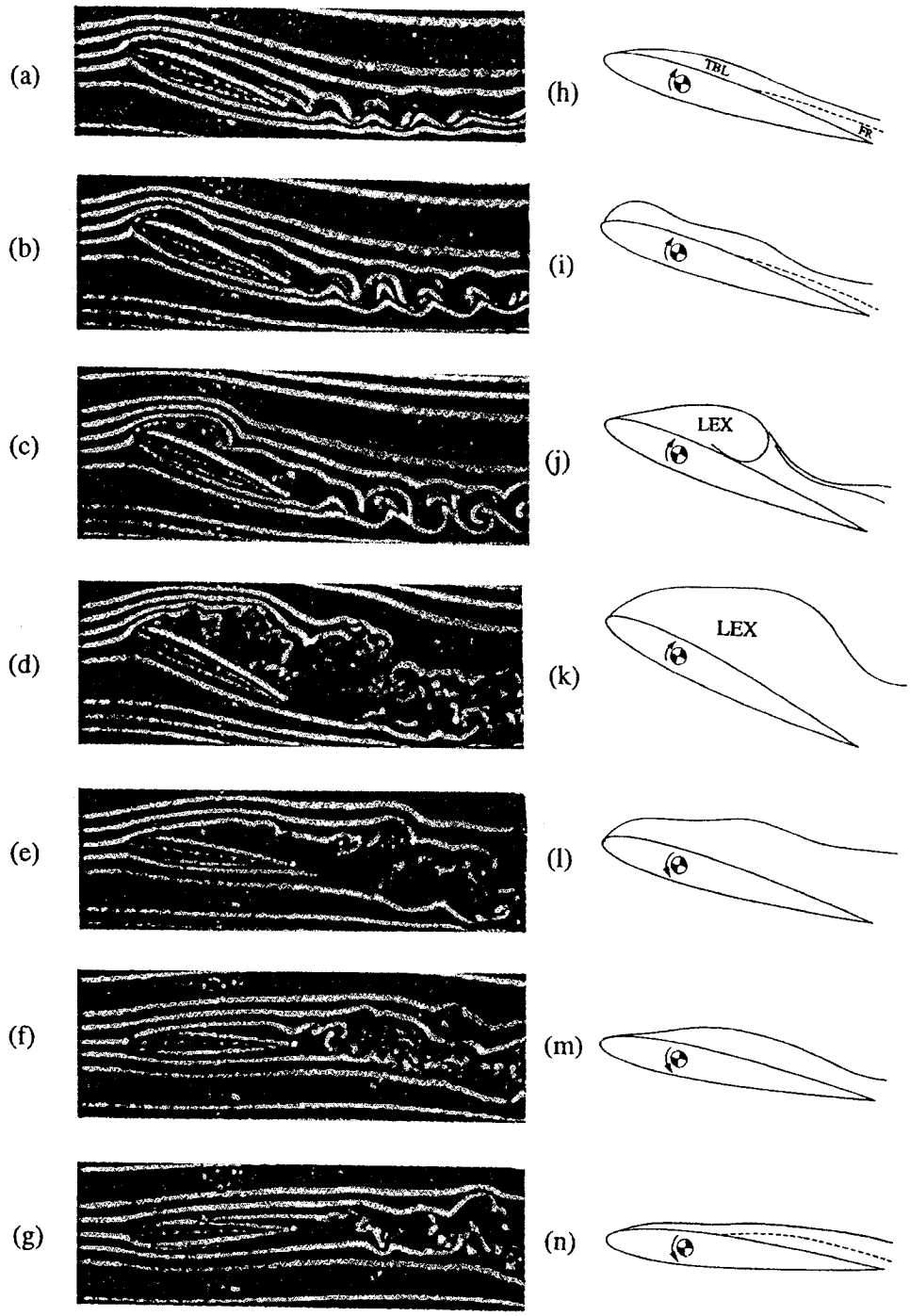

Figure 21 Selected sequences of boundary-layer events both prior to, during, and post stall at $\kappa = 0.1$ for $\alpha(t) = 10° + 15° \sin\omega t$. (a) upward spread of flow reversal for 12.9 deg $< \alpha_u <$ 21.6 deg; (b) turbulent breakdown and the formation of a LEV at $\alpha_u = 21.9$ deg; (c) LEV growth and rearward convection for $\alpha_u = 22.4$ deg - 24.4 deg; (d) LEV catastrophic detachment at $\alpha_u = 24.7$ deg; (e) separated flow for $\alpha_d > 14.1$ deg; (f) and (g) rearward reattachment for $\alpha_d < 14.1$ deg; (h) - (n) are the conceptual sketches of (a) - (g), respectively.

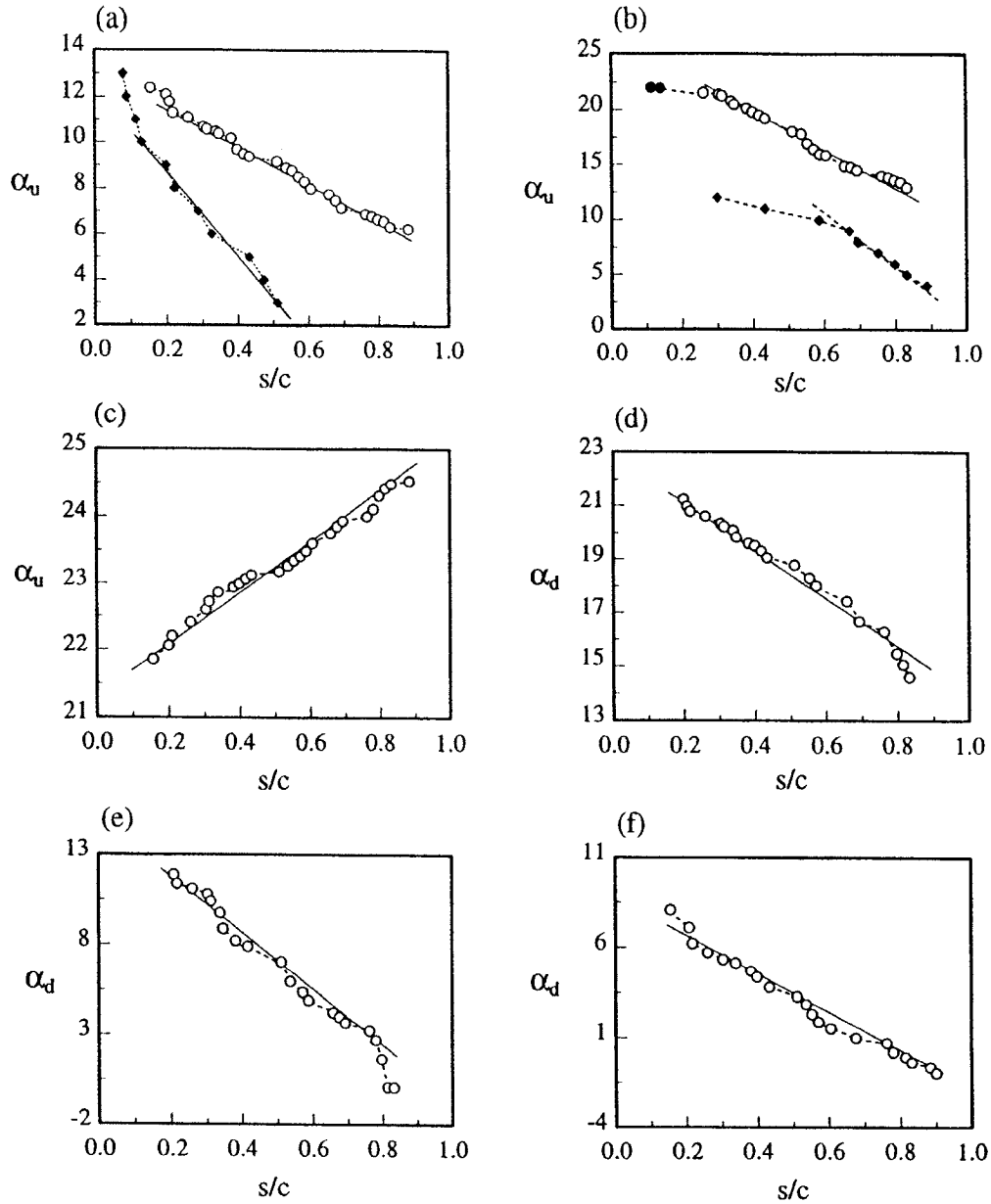

Figure 22 Loci of boundary-layer (a) transition, (b) flow reversal (o) and turbulent breakdown (•), (c) LEV, (d) secondary vortex, (e) reattachment, and (f) relaminarization at $\kappa = 0.1$ for $\alpha(t) = 10° + 15° \sin\omega t$. Note that only the clearly identifiable critical flow points were plotted. ◆, static airfoil.

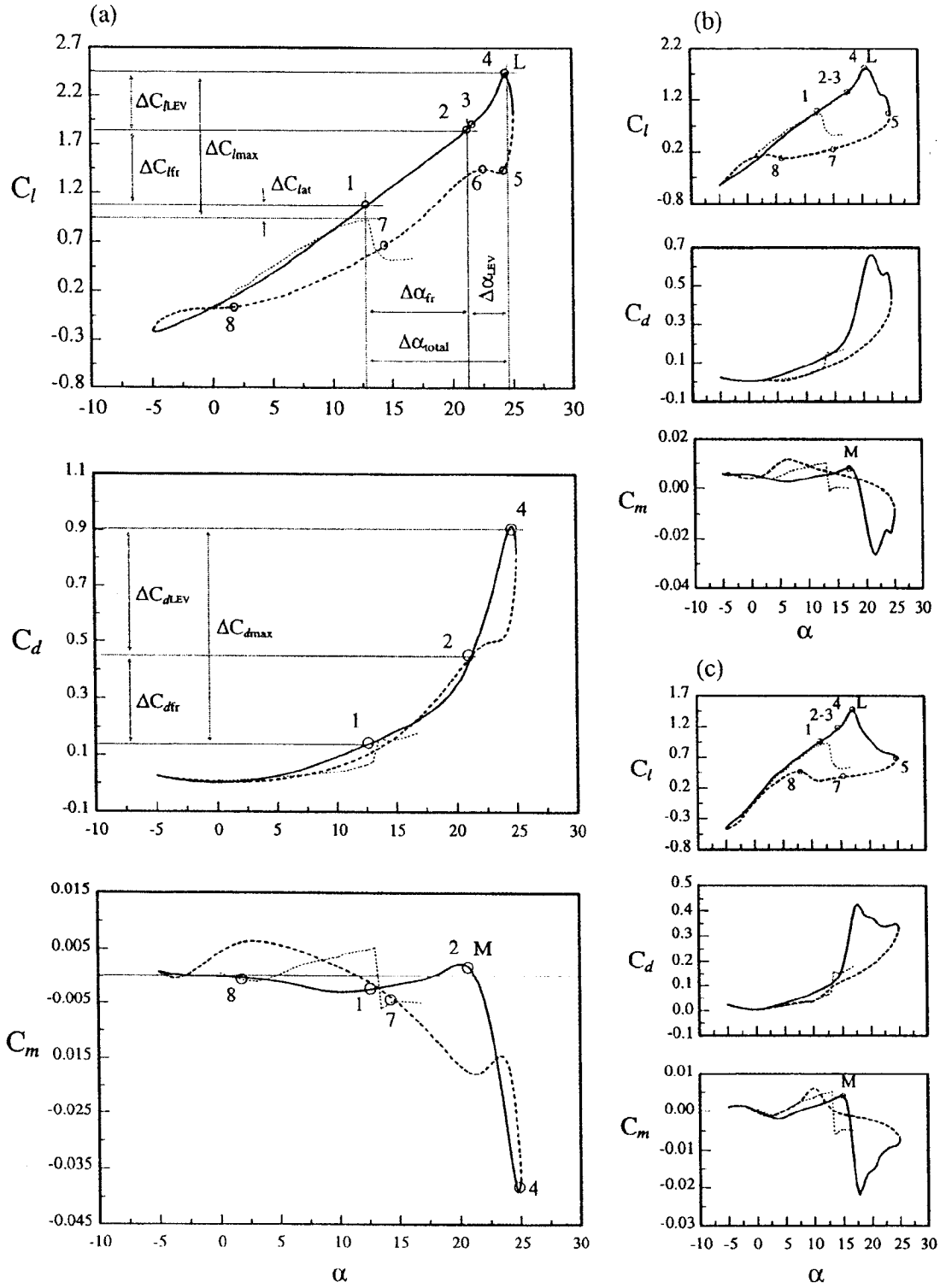

Figure 23 Variation of dynamic loads with reduced frequency for $\alpha(t) = 10° + 15° \sin\omega t$. (a) $\kappa = 0.1$, (b) $\kappa = 0.05$, and (c) $\kappa = 0.025$. 1, onset of flow reversal; 2, end of upward spread of flow reversal; 3, turbulent breakdown; 4, lift stall; 4-5, full stall; 6, onset of secondary vortex; 7, onset of flow reattachment; and 8, end of flow reattachment. ____, increasing α; – – –, decreasing α; ....., static values; M, moment stall; and L, lift stall.

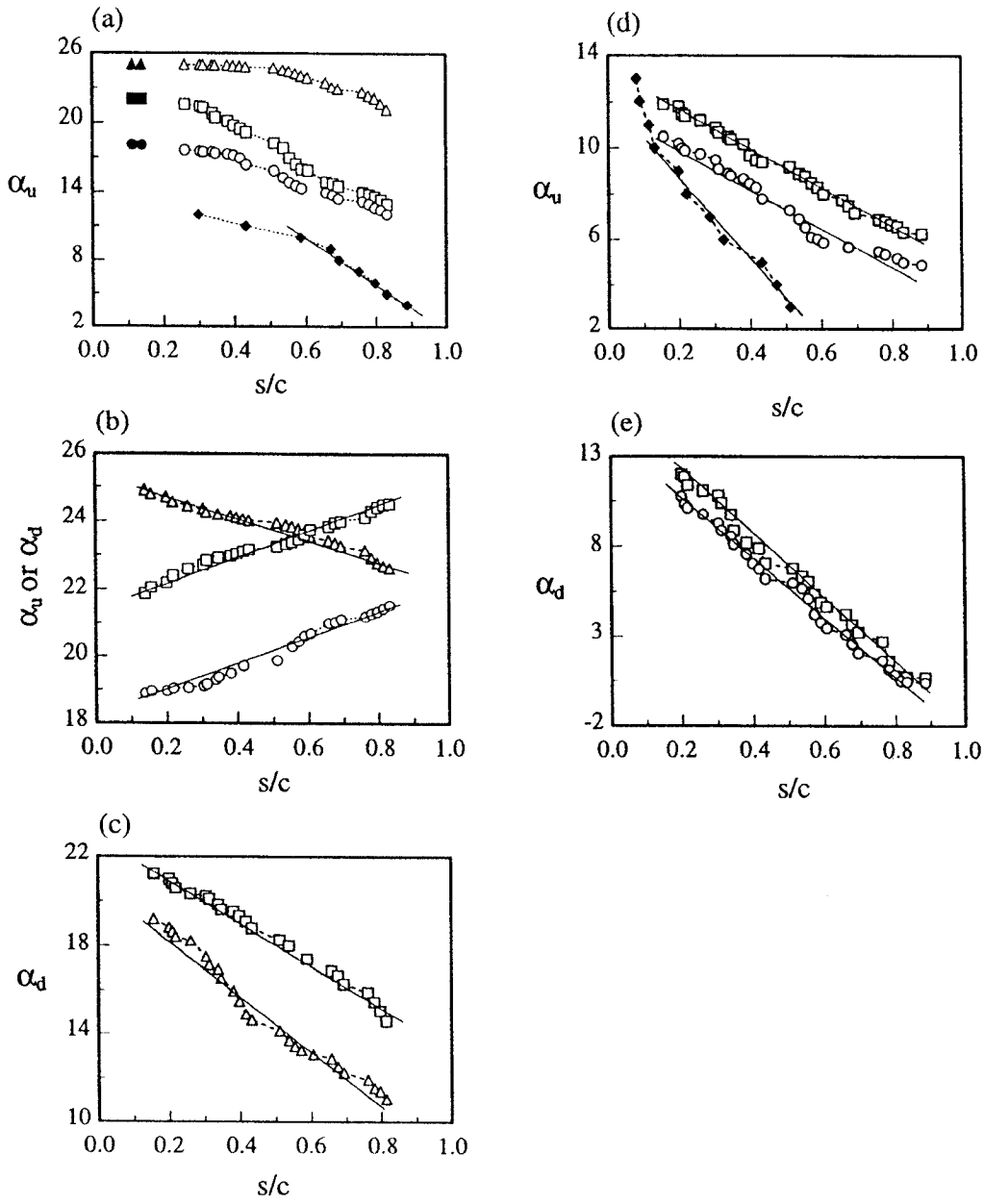

Figure 24 Effect of reduced frequency on boundary layer and stall events for $\alpha_m = 10°$ and $\Delta\alpha = 15°$: (a) flow reversal and separation; (b) LEV; (c) secondary vortex; (d) transition; and (e) reattachment. o, $\kappa = 0.05$; □, $\kappa = 0.1$; and Δ, $\kappa = 0.2$. Solid symbols denote flow reversal and open symbols turbulent breakdown. Note that for (e) and (f) the case of $\kappa = 0.2$ is omitted for clarity. ♦, static airfoil.

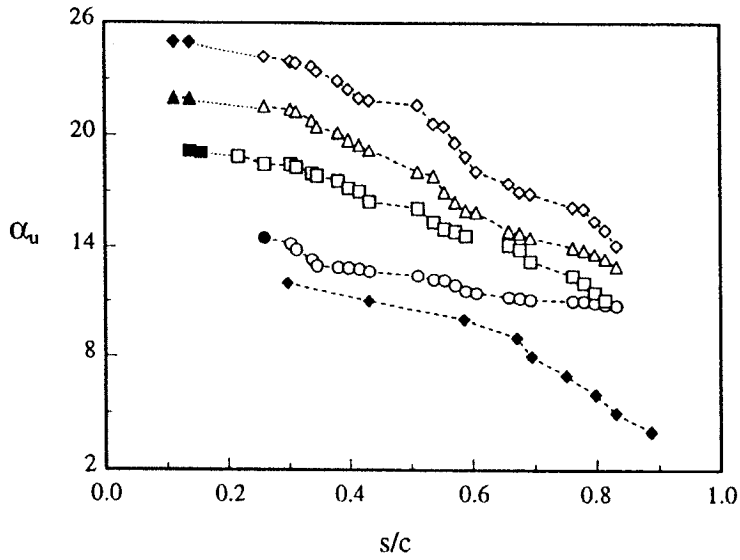

Figure 25 Effect of oscillation amplitude on flow reversal (open symbols) and turbulent breakdown (solid symbols) with $\alpha_m = 10°$ and $\kappa = 0.1$. o, $\Delta\alpha = 5°$; □, $\Delta\alpha = 10°$; Δ, $\Delta\alpha = 15°$; and ◊, $\Delta\alpha = 20°$. ♦, static airfoil.

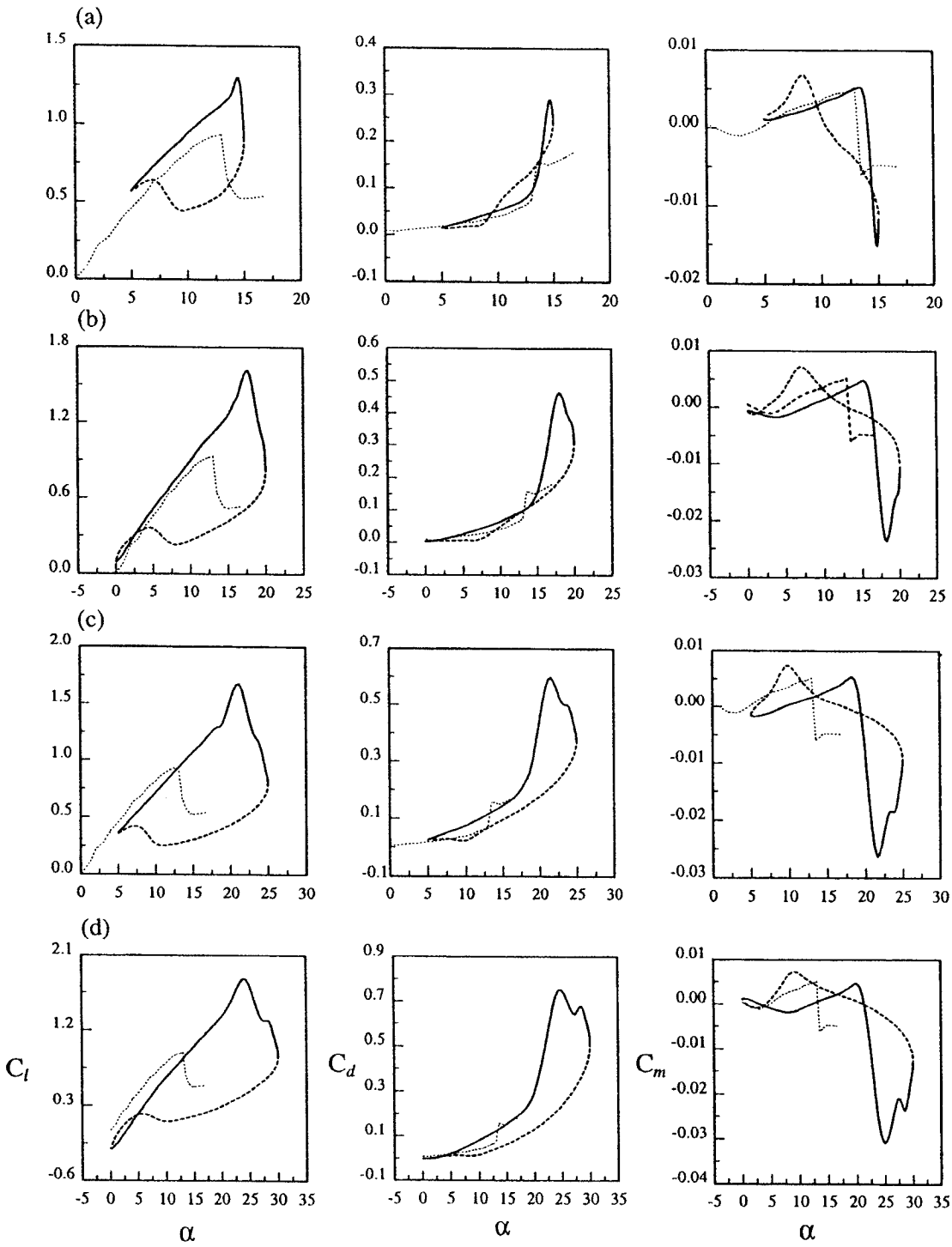

Figure 26 Dynamic load loops at $\kappa = 0.05$. $\alpha_m = 10°$: (a) $\Delta\alpha = 5°$ and (b) $\Delta\alpha = 10°$. $\alpha_m = 15°$: (c) $\Delta\alpha = 10°$ and (d) $\Delta\alpha = 15°$. ____, increasing α; – – –, decreasing α; ....., static values; M, moment stall; and L, lift stall.

APPENDIX A

FIGURES A1 – A24

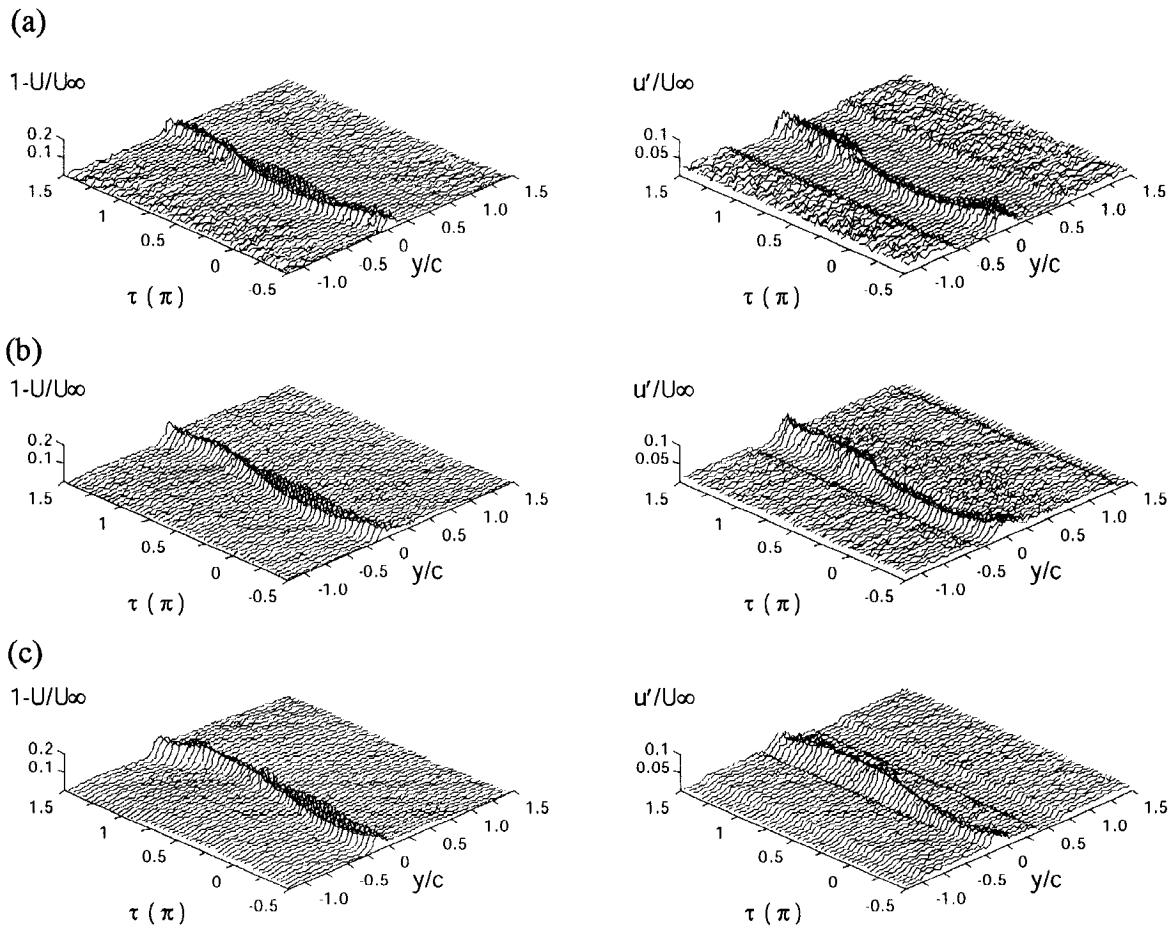

Figure A1 3-D representation of the wake mean and fluctuating velocity profiles for $\alpha(t) = 0° + 5° \sin\omega t$. (a) $\kappa = 0.025$, (b) $\kappa = 0.05$, and (c) $\kappa = 0.1$.

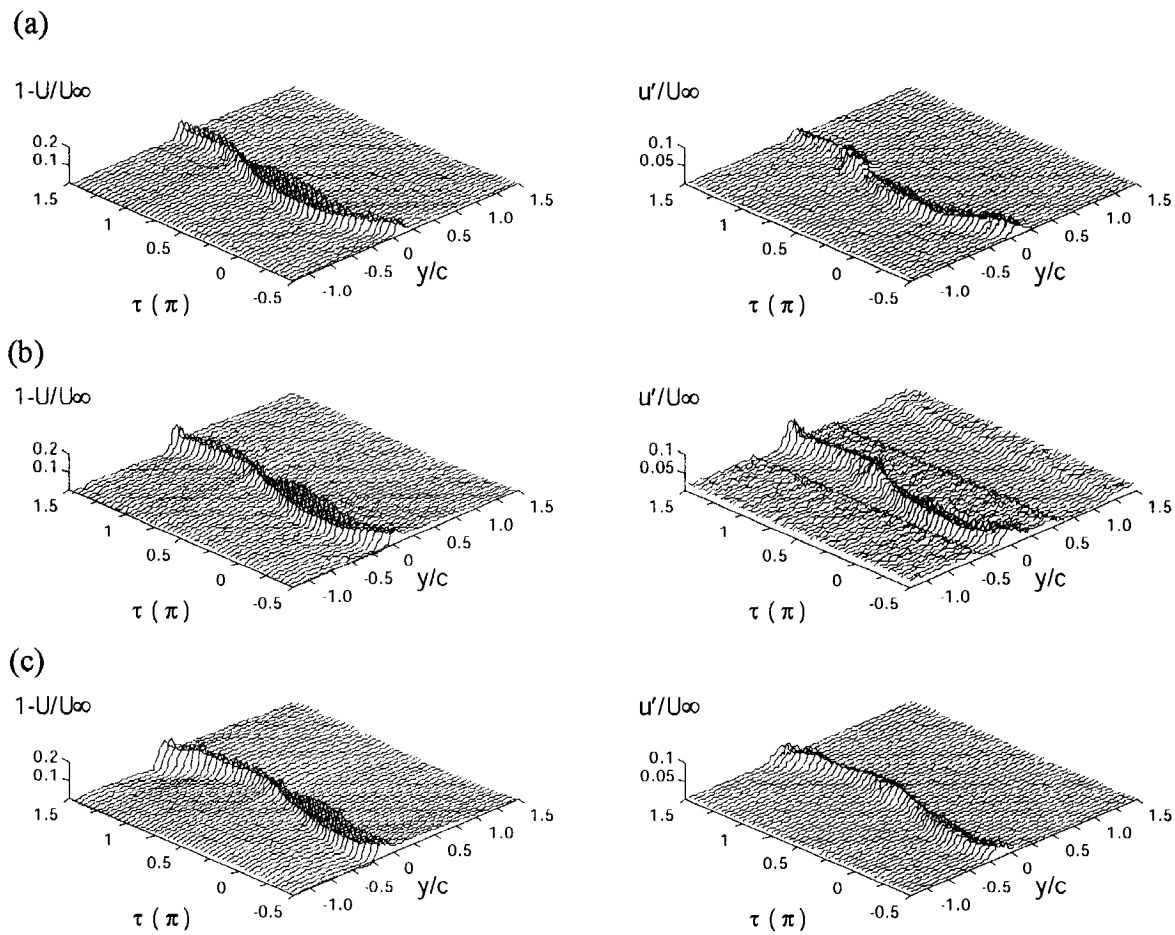

Figure A2 3-D representation of the wake mean and fluctuating velocity profiles for $\alpha(t) = 0° + 7.5° \sin\omega t$. (a) $\kappa = 0.025$, (b) $\kappa = 0.05$, and (c) $\kappa = 0.1$.

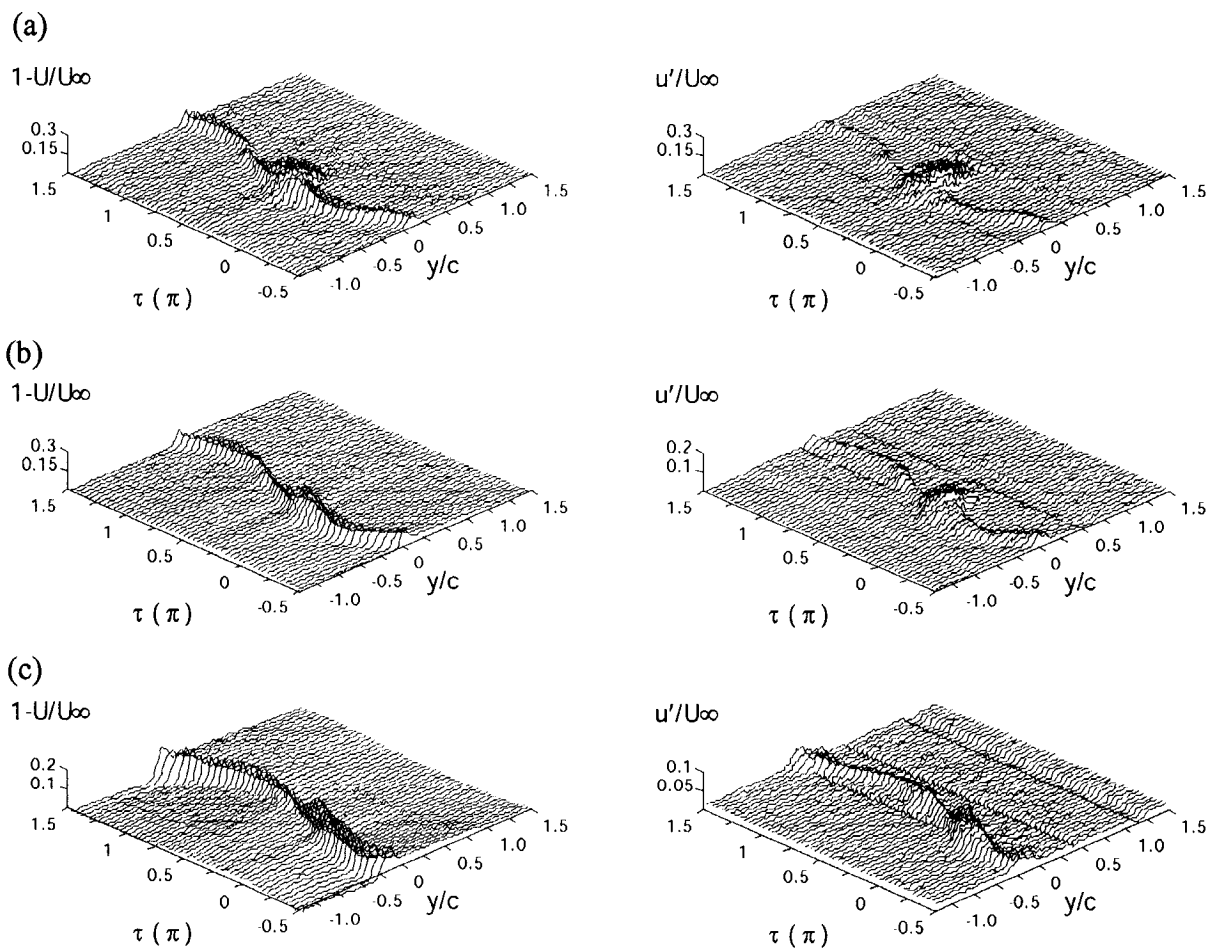

Figure A3 3-D representation of the wake mean and fluctuating velocity profiles for $\alpha(t) = 0° + 10° \sin\omega t$. (a) $\kappa = 0.025$, (b) $\kappa = 0.05$, and (c) $\kappa = 0.1$.

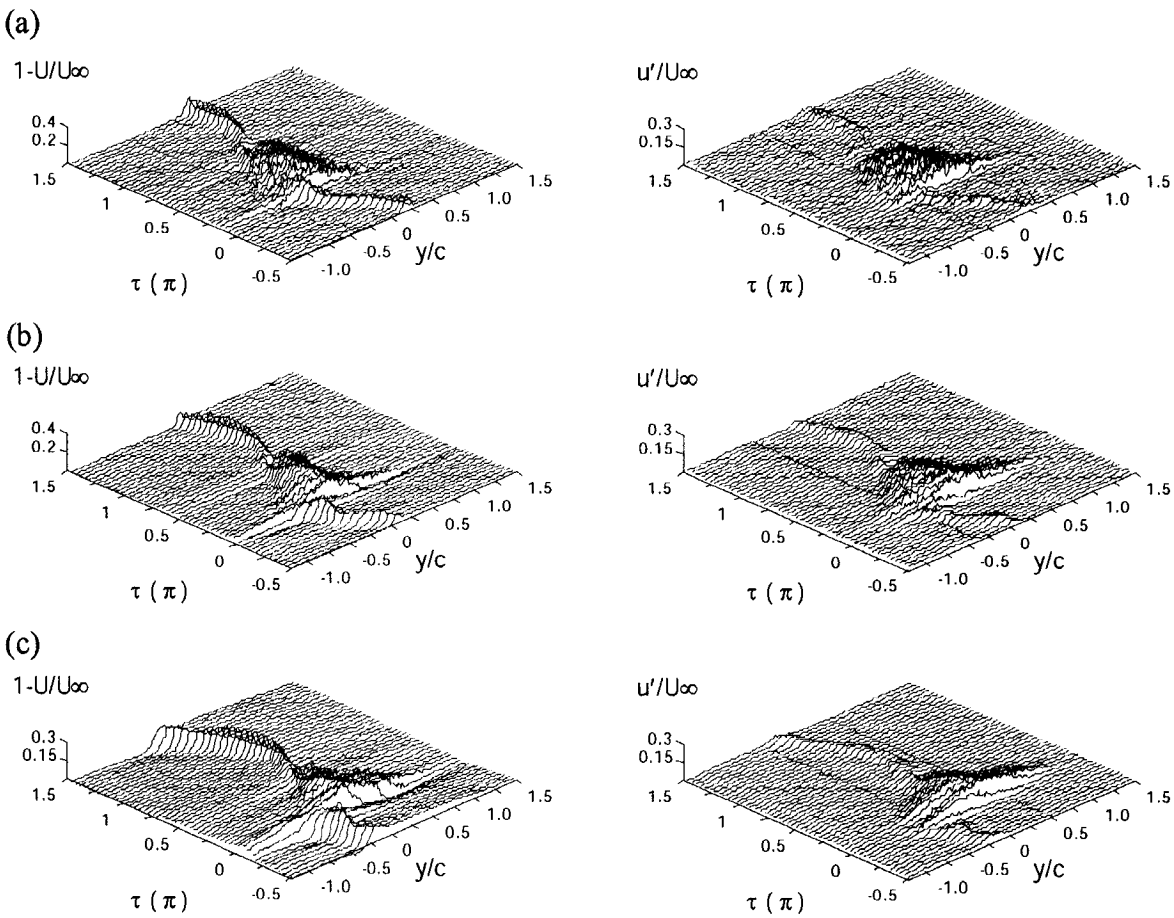

Figure A4 3-D representation of the wake mean and fluctuating velocity profiles for $\alpha(t) = 0° + 15° \sin\omega t$. (a) $\kappa = 0.025$, (b) $\kappa = 0.05$, and (c) $\kappa = 0.1$.

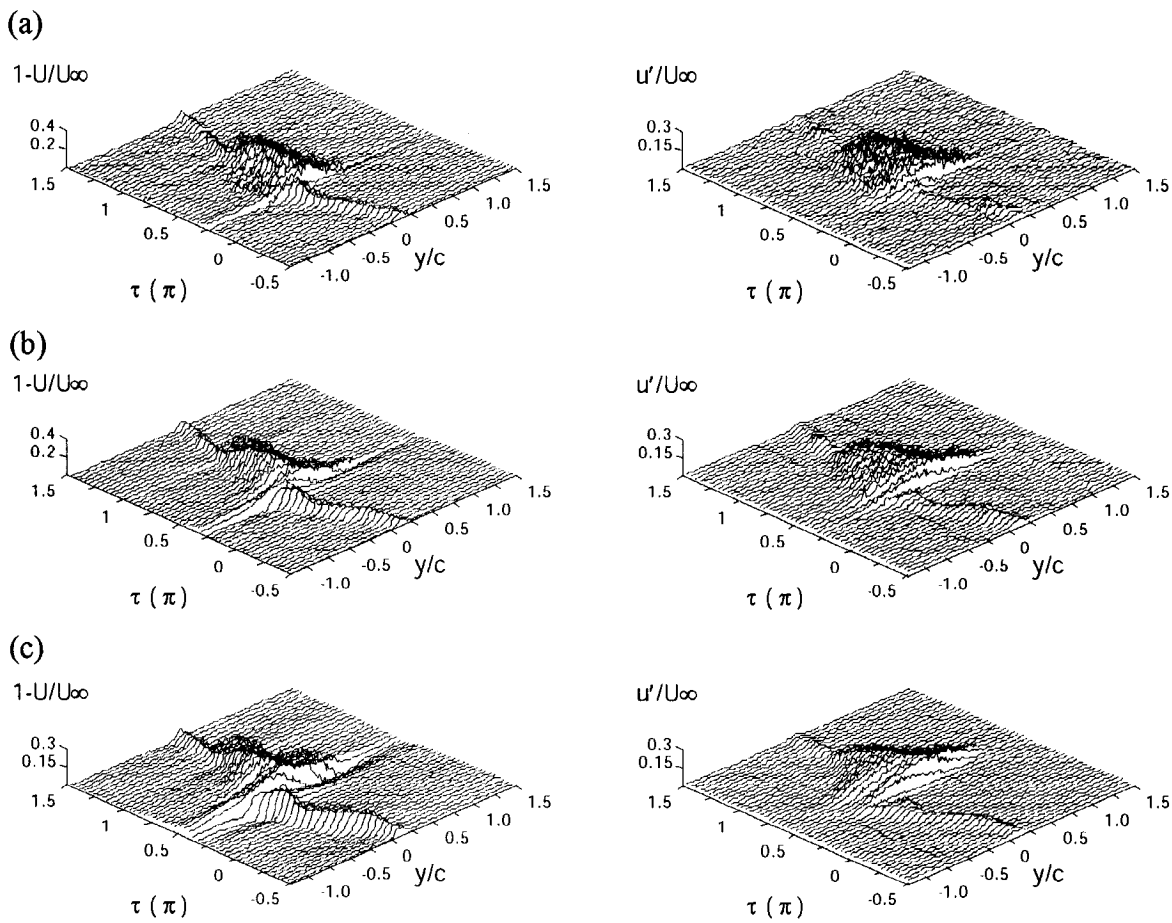

Figure A5 3-D representation of the wake mean and fluctuating velocity profiles for $\alpha(t) = 5° + 10° \sin\omega t$. (a) $\kappa = 0.025$, (b) $\kappa = 0.05$, and (c) $\kappa = 0.1$.

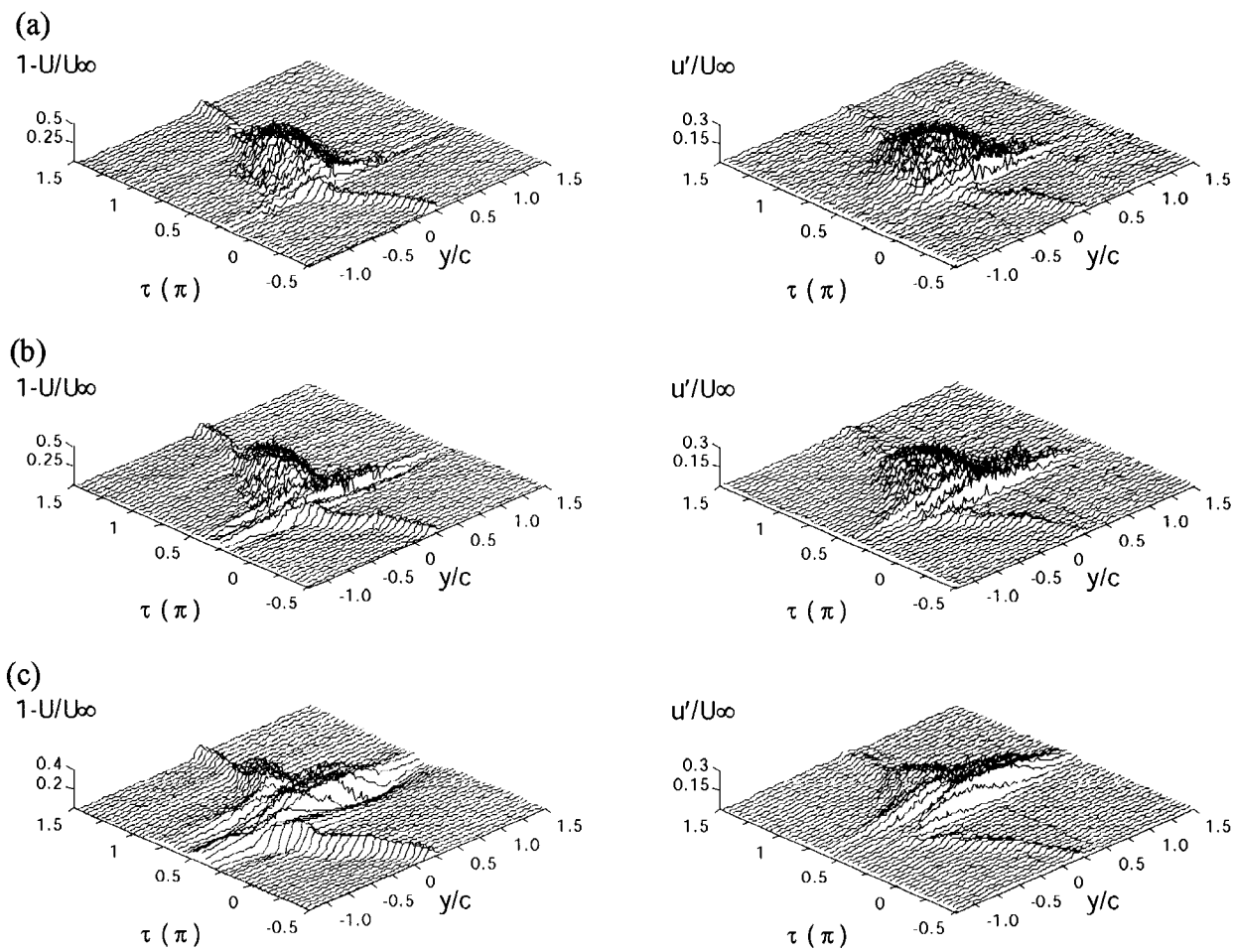

Figure A6 3-D representation of the wake mean and fluctuating velocity profiles for $\alpha(t) = 5° + 15° \sin\omega t$. (a) $\kappa = 0.025$, (b) $\kappa = 0.05$, and (c) $\kappa = 0.1$.

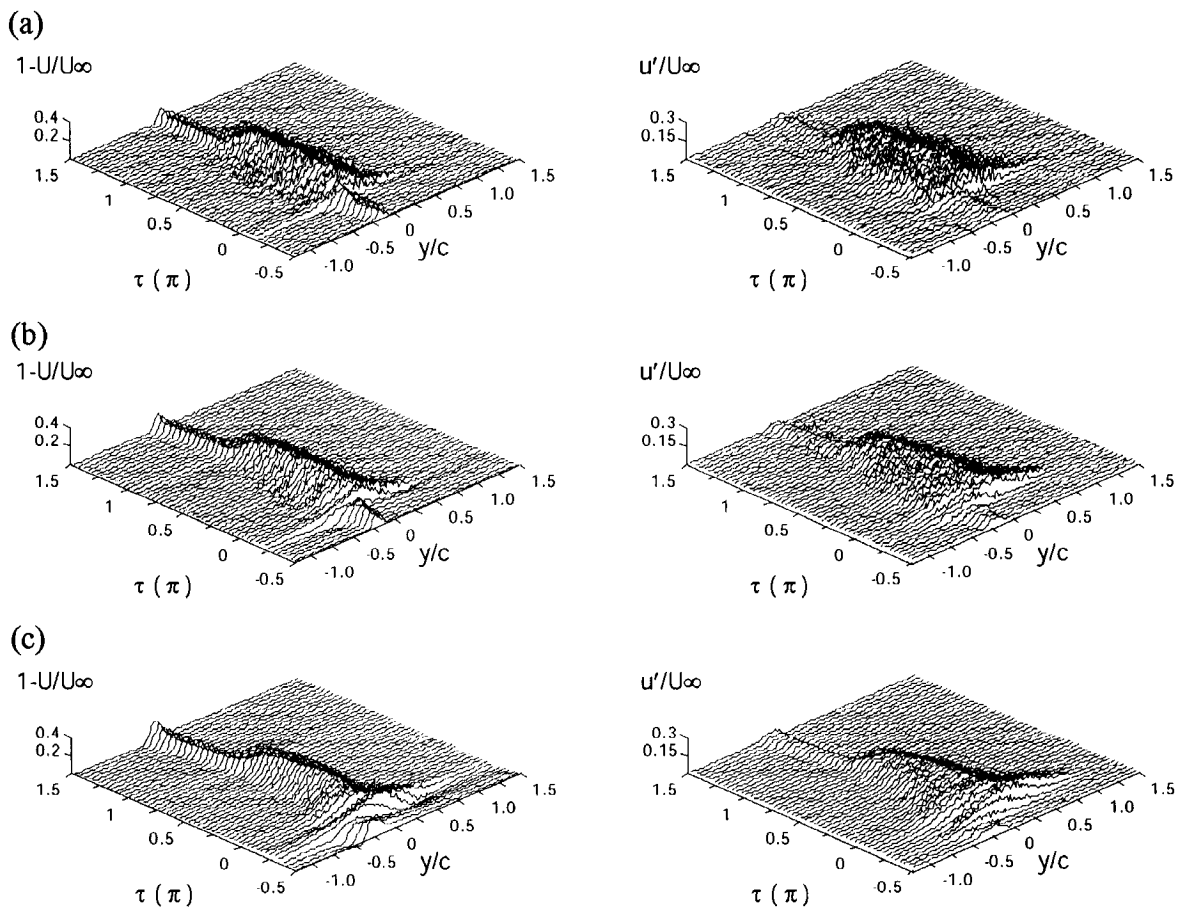

Figure A7 3-D representation of the wake mean and fluctuating velocity profiles for $\alpha(t) = 10° + 5° \sin\omega t$. (a) $\kappa = 0.025$, (b) $\kappa = 0.05$, and (c) $\kappa = 0.1$.

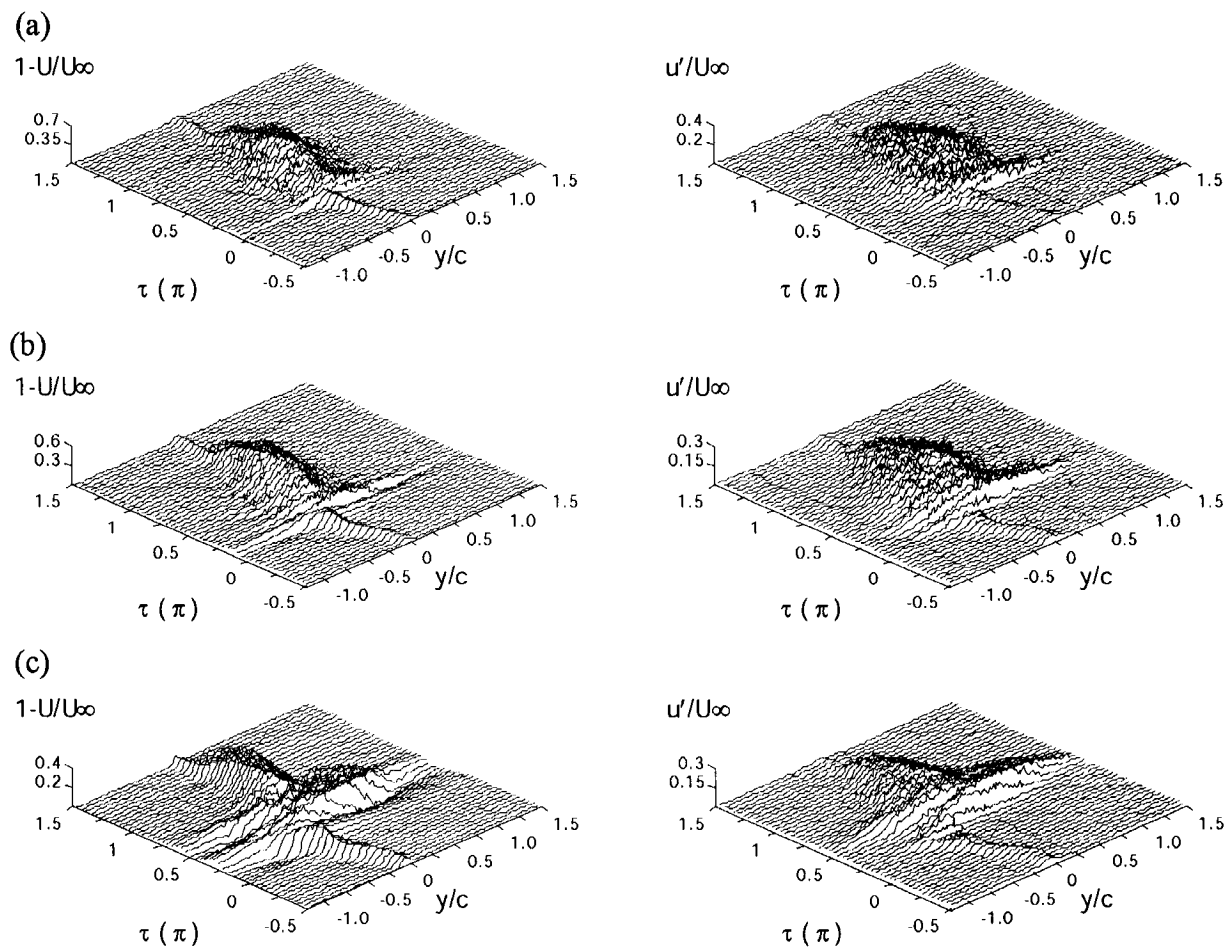

Figure A8 3-D representation of the wake mean and fluctuating velocity profiles for $\alpha(t) = 10° + 10° \sin\omega t$. (a) $\kappa = 0.025$, (b) $\kappa = 0.05$, and (c) $\kappa = 0.1$.

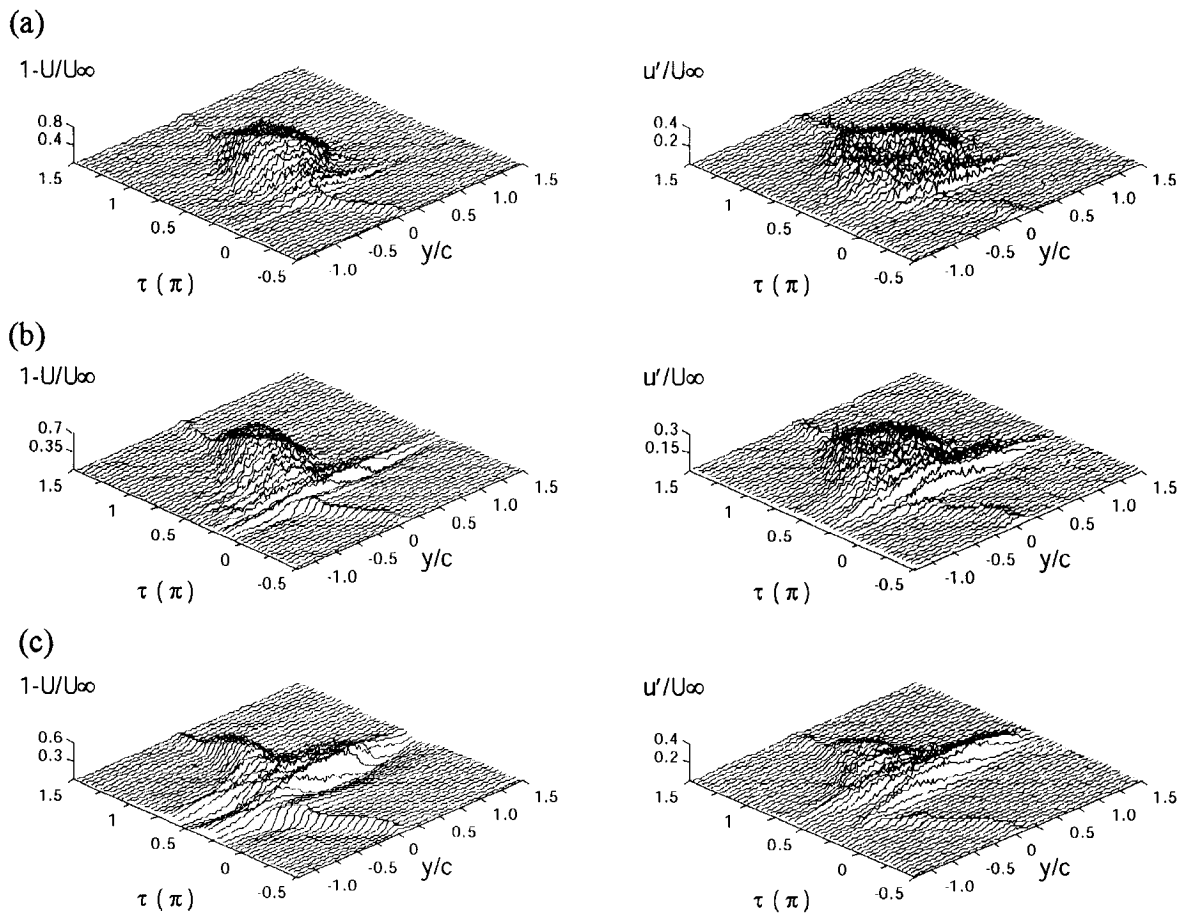

Figure A9 3-D representation of the wake mean and fluctuating velocity profiles for $\alpha(t) = 10° + 15° \sin\omega t$. (a) $\kappa = 0.025$, (b) $\kappa = 0.05$, and (c) $\kappa = 0.1$.

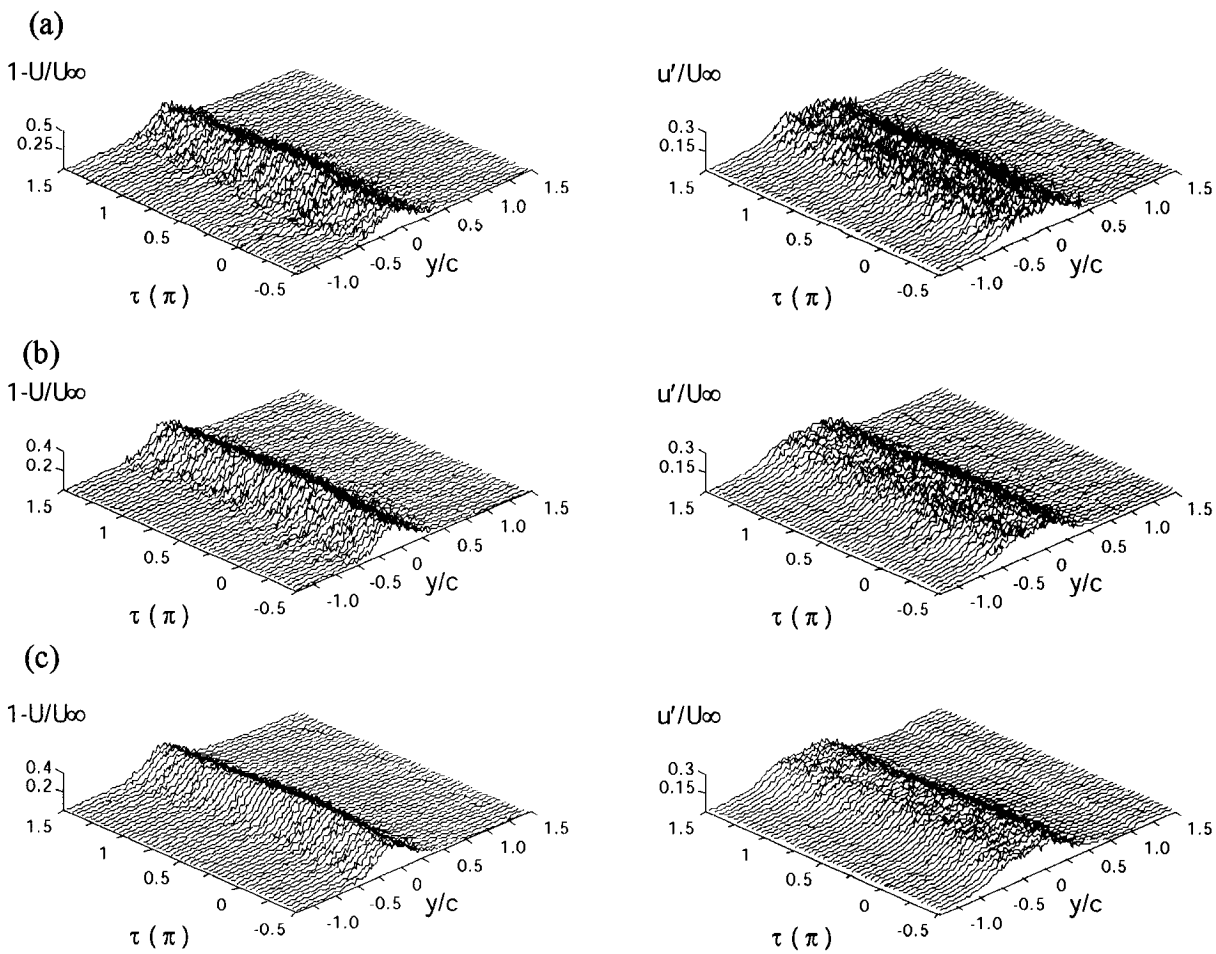

Figure A10 3-D representation of the wake mean and fluctuating velocity profiles for $\alpha(t) = 15° + 5° \sin\omega t$. (a) $\kappa = 0.025$, (b) $\kappa = 0.05$, and (c) $\kappa = 0.1$.

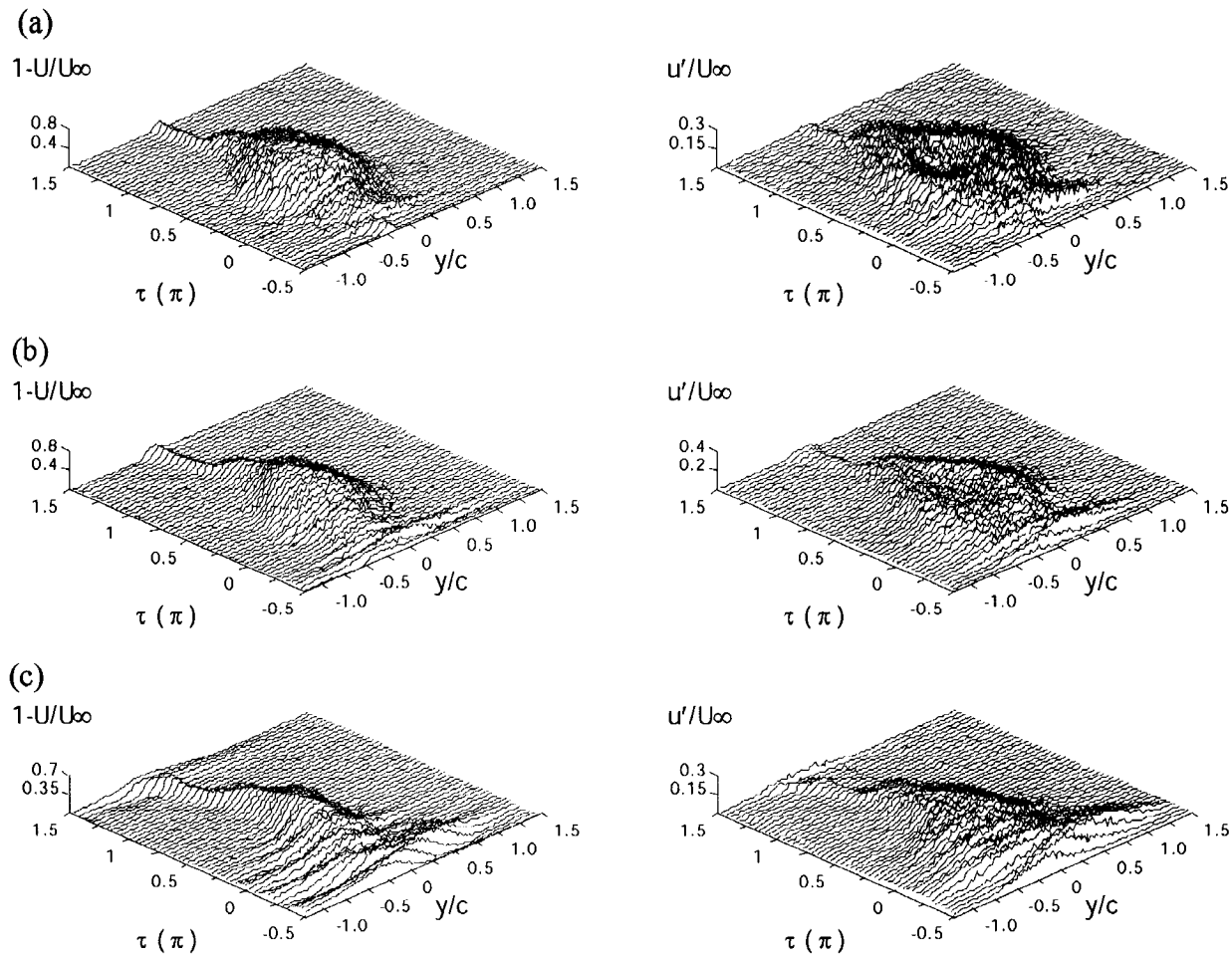

Figure A11 3-D representation of the wake mean and fluctuating velocity profiles for $\alpha(t) = 15° + 10° \sin\omega t$. (a) $\kappa = 0.025$, (b) $\kappa = 0.05$, and (c) $\kappa = 0.1$.

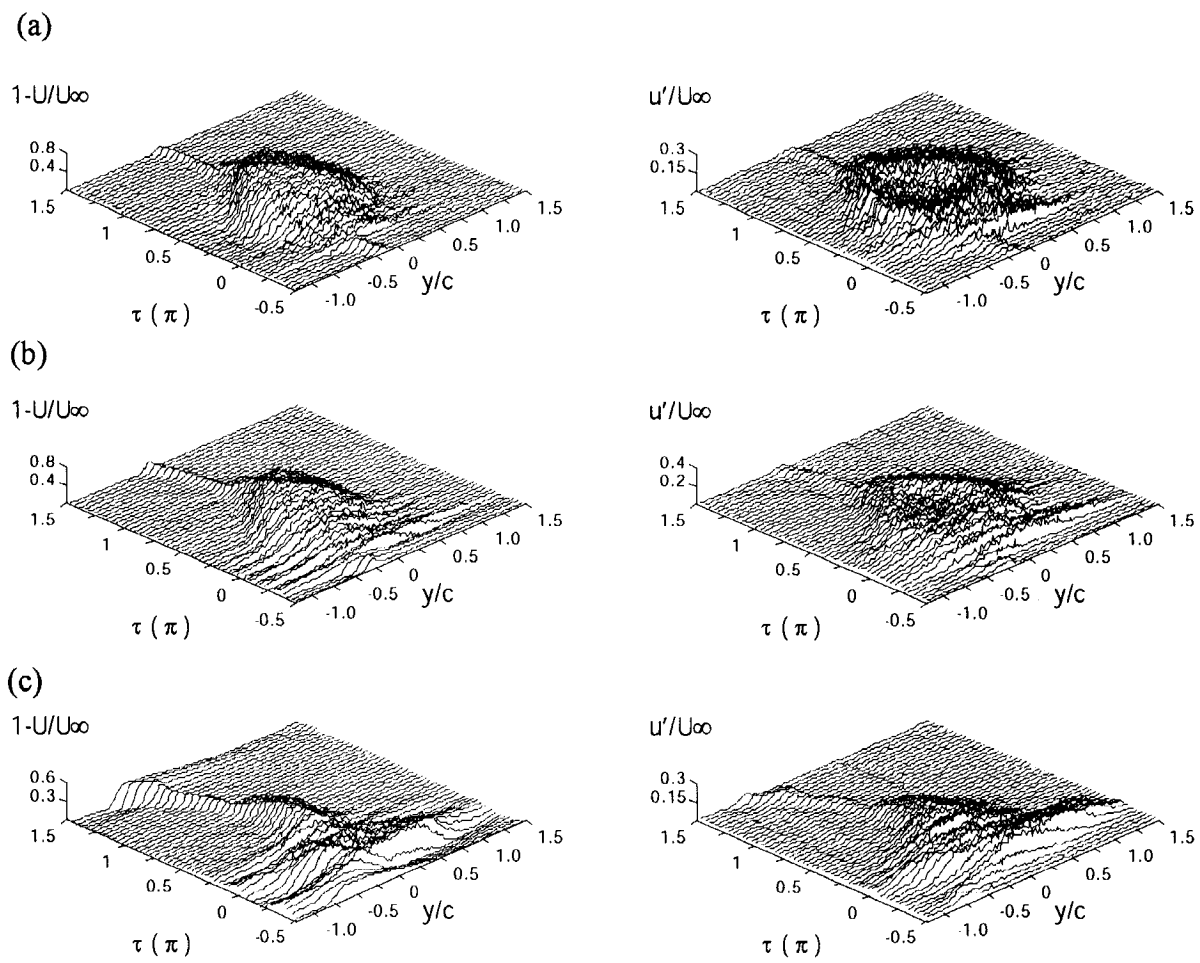

Figure A12 3-D representation of the wake mean and fluctuating velocity profiles for $\alpha(t) = 15° + 15° \sin\omega t$. (a) $\kappa = 0.025$, (b) $\kappa = 0.05$, and (c) $\kappa = 0.1$.

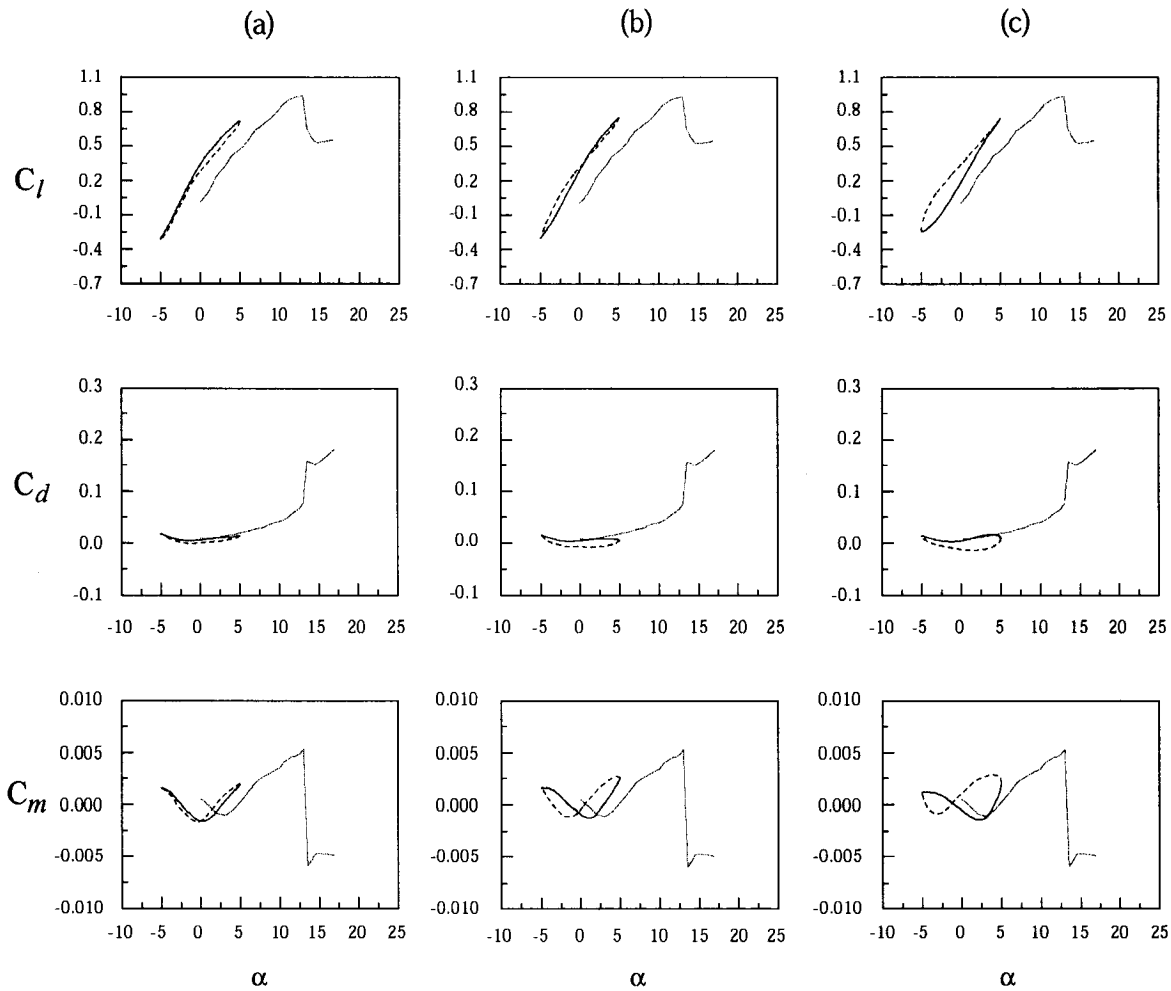

Figure A13 Dynamic loads loops for $\alpha(t) = 0° + 5° \sin\omega t$. (a) $\kappa = 0.025$, (b) $\kappa = 0.05$, and (c) $\kappa = 0.1$. ____, increasing α; – – –, decreasing α; ....., static values.

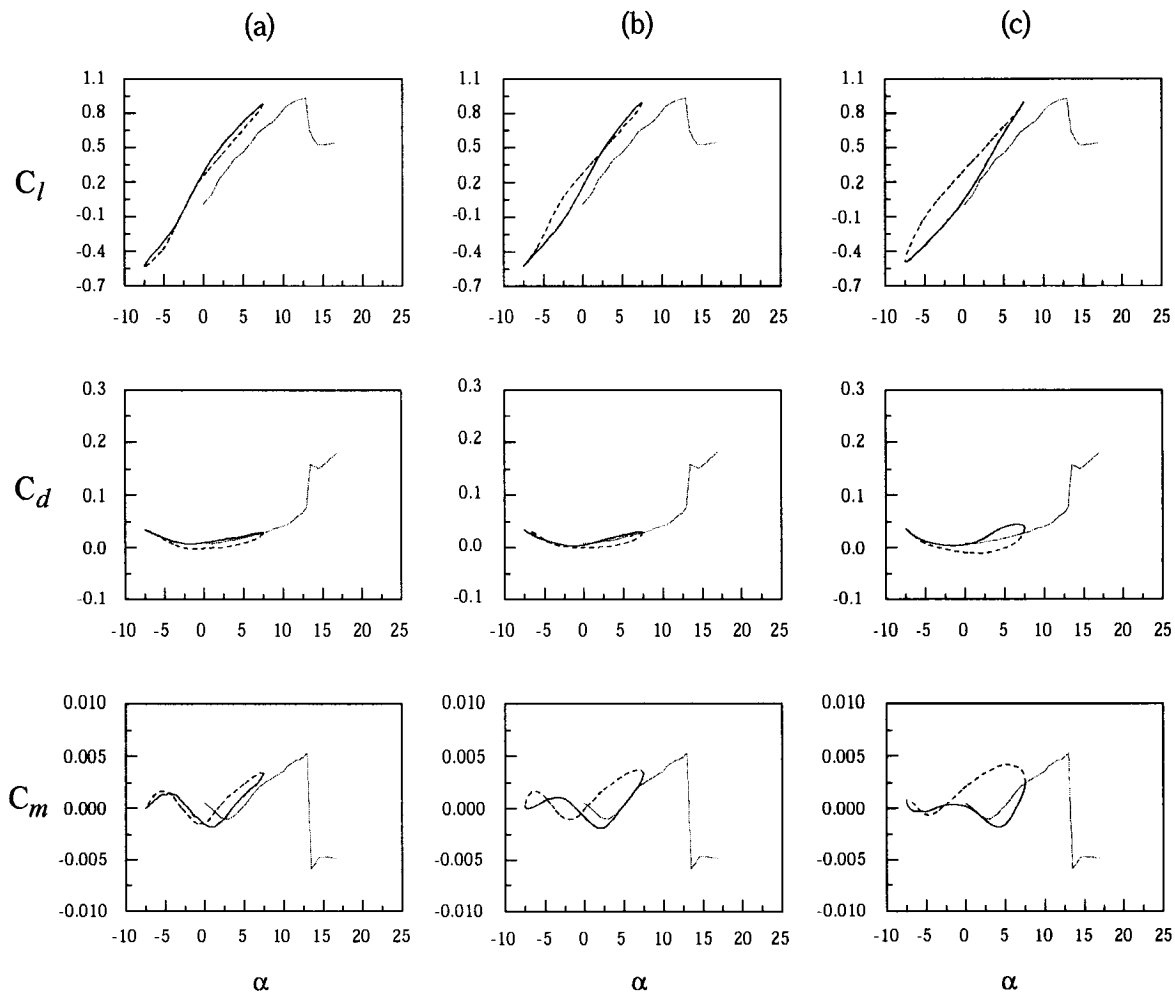

Figure A14 Dynamic loads loops for $\alpha(t) = 0° + 7.5° \sin\omega t$. (a) $\kappa = 0.025$, (b) $\kappa = 0.05$, and (c) $\kappa = 0.1$. ____, increasing α; – – –, decreasing α; ....., static values.

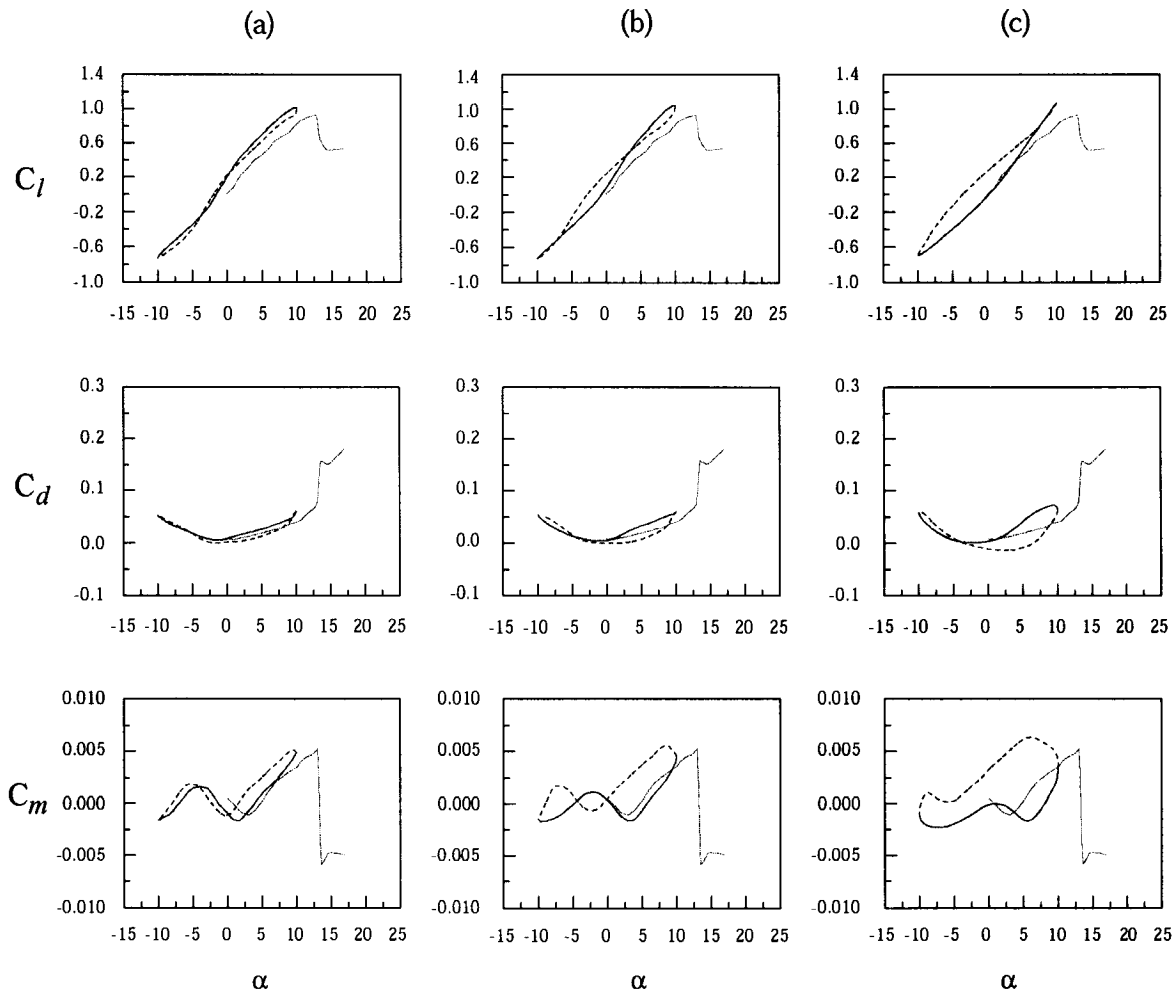

Figure A15 Dynamic loads loops for $\alpha(t) = 0° + 10° \sin\omega t$. (a) $\kappa = 0.025$, (b) $\kappa = 0.05$, and (c) $\kappa = 0.1$. ____, increasing α; – – –, decreasing α; ....., static values.

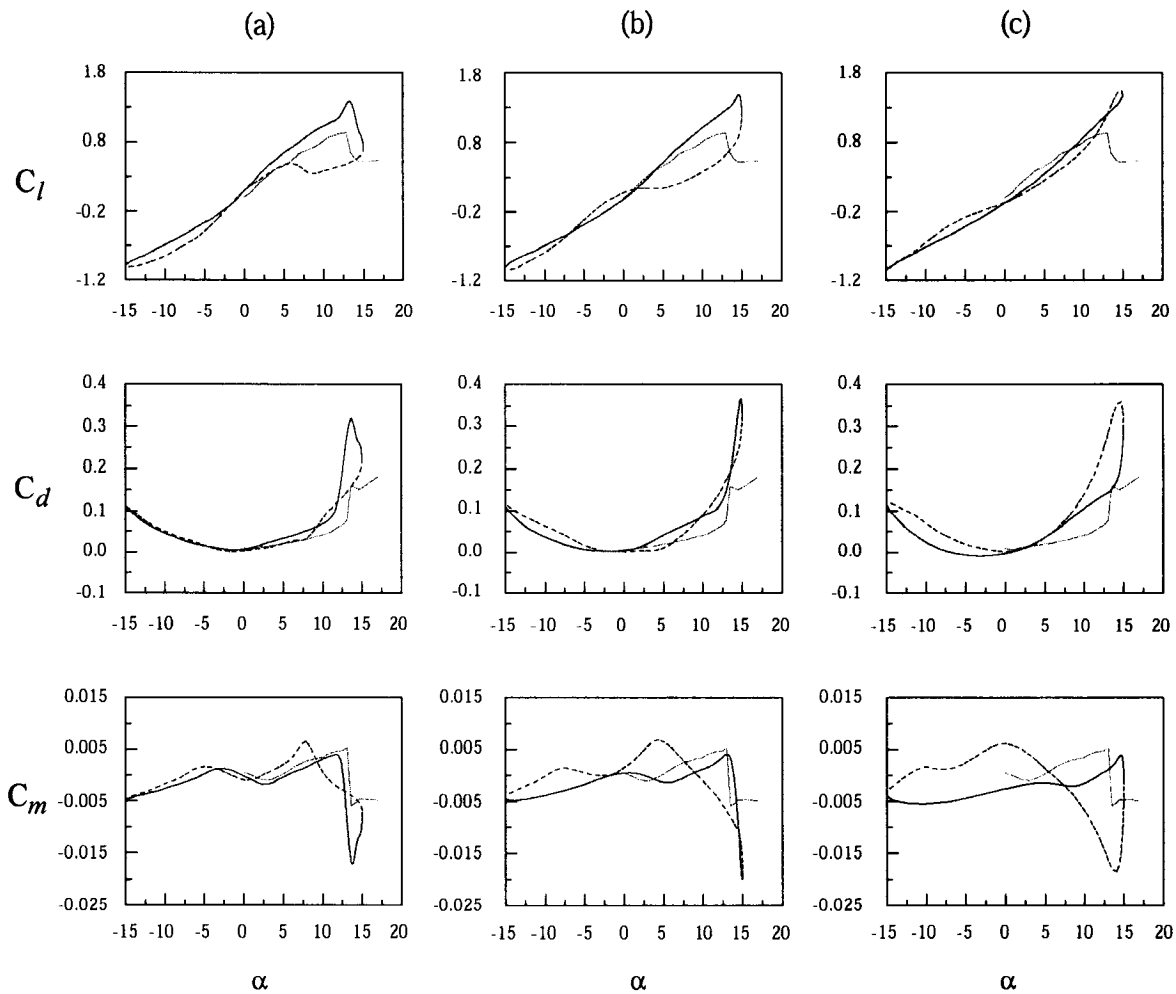

Figure A16 Dynamic loads loops for $\alpha(t) = 0° + 15° \sin\omega t$. (a) $\kappa = 0.025$, (b) $\kappa = 0.05$, and (c) $\kappa = 0.1$. ____, increasing α; – – –, decreasing α; ....., static values.

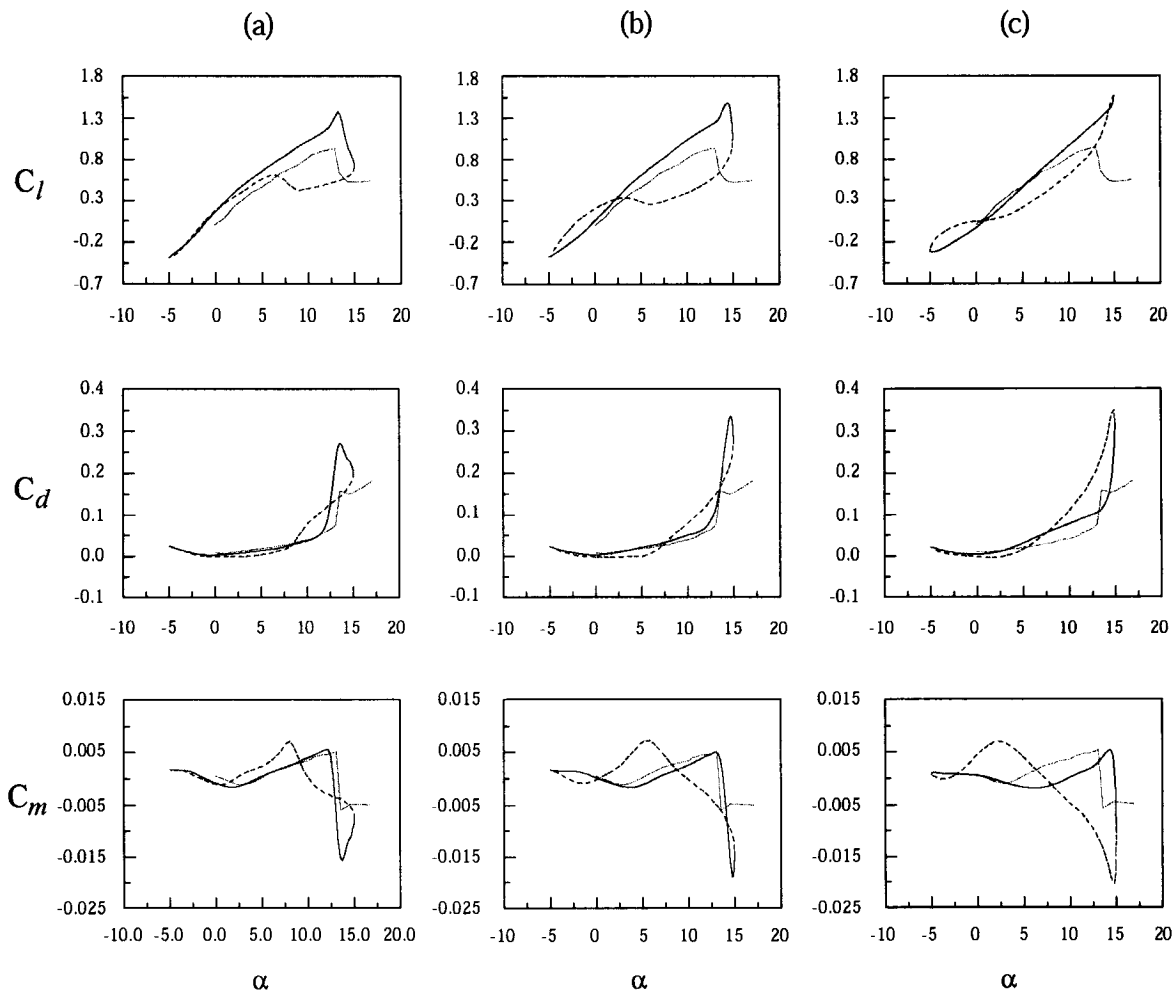

Figure A17 Dynamic loads loops for $\alpha(t) = 5° + 10° \sin\omega t$. (a) $\kappa = 0.025$, (b) $\kappa = 0.05$, and (c) $\kappa = 0.1$. ____, increasing α; – – –, decreasing α; ....., static values.

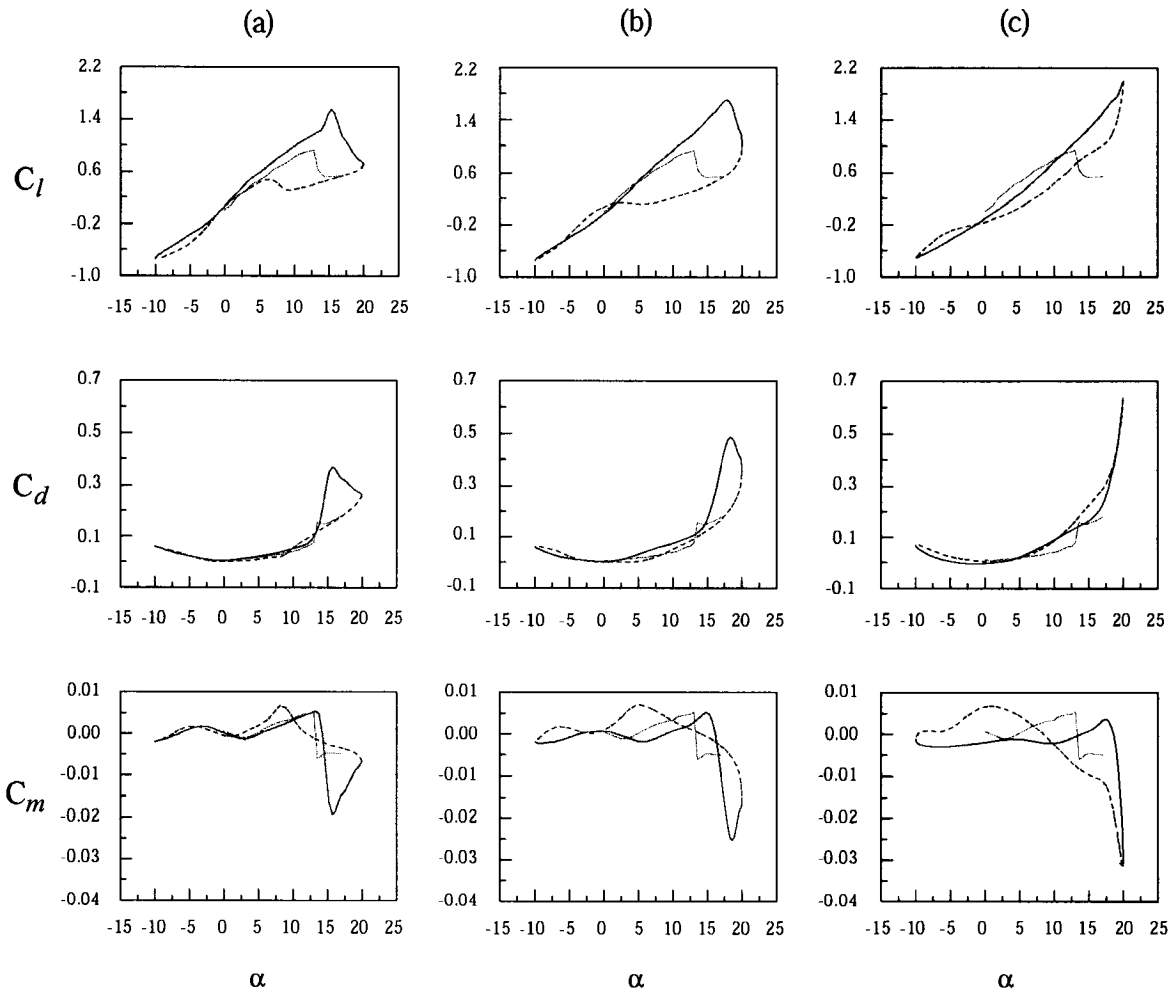

Figure A18 Dynamic loads loops for $\alpha(t) = 5° + 15° \sin\omega t$. (a) $\kappa = 0.025$, (b) $\kappa = 0.05$, and (c) $\kappa = 0.1$. ____, increasing α; – – –, decreasing α; ....., static values.

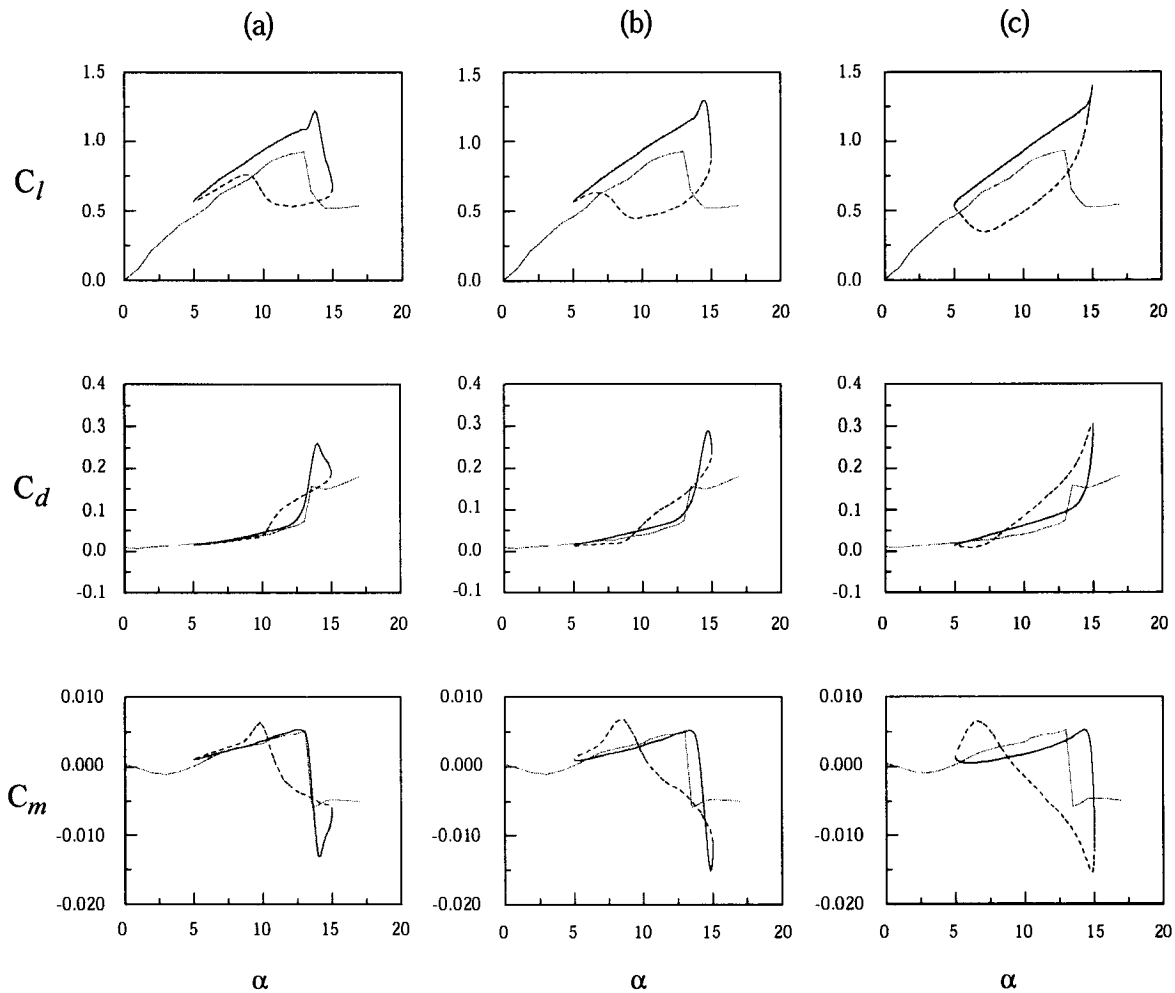

Figure A19 Dynamic loads loops for $\alpha(t) = 10° + 5° \sin\omega t$. (a) $\kappa = 0.025$, (b) $\kappa = 0.05$, and (c) $\kappa = 0.1$. ____, increasing α; – – –, decreasing α; ....., static values.

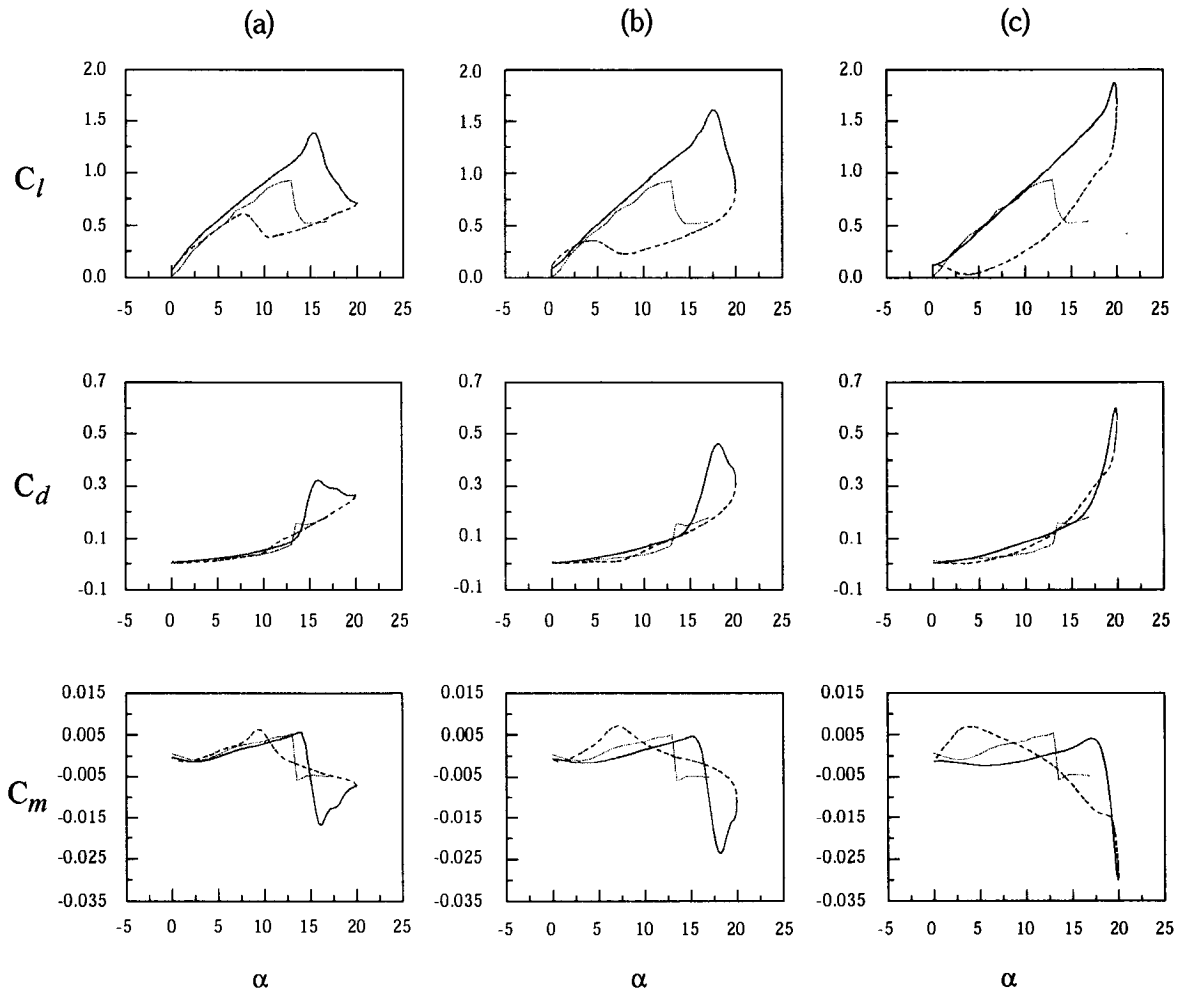

Figure A20 Dynamic loads loops for $\alpha(t) = 10° + 10° \sin\omega t$. (a) $\kappa = 0.025$, (b) $\kappa = 0.05$, and (c) $\kappa = 0.1$. ____, increasing α; – – –, decreasing α; ....., static values.

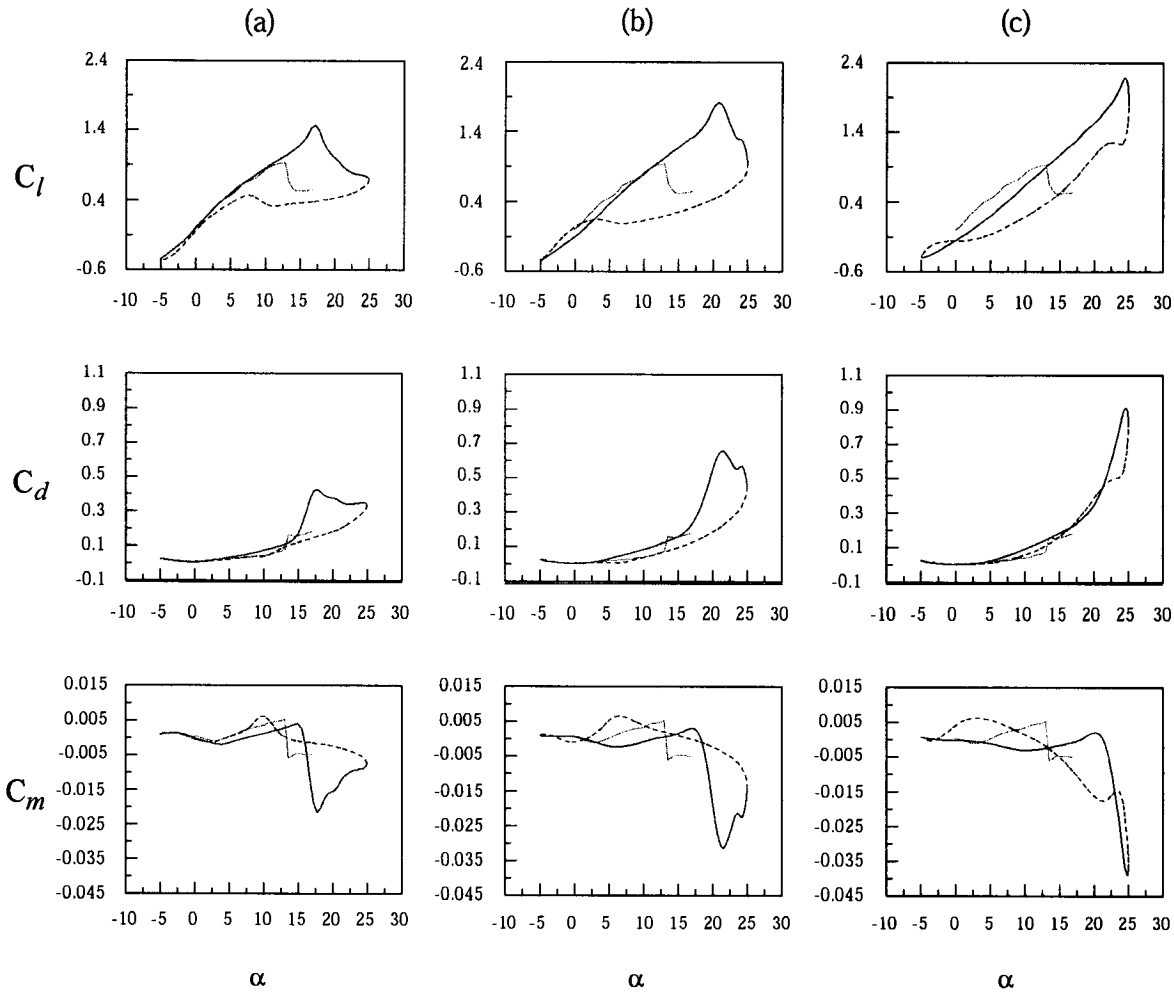

Figure A21 Dynamic loads loops for $\alpha(t) = 10° + 15° \sin\omega t$. (a) $\kappa = 0.025$, (b) $\kappa = 0.05$, and (c) $\kappa = 0.1$. ____, increasing α; – – –, decreasing α; ....., static values.

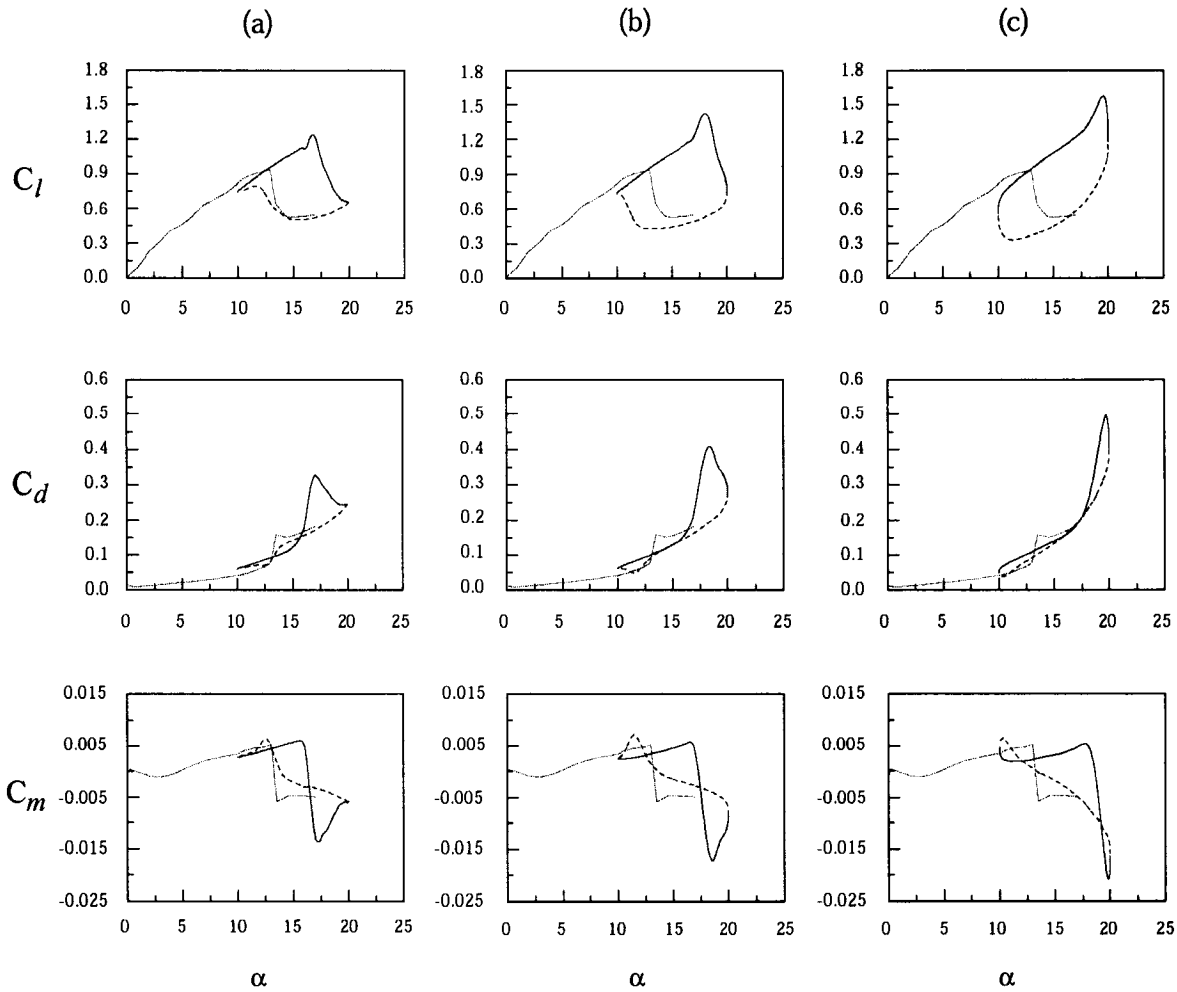

Figure A22 Dynamic loads loops for $\alpha(t) = 15° + 5° \sin\omega t$. (a) $\kappa = 0.025$, (b) $\kappa = 0.05$, and (c) $\kappa = 0.1$. ____, increasing α; – – –, decreasing α; ....., static values.

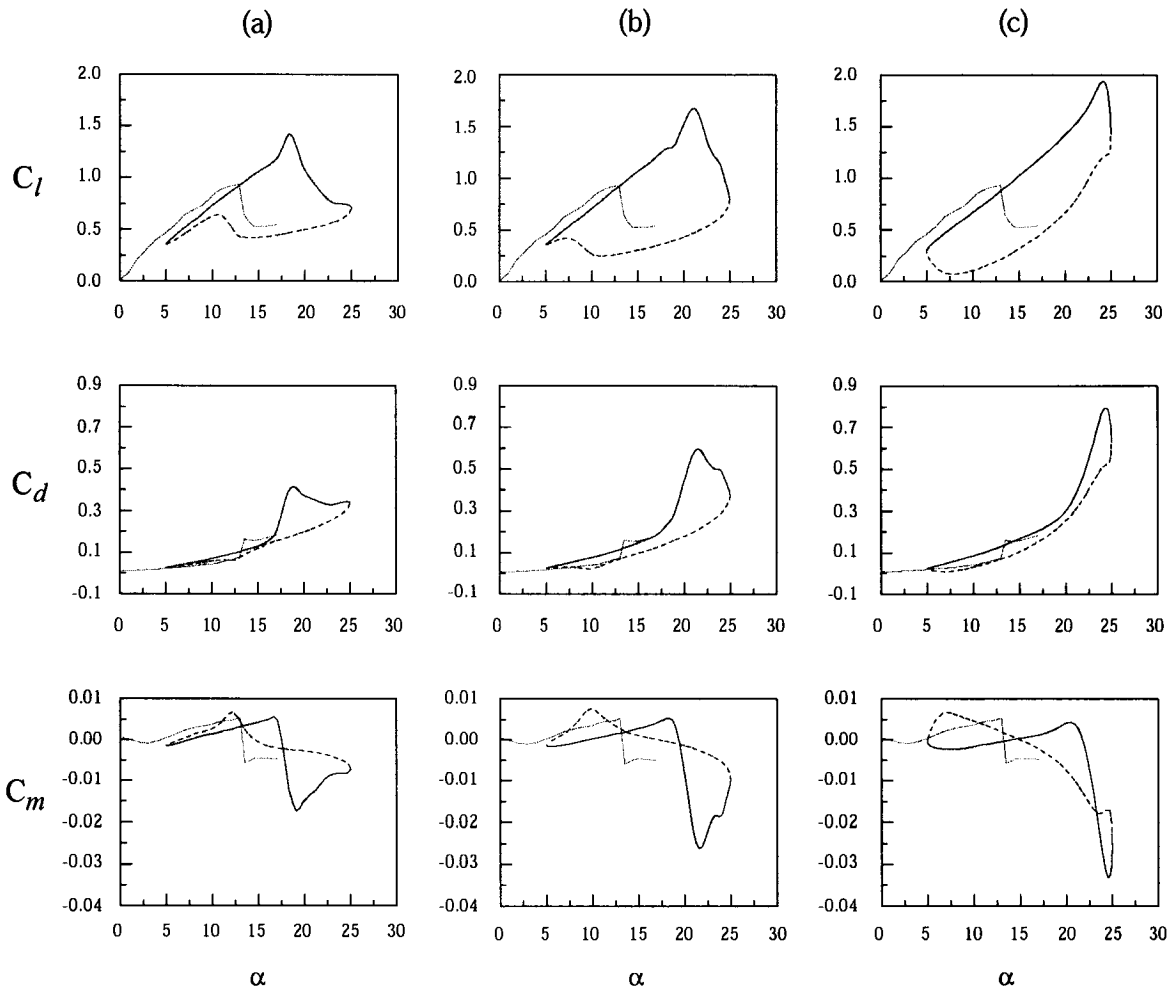

Figure A23 Dynamic loads loops for $\alpha(t) = 15° + 10° \sin\omega t$. (a) $\kappa = 0.025$, (b) $\kappa = 0.05$, and (c) $\kappa = 0.1$. ____, increasing α; – – –, decreasing α; ....., static values.

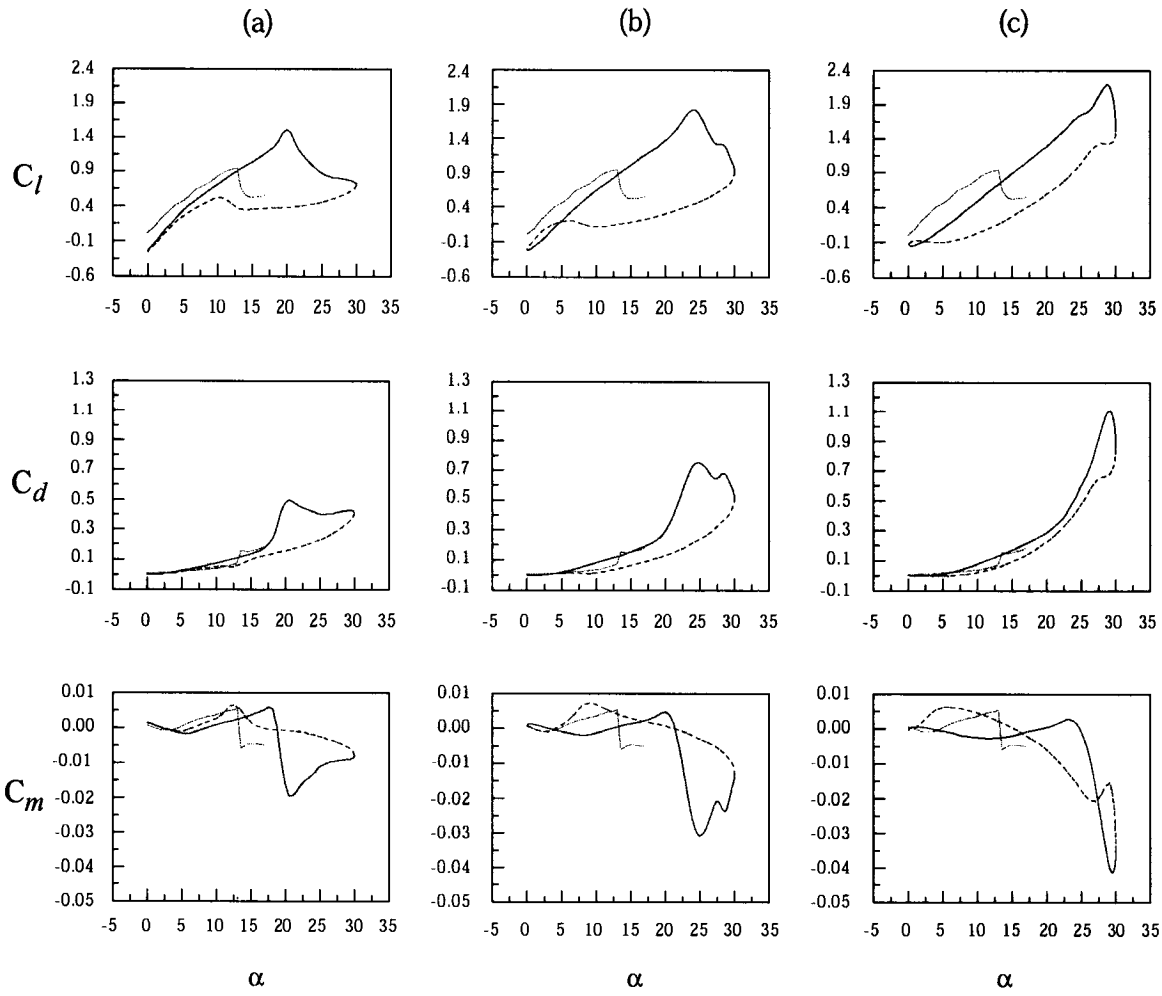

Figure A24 Dynamic loads loops for $\alpha(t) = 15° + 15° \sin\omega t$. (a) $\kappa = 0.025$, (b) $\kappa = 0.05$, and (c) $\kappa = 0.1$. ____, increasing α; – – –, decreasing α; ....., static values.